Preparation and characterisation of two-dimensional ferroelectrics

DISSERTATION

zur Erlangung des Grades eines Doktors
der Naturwissenschaften

vorgelegt von
M.Sc. Paulus Aleksa

Betreuer und erster Gutachter:

Prof. Dr. Carsten Busse
Universität Siegen

Zweiter Gutachter:

Dr. Arkady Krasheninnikov
Helmholtz-Zentrum Dresden-Rossendorf

Tag der mündlichen Prüfung:
05.06.2024

Abstract

Many two-dimensional materials are theoretically predicted to have remarkable properties, such as robust ferroelectricity for group-IV monochalcogenides. Ferroelectric materials exhibit a spontaneous polarisation in the absence of any external electrical field. Group-IV monochalcogenides consist of a metal (M = Ge, Sn) and a chalcogen (X = S, Se, Te) atom in equal parts. However, their investigation in terms of experimental preparation and characterisation is still scarce, even though such studies are the basis for all work and allow further insight into the growth process.

In this work, ultra-high vacuum chambers equipped with evaporators that allow molecular beam epitaxy were used to achieve highly controllable and clean environments. In addition, powerful tools like scanning tunneling microscopy (STM) and low electron energy diffraction (LEED) are used for crystallographic investigation with a focus on structure and shape determination of group-IV monochalcogenides. In particular, SnSe, GeSe, and SnS were investigated in this thesis.

Monolayer SnSe forms fractal-dendritic islands at room temperature on a graphene on Ir(111) surface. The shape is systematically studied during an annealing sequence. A change in shape could be observed and the equilibrium shape is reached at $570\,$K. This shape can be described as a rhombus consisting of only $\langle 110 \rangle$ edges. Due to coverage and island density not changing during this annealing sequence, it can be proven that no ripening process takes place, contrary to most growth processes of other two-dimensional materials. Desorption starts at around $600\,$K, which is indicated by a reduction in coverage and island density, until all islands vanish. A closer study of these edges, in terms of atomically resolved STM images and first-principle studies reveal an edge relaxation, which minimises the formation energy of such edges. Further investigations on the electronic structure show that this material is a semiconductor with a bandgap of $2.16\,$eV and the relaxation reduces the charge effect at the edges.

The formation of bilayer structures is highly present in this material and needs to be actively suppressed for monolayer investigations. This behaviour is also shown in a coverage study. However, no standard growth model can describe this tendency for bilayer preference. The study of bilayer SnSe reveals that multiple stacking orientations are possible, even when the islands grow together without clear boundaries. Electronic investigations show that an edge effect is present, which can not be explained by ferro- or antiferroelectric properties.

GeSe forms different amorphous structures on graphene substrates on multiple crystals under various conditions. This indicates that crystallisation is difficult. However, the crystallisation on Au(111) results in the out-of-plane ferroelectric β-polymorph. The growth can be described as self-limited since no second layer formation could be observed. Measurements reveal that the semiconductor, with a bandgap of $1.13\,$eV, expresses a hexagonal lattice with a complex superstructure.

The crystallisation of SnS can be achieved on various substrates, like graphene on Ir(111) and Au(111) presented here, as well as others in literature. First measurements aimed to experimentally determine the critical temperature with LEED measurements at elevated temperatures reveal significantly lower values than theoretically predicted.

This thesis demonstrates growth conditions of multiple group-IV monochalcogenide materials and focusses mainly on preparation and crystallographic properties. Despite the novelty and complexity of these materials, the presented results unveil promising properties and encourage for further in-depth investigations.

Kurzzusammenfassung

Theoretische Untersuchungen sagen für viele zweidimensionale Materialien bemerkenswerte Eigenschaften vorher, wie beispielsweise starke Ferroelektrizität für Monochalkogenide der Gruppe IV. Ferroelektrische Materialien weisen eine spontane Polarisation auf, auch ohne den Einfluss eines externen elektrischen Feldes. Monochalkogenide der Gruppe IV bestehen aus einem Metall- (M = Ge, Sn) und einem Chalkogenatom (X = S, Se, Te) in einem 1:1 Verhältnis. Arbeiten zur experimentellen Herstellung und Charakterisierung sind noch eher selten, jedoch sind solche Studien äußerst relevant, um weitere Erkenntnisse in den Wachstumsprozess zu bekommen.

In dieser Arbeit werden Ultrahochvakuumkammern verwendet, welche mit Verdampfern zur Molekularstrahlepitaxie ausgestattet sind, um hoch kontrollierbare und saubere Rahmenbedingungen zu erreichen. Darüber hinaus werden Messmethoden wie Rastertunnelmikrokopie (RTM) und Diffraktometrie mit niedriger Elektronenenergie für kristallographische Untersuchungen verwendet, wobei der Schwerpunkt auf der Struktur- und Formbestimmung von Monochalkogeniden der Gruppe IV liegt. Insbesondere wurden die Materialien SnSe, GeSe und SnS in dieser Thesis untersucht.

Einzelschichtiges SnSe bildet bei Raumtemperatur fraktal-dendritische Inseln auf einer Graphen auf Ir(111)-Oberfläche. Die Inselform wird während einer Heizsequenz systematisch untersucht. Es konnte eine Formänderung beobachtet werden und die Gleichgewichtsform wird bei 570 K erreicht. Diese Form kann als Raute beschrieben werden, die nur aus $\langle 110 \rangle$ Kanten besteht. Da sich Bedeckung und Inseldichte während dieser Sequenz nicht ändern, kann kein Reifungsprozess beobachtet werden. Ab einer Temperatur von etwa 600 K beginnt Desorption von der Oberfläche, was durch eine Verringerung der Bedeckung und der Inseldichte zu beobachten ist, bis jegliche Inseln abgedampft sind. Eine genauere Untersuchung der Kanten mittels atomar aufgelöster RTM-Bilder und Dichte-Funktional-Theorie-Simulationen offenbaren eine Relaxation der Kante, welche die Bildungsenergie solcher Kanten minimiert. Weitere Untersuchungen zur elektronischen Struktur zeigen, dass es sich bei diesem Material um einen Halbleiter mit einer Bandlücke von 2,16 eV handelt und die Relaxation Ladungseffekte an den Kanten verringert.

Die Bildung von Doppelschichtstrukturen ist in diesem Material stark ausgeprägt und muss für Einzelschichtuntersuchungen aktiv verhindert werden. Dieses Verhalten zeigt sich auch in einer Bedeckungsuntersuchung. Allerdings kann kein herkömmliches Wachstumsmodell diese starke Tendenz zur Bevorzugung des Doppelschichtwachstums beschreiben. Die Untersuchung der SnSe-Doppelschicht ergab, dass mehrere Stapelorientierungen möglich sind, wobei Inseln auch ohne klare Domänengrenze zusammenwachsen. Elektronische Untersuchungen zeigen, dass ein Randeffekt vorliegt, der nicht durch ferro- oder antiferroelektrische Eigenschaften erklärt werden kann.

GeSe bildet unter verschiedenen Bedingungen unterschiedliche amorphe Strukturen auf Graphen auf diversen Einkristallsubstraten. Dies weist darauf hin, dass die Kristallisation erschwert ist. Allerdings führt die Kristallisation auf Au(111) zum senkrecht zur Ebene ferroelektrischen β-Polymorph. Das Wachstum kann als selbstlimitierend bezeichnet werden, da kein Wachstum in der zweiten Lage beobachtet werden konnte.

Messungen zeigen, dass der Halbleiter mit einer Bandlücke von 1,13 eV ein hexagonales Gitter mit einer komplexen Überstruktur aufweist.

Die Kristallisation von SnS kann auf verschiedenen Substraten erreicht werden, wie dem hier vorgestellten Graphen auf Ir(111) und Au(111), sowie auch anderen bereits in der Literatur vorgestellten Substraten. Erste Messungen zur experimentellen Bestimmung der kritischen Temperatur mittels LEED-Messungen bei erhöhten Temperaturen ergaben deutlich niedrigere Werte als theoretisch vorhergesagt.

Diese Arbeit demonstriert die Wachstumsbedingungen mehrerer Monochalkogenide der Gruppe IV und konzentriert sich hauptsächlich auf die Herstellung und die kristallographischen Eigenschaften. Trotz der Neuheit und Komplexität dieser Materialien offenbaren die präsentierten Ergebnisse vielversprechende Eigenschaften und regen zu weiteren vertiefenden Untersuchungen an.

Frequently used abbreviations

2D two-dimensional

2DM two-dimensional material

AC armchair

BP black phosphorous

gr graphene

hBN hexagonal boron nitride

Ir(111) (111)-facet of iridium

LEED low energy electron diffraction

MBE molecular beam epitaxy

MX monochalcogenide

STM scanning tunneling microscopy

STS scanning tunneling spectroscopy

UHV Ultra high vacuum

QMB quartz mass balance

QMS quadrupol mass spectrometre

ZZ zigzag

Contents

Chapter 1

Introduction

In the pursuit of ever-advancing electronic devices and sensors, novel mechanisms are implemented to leverage diverse phenomenological characteristics. One example from the early 2010s is the introduction of ferroelectric memory devices into the commercial domain [1]. In this context, the newly introduced characteristic of ferroelectricity is directly linked to the crystal properties of the selected materials.

Ferroelectric materials exhibit a spontaneous electrical polarisation below their critical temperature. The orientation of the polarisation state can be manipulated by the application of an external electric field. This specific property allows these materials to not only be used as memory device but also in sensors, actuators, and optoelectronic devices [2, 3].

To further increase technological advancement, there is a drive for miniaturisation and, consequently, improved energy efficiency. This can be achieved by a reduction in film thickness. However, when the dimensionality is reduced significantly, the problem for ferroelectrics arises. The critical temperature becomes no longer practicable due to intrinsic depolarisation fields stemming from charged surfaces [4].

The ultimate level of thin film technology is reached with two-dimensional materials (2DMs). Since the first preparation of graphene (gr) [5], it became quickly the norm as a versatile material for multiple applications. However, the world of 2DMs is evolving with emerging members enabling new possibilities [6]. Nowadays, gr is used as a suitable semimetallic substrate due to its ability to achieve high-quality growth, chemical inertness, and low charge carrier density [7–9], especially within the domain of surface science.

Fortunately, recent entries to the two-dimensional (2D) world offer a solution to the problem conventional ferroelectric materials suffer from. 2DMs with in-plane ferroelectricity can exhibit a spontaneous polarisation at practicable temperatures, which is shown by a ground-breaking study where a critical temperature above room temperature was found [7]. The unique aspect for this phenomenon is that the polarisation is confined within the 2D plane. The absence of surface charges, in the form of dangling bonds, is an advantage, and possible, since the ferroelectric property originates from a parent bulk material with a layered crystal structure.

One of such bulk material classes are group-IV monochalcogenides which are characterised by the structural formula MX, with the metal (M = Ge, Sn) and chalcogen (X = S, Se, Te) atoms in a stoichiometric ratio [10, 11]. These materials quickly gained prominence, with single layers forming puckered sheets and an orthorhombic crystal structure, which is closely related to phosphorene [12]. This crystal structure lacks inversion symmetry, which is a requirement for ferroelectric materials. For this crystal structure, this results in tilted dipoles in the unit cell which then add up to a total in-plane polarisation while the other components compensate each other. At tempera-

tures above the critical temperature, the tilting of these bonds vanishes, such that the net polarisation is compensated to zero. Theoretical investigations of these materials confirm strong ferroelectric properties [13–16]. An advantage for device fabrication is that all these materials are semiconductors, contributing to their straightforward integration into logical circuits.

Although numerous theoretical contributions exist, experimental work remains still relatively scarce. This fact can be attributed to the challenges in material preparation [9]. Nevertheless, MX monolayers are promising candidates for devices, such as non-volatile memories or ferroelectric tunneling junctions in modern transistors [7]. Designs for transistor devices with in-plane ferroelectric materials were already proposed [17]. These devices promise non-volatile memory functions with low power usage for fast read-out and writing performances while obtaining a non-destructive reading process.

For the sake of overcoming the aforementioned challenges in preparation, highly controlled conditions with a well-defined substrate are required. Molecular beam epitaxy (MBE) under ultra-high vacuum (UHV) conditions emerge as a viable option. This method uses the MX material in the form of powder or granules as the direct source, which eliminates the need for complex processes from multiple sources. This growth method also allows the formation of structures at nanometer scale. The preparation via exfoliation is impracticable due to relatively high exfoliation energies [9].

In this work, the preparation and characterisation of a various group-IV monochalcogenides are covered as ideal candidates for ferroelectric 2DMs. In order to contextualize and integrate the results into current research, chapters 2 and 3 offer necessary background information. Chapter 2 concentrates on the theoretical aspects of growth and possible mechanisms in the 2D regime, in particular edge reconstructions and relaxations. Additionally, this chapter aims to enhance the understanding of ferroelectricity and the investigated material class of group-IV monochalcogenides.

Chapter 3 discusses the experimental equipment, including the used UHV systems together with their primary characterisation tools, low energy electron diffraction (LEED) and scanning tunneling microscopy (STM), alongside the preparation methods.

Chapter 4 describes the growth of SnSe on graphene on iridium (Ir(111)) with particular emphasis on island shape. The morphology of the edges is also studied using first-principle calculations, provided by M. Ghorbani and A. Krasheninnikov (Helmholtz-Zentrum Dresden-Rossendorf). The experimental shape of the SnSe islands, together with the theoretical findings and atomically-resolved STM images of the edge are evidence for an edge relaxation in this system.

The focus of chapter 5 is on the intriguing bilayer formation of SnSe. This structure and its features are characterised and the first electronic measurements emphasise the complexity of such stacked system.

The difficulties of the MX preparation are exemplified in chapter 6 with the growth of GeSe, where amorphous structures on graphene substrates are presented as well as the first successful crystallisation in a different polymorph than typically discussed. The out-of-plane ferroelectric β-phase is explained in further detail along with the characterisation of this material.

In chapter 7, the material SnS is investigated and characterised. Initial insight and methods towards the experimental determination of the actual critical temperature are given.

Chapter 2

Theoretical Background

This chapter touches on the basic theoretical foundations of crystallography and crystal growth processes, including far from equilibrium conditions. These are conditions where the system is not in thermodynamic equilibrium and therefore does not posses a stable state with the minimum free energy. Typically, this is only the case for thin film deposition, while crystal growth only is considered in equilibrium [18]. Furthermore, this chapter covers the mechanics and importance of 2D reconstructions, the fundamentals of ferroelectricity, and the unique material class of group-IV monochalcogenides.

2.1 Growth far from equilibrium

Iso- and polymorphism of crystals provided early evidence that the shape of a crystal is due to the atomic building blocks in the form of crystal structures and not determined by specific chemical properties. This means that similar crystal shapes could be found for different materials, but also multiple shapes could be found for a single material. These phenomena can be directly observed in the different shapes of snowflakes, crystallising at various ambient conditions [18]. Fundamental studies resulted in the description of the atomic building blocks and therefore the derivation of all primitive Bravais lattices. These are lattices based on specific symmetries and the relationship between lattice vectors. There are 14 3D and five 2D Bravais lattices. 3D and 2D lattices are not linked by simple cuts through the unit cell, but are rather based on a mathematical principle for the arrangement of atoms. However, cuts can be described by a set of Miller indices (hkl), where h, k and l are integers and each represent a direction in space. In crystallography, a typical description is based on the reciprocal space, where a reciprocal lattice vector $\vec{a}^*$ is defined by $\vec{a_i} \cdot \vec{a_j}^* = 2\pi\delta_{ij}$. A plane in reciprocal space can then be described by $h\vec{a}^* + k\vec{b}^* + l\vec{c}^*$. The smallest unit cell in reciprocal space that contains the reciprocal lattice vectors is defined as first Brillouin zone.

The 2D Bravais lattices can be seen in fig. 2.1 (a)-(e). There are also other common 2D structures, like the honeycomb lattice found in graphene, shown in fig. 2.1 (f). For all 2D lattices here, the unit cell, and lattice vectors a and b are drawn in, in a similar way for the honeycomb structure as well.

The understanding of the growth can usually only be done from the development of models and imaging techniques. However, in-situ investigation is often hindered in the necessary time and resolution scale. Such knowledge on the atomic scale can make it possible to optimise preparation methods in order to achieve desired morphologies. For most fundamental cases of metal growth on itself, the processes as well as the significance of individual mechanisms are already available with the relevant quantitative parameters [18]. But especially in the realm of 2DMs, the discussion can be very limited with only few studies of the atomic processes during growth.
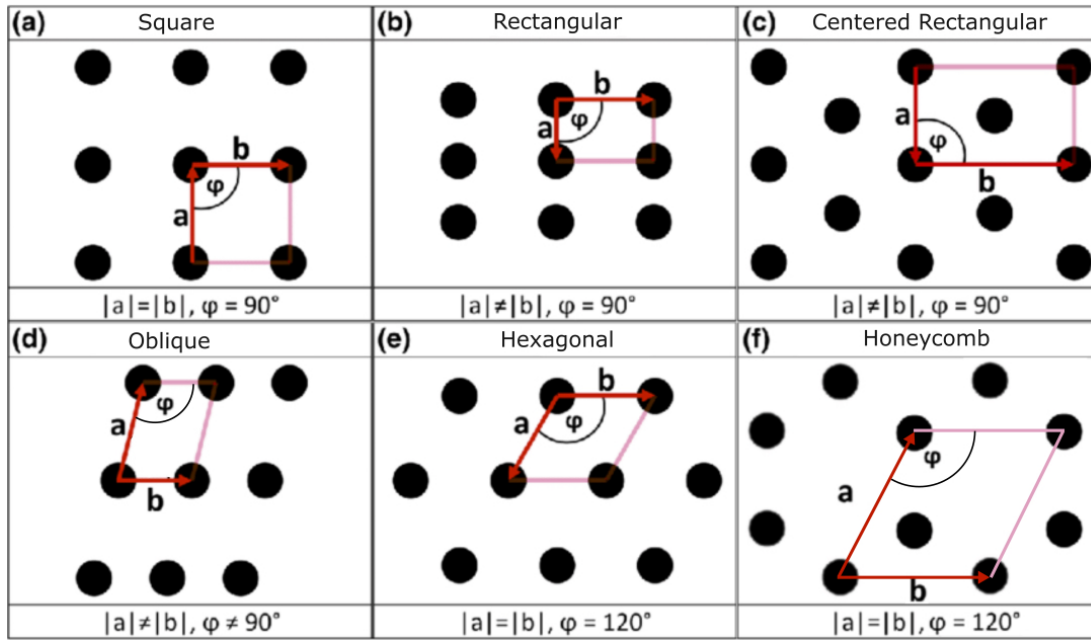
Figure 2.1: Summary of 2D lattices. (a) - (e) All five Bravais lattices are shown with drawn in unit cell, lattice vectors *a* and *b*. In (f) the honeycomb structure is presented in a similar way.

This regime of thin film deposition is a special case of epitaxial growth. The term epitaxy is used to describe the growth of a crystalline layer on a crystalline substrate with a certain orientation dependency on each other [18]. Typically the orientation of the deposited layer is determined by minimising the (energetic) constraint on the interface.
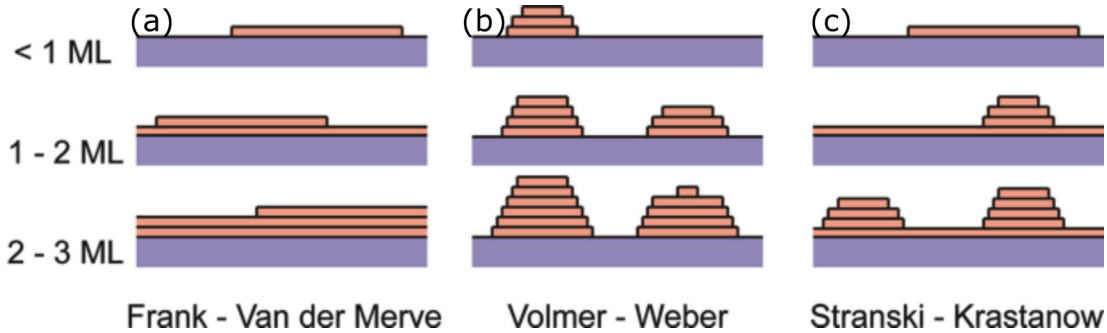

Figure 2.2: Schematic of different growth modes in dependence of layer thickness for the range sub-monolayer (top), 1-2 ML (middle) and 2-3 ML (bottom). The three modes (a) *Frank-Van der Merwe*, (b) *Volmer-Weber* and (c) *Stranski-Krastanov* are shown, adapted from [19].

Three initial states of thin film growth can be distinguished from conditions close to the thermodynamic equilibrium. The limiting factor is the consideration of the surface free energy of the substrate γ_S in comparison to the sum of interface free energy γ_{int} and surface free energy of the deposit γ_D. For a small value of γ_S, it is energetically favourable that the area covered by the deposited material is minimised. This mode is called *Volmer-Weber* growth and is illustrated in fig. 2.2 (b). In the opposite case, the deposit wants to maximise the area on the surface and grows layer by layer. This mode is called *Frank-Van der Merwe* growth, which can be seen in fig. 2.2 (a). The third case,

which is true for a balanced energy consideration, can only be achieved for $\gamma_S = \gamma_D$. This case is called *Stranski-Krastanov* growth and is only fulfilled for homoepitaxy [18]. Fig. 2.2 (c) shows this growth mode. It can be seen that the growth on the surface is preferred, but once no surface spot is longer available, the growth behaves similar to *Volmer-Weber*.

In order to distinguish conditions in equilibrium from far from equilibrium, a first indication are growth rates and substrate temperatures. Since the growth of single layer islands with specific interest in their shape and properties is in focus, this is usually not beneficial for sub-monolayer growth. For the growth of thin films highly controlled conditions are needed. For these conditions, other growth modes than the mentioned above are more relevant. In the kinetic growth regime, where the growth is influenced by external factors as temperature, rate and/or pressure, two main modes can be distinguished. Similar to the *Frank-Van der Merwe* growth mode, a layer-by-layer growth is achievable when surface diffusion is preferred. In the case of prohibited diffusion on the surface, the growth will behave in a statistical manner, such that any position on the surface available is treated with equal probability.

For thermally activated processes the *Arrhenius* law determines the rate ν of all relevant atomic mechanisms

$$\nu = \nu_0 \cdot e^{-\frac{E_a}{k_B T}}, \tag{2.1.1}$$

where ν_0 is the attempt frequency, E_a is the energy of the activation barrier of the process, k_B is Boltzmann's constant, and T is the temperature. Thermally activated processes can be identified for example in how the shape or the size of islands change when thermal energy is added to the system, like during annealing. These phenomena can be explained in terms of specific atomic processes. In the case of effective step edge diffusion, the shape can become more compact. The island can also decrease in size in the case of effective step atom detachment. Both processes, diffusion and detachment, can be characterised by a specific energy barrier, which will be different for each case and therefore a hierarchy of processes can be given. Thus, the resulting island morphology is typically in a complicated dependence on the annealing temperature. However, various regimes of dominating processes, which are all temperature-depended can still be distinguished, since the exponential relation of the rate ν activates different processes subsequently [18]. As an illustration, the rate for two different processes with an activation barrier energy difference of only 0.2 eV at an annealing temperature of 500 K differs by a factor of 100.

2.2 2D reconstructions

Surface reconstruction is a process that alters the crystal lattice of the topmost layer of atoms from the ideal equilibrium structure in the bulk. Such phenomena are present in electronically unstable systems, for example, due to dangling bonds [20], or when tensile stresses in the pristine surface are present [21]. One example for the latter phenomena is the Au(111) surface. The tensile stress is introduced by a lower coordination number of atoms on the surface than the bulk. In turn, a reconstruction of the surface enables to satisfy the energetically favoured arrangement of atoms of the surface to the bulk material. Since the reconstruction changes the lattice, this is directly visible in microscopy imaging. In the case of Au(111), the reconstruction compensates the offset of one extra atom in the surface layer per 22 lattice constants and manifests itself in a herringbone pattern [21]. The complete explanation for this exact shape on an atomic level was only achieved recently [21]. Generally, reconstructions are an important way to minimise energy and often play a crucial role in chemical, electronic, and shape properties.

This is not only a mechanism to reduce the surface energy in metals, but also for

2DMs in the form of islands, where step edges are usually in focus. Step edges are the boundaries of any island, recognisable in a top view with a terrace and lattice constant change. Here, we need to distinguish between two major processes: reconstructions and relaxations. While the former changes the lattice structure at the step edge from the ideal lattice in the interior of the island (2D bulk), relaxations alter bond length and bond angles but do not change the periodicity of the lattice.
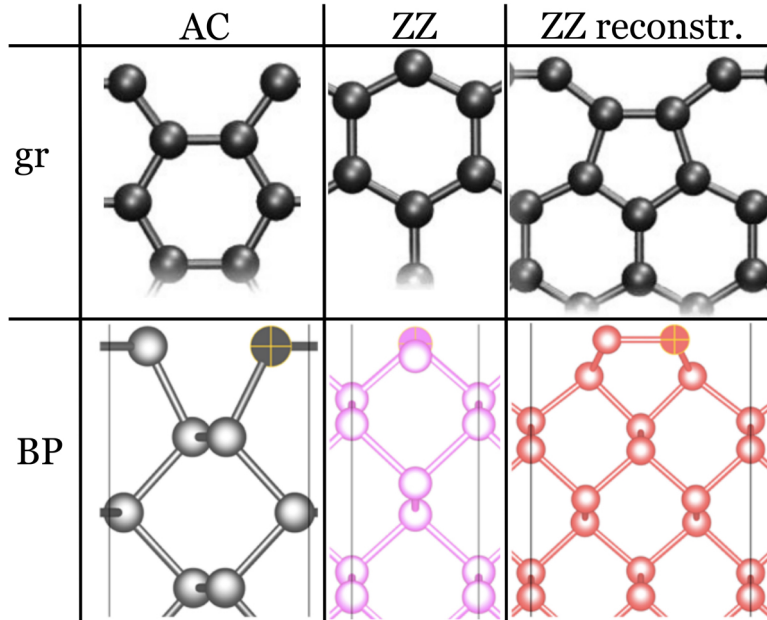

Figure 2.3: Examples of reconstructions in common 2DMs. Schematic drawings in a top view of armchair (AC), zigzag (ZZ) and reconstructed ZZ edge (ZZ reconstr.) for graphene (top) and black phosphorous (bottom), adapted from [22, 23]. The edge is perpendicular to the infinite structure and can be found on the top of the image. Further explanation of the reconstruction mechanisms is in the text.

As the first synthesised 2DM, gr is already intensely studied [5], especially the edge configurations. Gr forms a hexagonal lattice arrangement, which resembles the cells of a honeybee hive. Therefore this structure is also called honeycomb structure. It can be seen as a top view in fig. 2.3 in the 2D bulk area for gr. Possible edge configurations can be determined by a simple bond-counting and reducing the number of broken bonds. This cuts the structure such that the least number of broken bonds occur. Typically, this method results in the energetically favoured step edges, a material forms. For gr, two major edge options emerge: armchair (AC) and zigzag (ZZ). While AC is named in accordance to the shape resembling the armrest of a chair, zigzag can be described by alternating up- and downward tilted bonds. Both can be seen in fig. 2.3 in a top view, where the edge is perpendicular to the infinite structure and can be found on the top of the image.

For simplicity reasons, the focus of this chapter is set to reconstructions on ZZ edges. The underlying mechanism for gr is a ZZ57 reconstruction where a pentagon and a heptagon are formed. The lattice changes from rings with six carbon atoms to a structure with alternating five- and seven-atom rings at the edge. The reconstruction is due to a dangling bond on every second atom at the edge, which only has two neighbouring atoms instead of three. In order to reduce the total energy, the system changes into pentagon rings, where all bonds are satisfied and heptagon rings with now two unsatisfied carbon atoms at the edge next to each other to compensate. Such a structure also widens the bond angle, which further decreases the energy in the system [22]. This is visualised in

fig. 2.3 in the top row. The ZZ57 reconstruction allows the material to reduce its step edge energy by 8% from its unreconstructed ZZ edge at $1.29\,\text{eV/Å}$ [22].

Hexagonal boron nitride (hBN) is structurally very similar to gr. The difference is that it consists of alternating boron and nitrogen (instead of only carbon) atoms in the same honeycomb structure [24]. They are isostructural to each other. It can also be classified with ZZ and AC edges. But for each edge type, there are two terminations possible because of its binary composition. As an example, the unsatisfied atom in ZZ can be B or N, resulting in B or N termination of the edges, respectively. While hBN would be a good candidate to compare charge effects on reconstructions to the neutral gr, the possible reconstruction options are more complex due to the edge terminations. The formation of a boron terminated ZZ57 edge is energetically favoured than a nitrogen one, and reduces the energy by up to 8% compared to the unrelaxed B terminated edge [24, 25]. This is on the same scale as for gr. Though in a simple picture, a larger effect would be expected, since not only the unsatisfied bond but also the resulting charged edge would increase the step edge energy. However in reality, the material undergoes a reconstruction, which changes the structure at the edge in dependence of the neighbouring termination of edge. This complex reconstruction allows a step edge energy gain of up to 24% [25], which now even surpasses the energy gain of gr in comparison. Such strong reconstructions are not seen in gr and have to be due to the polar nature of hBN. In any case, a direct comparison between gr and its binary counterpart hBN is difficult due to the different mechanism and further structural refinement options which are not available for gr. Hence, it will not be included further.

Another commonly available 2DM is black phosphorus (BP), an allotrope of phosphorus, which exhibits an orthorhombic structure. This structure is defined by a rectangular unit cell, which consists of two atoms in a cell of only right angles but unequal lattice constant lengths. The lattice can be seen in fig. 2.3. In a simple view, it also has resemblance to a hexagonal ring which is buckled such that two atoms are nearly on top of each other. For this material, the preferred edge is also a reconstructed ZZ edge, which allows a step edge energy reduction of 50% compared to the unreconstructed ZZ edge ($0.40\,\text{eV/Å}$) [23]. The mechanism also involves the atoms at the edge to shift outwards (ZZo) and form a five-atom ring, which is similar to the gr reconstruction. Due to the strong buckling of the lattice no heptagon is formed, since this would increase the bond angle and therefore also increase the total energy. The top view of the BP lattice with AC, ZZ and reconstructed ZZ edge can be seen in Fig. 2.3 bottom.

Group-IV monochalcogenides like SnSe, are isostructural to BP. Similar to the difference between gr and hBN, SnSe with its binary composition results in different partial charges for each atom sort. This even results in a polar field across the material, which also drives this system even more to allow reconstructions to take place. In this specific case, a relaxation of the ZZ edge reduces the step edge energy by up to 56% from the non-relaxed form ($0.231\,\text{eV/Å}$).

A comparison of the different energy gains of gr, BP and SnSe due to reconstruction in their ZZ edge is presented in fig. 2.4 as percentage reduction. The unreconstructed bar at 100% represents the pristine state, while each material is given as percentage to its unreconstructed edge with its mechanism. This shows on the one-hand side that reconstruction/relaxation mechanisms are an efficient form to reduce edge energy. On the other-hand side, it demonstrates that more complex systems (either due to polarity or crystal structure) tend to have larger energy gains and are therefore more likely to undergo reconstruction/relaxation mechanisms.

Generally, 2D reconstructions and relaxations represent deviations from the ideal structure and are influenced by various factors, as shown here for dangling bonds, buckled structure, and a combination of a polar and buckled structure. The study of
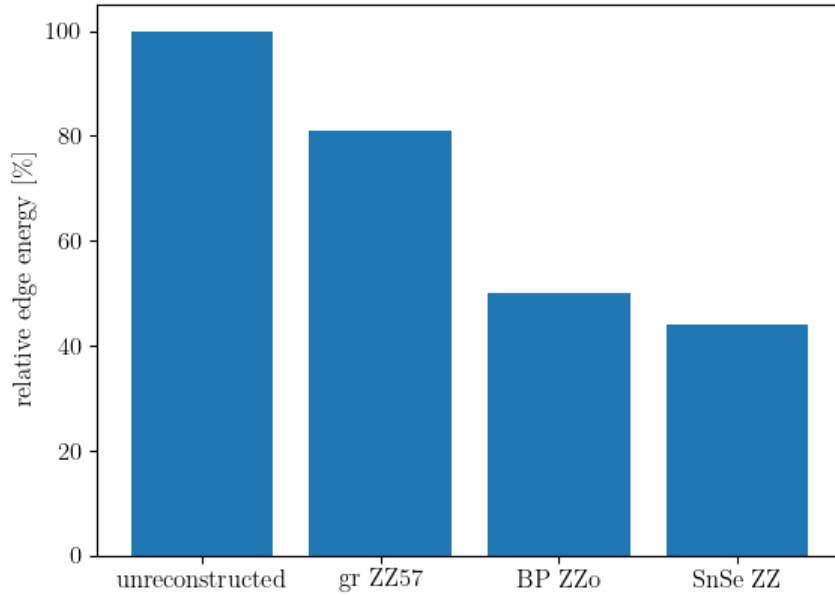
Figure 2.4: Representation of energy gain of different 2D materials due to edge reconstruction mechanism at the ZZ edge, represented as relative edge energy normalised by the unreconstructed structure, expressed as a percentage. Graphene (gr) exhibits a 57-reconstruction at the zigzag edge with an energy gain from $1.29\,\text{eV/Å}$ to $1.19\,\text{eV/Å}$ [22, 26]. Black phosphorus (BP) also gains from $0.40\,\text{eV/Å}$ to $0.20\,\text{eV/Å}$ at the zigzag edge due to reconstruction shifting atoms outwards (ZZo) [23]. For SnSe, this mechanism could alter the zigzag edge by which the step edge energy changes from $0.23\,\text{eV/Å}$ to $0.10\,\text{eV/Å}$.

such step edges is important since not only chemical properties like reactivity alter but also because the energetically preferred step edge and therefore island shape are often linked to other major physical properties like, for example, ferroelectricity [27, 28].

2.3 Ferroelectricity

The first ferroelectric material investigated was potassium sodium tartrate, also known as Rochelle salt, in 1920 by Valasek. While investigating this material, he found out that the electrical polarisation P increases with increasing external electrical field. However, when the external field is subsequently turned off, the polarisation does not vanish, but a permanent electrical polarisation, also called spontaneous polarisation, is present. This implies a hysteresis effect, which is also known in ferromagnetism [29]. Although neither Rochelle salt nor most ferroelectric materials contain iron, the prefix ferro- was chosen to emphasise the similarities in properties to ferromagnetism. Materials exhibiting ferroelectricity, -magnetism, and/or elasticity are called multiferroics.

As a clear definition, a ferroelectric material exhibits a spontaneous polarisation, which is present within the material without any external influence. However, the polarisation direction can be reversed by the application of a suitable external electrical field.

Electrical polarisation is defined by the change of microscopic dipole moments ($\vec{p}$) per volume (V):

$$\vec{P} = \frac{\vec{p}}{V_{\text{island}}}. \tag{2.3.1}$$

In order to treat ferroelectricity as an intrinsic material property, all ferroelectric materials do need a non-centrosymmetric crystal structure, where atoms lack any

inversion center, and a charge difference within the unit cell. This results in a dipole moment per unit cell. These rather strict requirements lead to the interesting fact that all ferroelectric materials also have an electrical response due to mechanical stress (piezoelectricity) and to temperature change (pyroelectricity).

There are also other materials exhibiting ferroelectric behaviour which are based on organic compounds. The basis here is typically not due to individual dipole moments, but rather from displacements in non-covalent molecules or the charge transfer as a collective layer [30].

Macroscopically over a larger area, it often occurs that both ferroelectric states exist in one material. These distinct regions within the crystalline structure are called domains. Each of them have a specific orientation of the microscopic dipoles and are separated by domain walls as borders. There is an associated energy to form such borders, whereby the shape and size of domains can be affected.

Since two polarisation states are generally obtainable, this means the energetic landscape expresses two minima. Each domain can also switch their polarisation state. For this switching, the energy barrier needs to be overcome thermally, electrically or by mechanical stress. Subsequently, either parts, or the whole domain switches its dipole orientation. It is also possible that domain boundaries macroscopically move within the material, with a suitable switching mechanism which manipulates the dipole orientation, originating from one specific direction.

Ferroelectric materials only exhibit spontaneous polarisation when the temperature is below the critical temperature T_C. This temperature is also called Curie temperature, in analogy to ferromagnetism. Above this temperature, the materials changes to a paraelectric phase, where no spontaneous polarisation is present. However, a polarisation can still be induced by an external electrical field.

In order to mathematically describe systems close to phase transitions, the Landau theory is generally considered [31, 32]. It focuses on a macroscopic order parameter and its free energy expression. This model takes the symmetry-breaking terms into account but neglects higher order terms or critical exponents. The extension of the Landau theory developed by Ginzburg and Devonshire is created to also describe the change in order parameter, especially in the case of ferroelectric and -magnetic materials. The Landau-Ginzburg-Devonshire (LGD) theory helps to frame the spontaneous polarisation in the ferroelectric-paraelectric transition near the phase transition point T_C [31]. The total free energy F can then be expressed by polynomial terms

$$F = F_0 + \frac{\alpha_1}{2} \cdot P^2 + \frac{\alpha_2}{4} \cdot P^4 + \frac{\alpha_3}{6} \cdot P^6 + ..., \qquad (2.3.2)$$

where F_0 is a constant term and α_i are material-specific constants, which are temperature and/or pressure dependent. This expression is truncated here to the sixth term. The most dominant material-specific constant can be expressed as

$$\alpha_1 = \frac{1}{\epsilon_0 C(T - T_C)}, \qquad (2.3.3)$$

where ϵ_0 is the permittivity of free space and C is the Curie-Weiß constant.

Close to the transition, the difference $(T - T_C)$ becomes negligible small, therefore higher order terms can be ignored. With $\partial F / \partial P = 0$ and elegant mathematical transformation, the Curie-Weiß law follows. This results in an expression for the polarisation P

$$P = P(0\,\text{K}) \cdot \left(1 - \frac{T}{T_C}\right)^\gamma \text{ for } T < T_C, \qquad (2.3.4)$$

where $P(0\,\text{K})$ is the polarisation at $0\,\text{K}$, therefore the maximal achievable spontaneous polarisation value, and γ is the critical exponent. For temperatures above T_C, the

polarisation is zero.

Another expression follows from the second derivative of the free energy F. For temperatures close to the transition temperature, the maximum spontaneous polarisation behaves proportional to said transition temperature

$$P_\mathrm{S} = (\alpha_s(T_\mathrm{C} - T))^{1/4}\,, \tag{2.3.5}$$

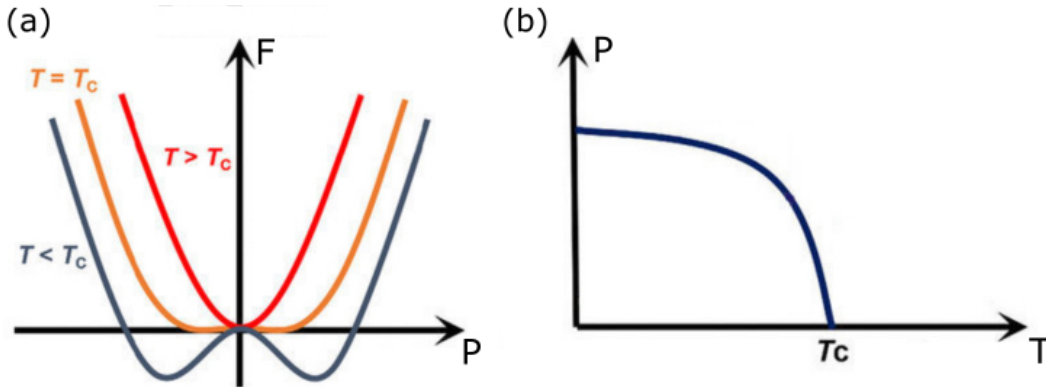with a material constant α_s.

Figure 2.5: Electrical polarisation in dependence of the critical temperature T_C. (a) The free energy landscape shows two possible polarisation minima at $T < T_\mathrm{C}$, which vanish for higher temperatures. (b) The second-order transition of polarisation in dependence on temperature with its characteristic sudden drop close to T_C is shown, adapted from [20].

The two correlations for free energy and polarisation in dependence of temperature are illustrated in fig. 2.5 (a) and (b), respectively. From the mathematical expression, the free energy landscape in dependence of polarisation has two minima for temperatures below the critical temperature, which is directly correlated to the two ferroelectric states and the energetic barrier between them (blue curve in fig. 2.5 (a)). With increasing temperature, the difference $(T - T_\mathrm{C})$ becomes smaller. Close to the transition temperature higher order terms can be neglected, such that the minima vanish (orange curve). At even higher temperatures, the free energy can be described as proportional to P^2, as seen in the red curve. Fig. 2.5 (b) demonstrates a typical second order transition in dependence of temperature. Here, the parameter polarisation does not alter significantly in a wide temperature range. Close to the transition temperature, a rather abrupt change in the macroscopic order parameter is seen. At even higher temperature, the spontaneous polarisation is zero.

However, as practical as these mathematical expression regarding electrical polarisation are, real world applications and problems are not discussed. Most ferroelectric layers do have charge recombinations when the film thickness becomes to thin, which sets a limit to the effective layer thickness. Although ferroelectric devices promise excellent properties, most advances can not scale in the same rate as silicon device technology trends due to this material dependent layer thickness limit. Typical occurring problems are connected to create a sufficient minimal domain size for single domain devices, the preparation of defect-free films to prohibit charge recombinations, and the onset of out-of-plane depolarisation fields or leakage currents. The appearance of these currents is often linked to small bandgaps or Schottky barrier heights. Since these two properties are strongly dependent on material characteristics, there is not much variation possible. A typical used ferroelectric material for devices is HfO_2. For optimal tuning of such characteristics, this material is doped with various metals, in order to achieve higher

polarisation values, but also larger Schottky barrier heights [33].

Due to depolarisation fields, the critical thickness of perovskites, another typically used ferroelectric material, is limited to 24 Å [15]. In order to mitigate the problems which occur in downsizing of 3D ferroelectrics, the world of 2D materials, especially layered systems, offers new opportunities.

2.4 Group-IV monochalcogenides

The last years have seen a steady increase in new materials in the 2D world [34], especially since the first isolation of a single graphene layer [5]. A rather new semiconducting candidate emerged with the layered group-IV monochalcogenides (MXs) which are environmental friendly and use earth abundant elements. This class of materials gained attention due to the theoretical prediction of promising properties for several applications [35]. MXs are materials consisting of a transition metal atom and a chalcogen with the chemical formula MX, where M = (Si, Ge, Sn) and X are chalcogens. Strictly speaking, all group VII atoms are considered chalcogen atoms, but typically the elements sulfur, selenium, and tellurium are meant. Due to the layered structure, individual properties are still present when the dimensionality is scaled down to the monolayer. These semiconductors typically form an orthorhombic crystal structure, see fig. 2.6, which is isostructural but also -electronic to group-V semiconductors like black phosphorous. Such structures have a broken inversion symmetry and therefore very low crystal symmetry [15, 36, 37].
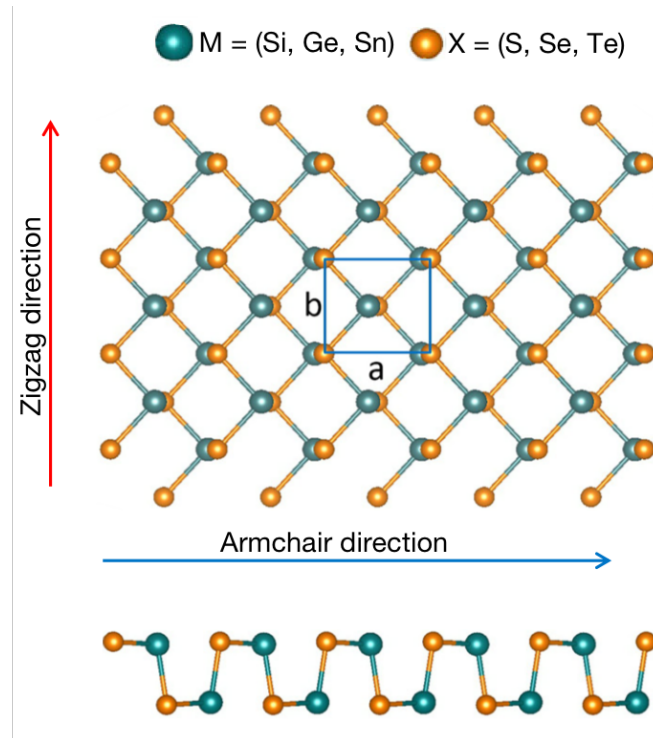

Figure 2.6: Schematic of the orthorhombic atomic structure of MXs in top-view aligned to the lattice vectors a and b in AC and ZZ direction, respectively. Metal atoms are green, while chalcogen atoms are orange. The unit cell entails in total four atoms of two different layers and therefore the lattice constant c does not correspond to layer thickness d. Underneath is the corresponding side-view shown. [15].

Orthorhombic crystals can be described by their unit cell with lattice constants $a \neq b \neq c$

and corresponding angles between each lattice constants $\alpha = \beta = \gamma = 90°$. The rectangular unit cell results also in a rectangular first Brillouin zone. Within this unit cell, monochalcogenides usually obtain a puckered lattice, which belongs to the space group Pnma 62, which can be seen in 2.6 as top-view (top) and as corresponding side-view (underneath). Each M atom bonds to three X atoms with different bond lengths and vice versa. Two of those are related by symmetry and therefore the same. The resulting monolayer extends over two atomic layers that are separated by distance d from the next monolayer. Using this nomenclature, the unit cell itself contains four atomic layers and such two monolayers. In a very simplistic model, the lattice could be described as a complex hexagon which is folded together in one direction, such that the puckered lattice results. Therefore, similar to hexagonal lattices, a clear AC and ZZ direction can be identified, which is indicated in the schematic view of the MX lattice in fig. 2.6. This puckered lattice structure enables novel physical phenomena due to its reduced symmetry in comparison to already intensely studied 2DMs with different crystal structures like graphene or transition metal dichalcogenides like MoS_2. This phenomena is also known as Neumann's principle. In principle, it states that the symmetry of physical properties is linked to the symmetry of the crystal class, enabling interesting features in systems with reduced symmetry [38].

As indicated in the schematic drawing for a monolayer in fig. 2.6, the layered nature of this material class results that also multiple stacking possibilities are available. The stacking in the bulk material resembles the type AB, where the upper layer is only mirrored by 180°, see fig. 2.7 (c). However, theoretical studies for MX and also for the isostructural black phosphorus suggest that there are more options in reduced dimensionality [39–41]. In stacking cases, where the upper layer is rotated, or has a different periodicity as the other one, the moiré effect can be observed, when the layer is partially opaque in terms of the specific measurement technique. This effect results in a large scale interference pattern which is not entailed in any of the base periodic structures [18]. Such a superstructure can be seen in many examples, like in scanning probe microscopy for the graphene lattice on the hexagonal (111)-plane of Ir, which has a different lattice constant resulting in a moiré superstructure.

As a result of the broken symmetry, few-layer MX are reported to express higher anisotropic electronic responses than existing 2D materials [36]. For optical devices, the absorption spectra also exhibit strong anisotropy with excitonic gaps [37]. One particular example is bulk SnSe, which can be used as a high-performance thermoelectric material [42]. These features are expected to stay present in the monolayer regime.

One of the most interesting features of MX materials is a large in-plane spontaneous polarisation as predicted theoretically [15, 43, 44]. Another important advantage to the size of this intrinsic effect is that the stability is not dependent on out-of-plane depolarisation fields and therefore film thickness [37]. Such behaviour can be realised in this material class due to the layered structure of bulk parent material. Each layer itself expresses a dipole moment independently of the other layers, which then can result in a collective polarisation of the structure. This is possible because of the ionic bond and therefore slight difference in charges, where each M atom is positively and X is negatively charged.

In a more symmetric puckered lattice where each atom of the upper atomic layer is exactly on top of the one from the lower layer, which can be seen in fig. 2.7 (b), all the ionic bonds would compensate each other. However, due to differences in bond angle, this is not the case for MX. In order to determine the orientation of the polarisation, the structure can be seen as a compound of individual dipoles. Each dipole is set between an atom of the upper and one of the lower layer. This results in electric dipole moments either pointing up- or downwards with a slight angle. This angle can be introduced as
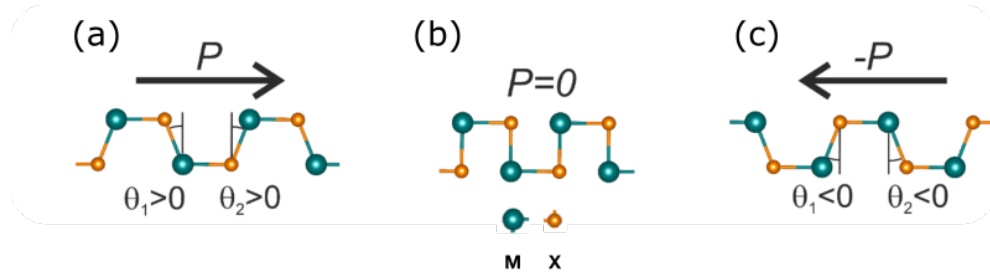
Figure 2.7: Schematic of polarisation orientation of MX. The orthorhombic structure is shown with bond angles θ_1 and θ_2. In (a) these angles are per definition positive, resulting in a total polarisation to the right direction. In (c) the structure is mirrored, such that these angles are negative with a resulting polarisation to the left direction. (b) represents the paraelectric state where the angles are zero, resulting in no net polarisation.

the angle of the bond between both atoms, which can be seen in fig. 2.7 with θ_1 and θ_2. If said angles are non zero, each of the dipole moments have a slight component parallel to the AC orientation, while the component in c-direction is cancelled by another dipole. The polarisation orientation is the same as the orientation of the total dipole moment. The case with positive bond angles is shown in (a) resulting in a polarisation to the right. The opposite direction is achieved by a mirrored structure, which results in negative bond angles, as presented in subfigure (c), as well as in fig. 2.6. This simple demonstration directly leads to two stable configurations of differently orientated polarisation. MX are therefore ferroelectric materials, conceptionally only for monolayer structures. The transition phase, where the bond angles are zero, is shown in fig. 2.7 (b). Such a configuration leads to no net polarisation and is thus paraelectric.
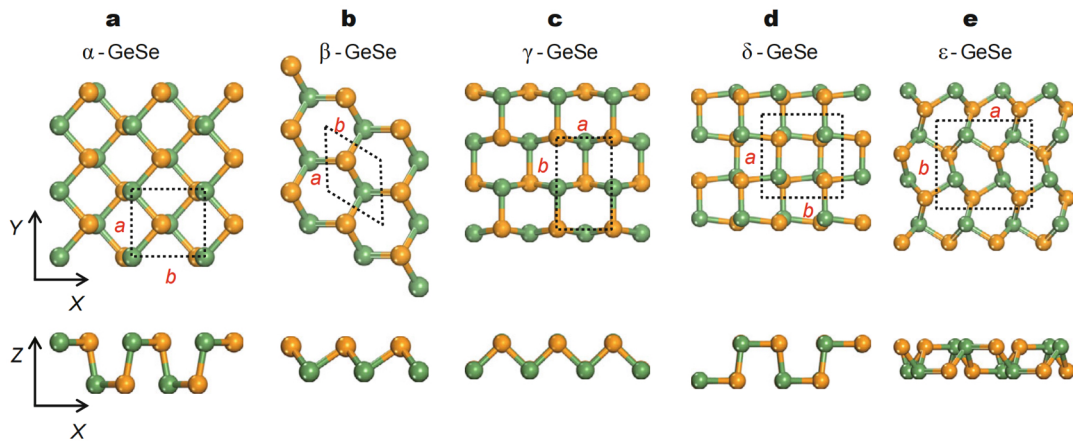

Figure 2.8: Schematic structures of the five stable MX polymorphs presented in the form of GeSe, while Ge is green and Se is orange. For each phase top- (upper) and side- (lower) view is shown with a unit-cell and lattice constants a and b drawn in, adapted from [35].

Although the bulk parent of each MX material always forms an orthorhombic lattice, theoretical studies show that there also other stable forms for monolayer growth. Fig. 2.8 presents five stable phases, which were theoretically predicted for GeSe, but can be generalised for all MX materials. As a convention the orthorhombic structure is called α-phase, which can be seen in subfigure (a) and was discussed previously.
The β-phase is a buckled hexagonal structure, where the lattice constants $a = b$ are

equal, shown in fig. 2.8 (b). The buckling results in one atom sort being closer to the surface underneath than the other and in a net dipole momentum in out-of-plane direction. Therefore, this phase can also be considered ferroelectric.

The γ-phase (subfigure (c)) differentiates itself from the β-phase, such that this phase is in another hexagonal conformation, resulting in different lattice constants a and b. The δ- and ϵ-phases, shown in fig. 2.8 (d) and (e) respectively, are structurally more complicated, but still resemble a similar orthorhombic lattice like the α-phase.

Material	gr	hBN	MoS_2	$MoTe_2$	GeSe	SnS	SnSe
E_{exf} [meV/Å^2]	17.1	18.2	18.2	21.7	30.3	34.6	40.4

Table 2.1: Exfoliation energies E_{exf} of various conventional 2D materials and three MXs [9]. A significant increase in energy from other materials to MX could be seen, also from other ferroelectric materials like $MoTe_2$.

In contrast to the theoretical prediction of multiple polymorphs, adequate experimental monolayer growth is quite hindered, due to high exfoliation energies E_{exf} compared to other 2DMs, see table 2.1, whereas other two-dimensional materials, like gr have up to 50% less exfoliation energy. It can be noted that even compared to other ferroelectric materials like $MoTe_2$, the exfoliation energies of MX are higher [9]. This makes the experimental approach to monolayer growth more difficult. But in order to achieve the theoretically predicted characteristics of these 2D MXs, a bottom-up method in a very controlled environment, like MBE in UHV, is an adequate starting point. The following thesis will concentrate on the experimental preparation of three of this material class, namely SnSe, GeSe, and SnS, via MBE in UHV chambers.

Chapter 3

Experimentation

In order to frame experimental results into context, it is important to understand the technical possibilities and limitations of modern surface science techniques. This chapter should give a basic overview of the used methods, starting with the two main techniques, low energy electron diffraction (sec. 3.1), followed by scanning tunneling microscopy (sec. 3.2) and spectroscopy (sec. 3.3). Then, it focuses on the different ultra-high vacuum setups with their components (sec. 3.4) and lastly common preparation methods (sec. 3.5), which are used throughout many experiments.

3.1 LEED

Diffraction methods are powerful techniques to investigate structural properties, especially in crystallography. Electron diffraction is based on the wave-like behaviour of electrons which interact with atoms of a sample leading to elastic scattering and diffraction of these waves. These electrons can be described by their de Broglie wavelength

$$\lambda = \frac{h}{p} = \frac{h}{\sqrt{2m_e E}},\tag{3.1.1}$$

with Planck's constant h, momentum p, electron mass m_e and energy E.
In order to use a non-destructive and surface-sensitive technique, wavelengths in the typical atomic length scale $(1 - 2\,\text{Å})$ are used. Therefore low energy electron diffraction (LEED) uses energies in the range up to $200\,\text{eV}$ to be most sensitive for the topmost layers.
An electron beam is generated by a cathode and is then collimated by a Wehnelt collimator cylinder and electric lens apparatus. The beam is then accelerated towards the surface of a grounded sample with a potential difference of $-V$. At the surface, the electrons scatter with a periodic structure. Backscattered electrons then travel in a field-free space, since there is no potential difference between the sample, first and fourth grid. Through a $-(V - \Delta V)$ potential difference at grids 2 and 3, inelastically scattered electrons are filtered. Afterwards the electrons are again accelerated and later detected on a hemispherical fluorescent screen which is typically at a voltage of $3.5\,\text{kV}$. The setup can be seen schematically in fig. 3.1 (a). Due to this geometry, the electron gun can always be seen in LEED images, like in the example LEED image in fig. 3.1 (b). The first-order reflexes of gr (one is highlighted in blue), Ir (red) and of the moiré superstructure can be seen, while the zeroth order spot is hidden due to the electron gun.
The underlying physical principle is based on the Laue condition for elastic scattering

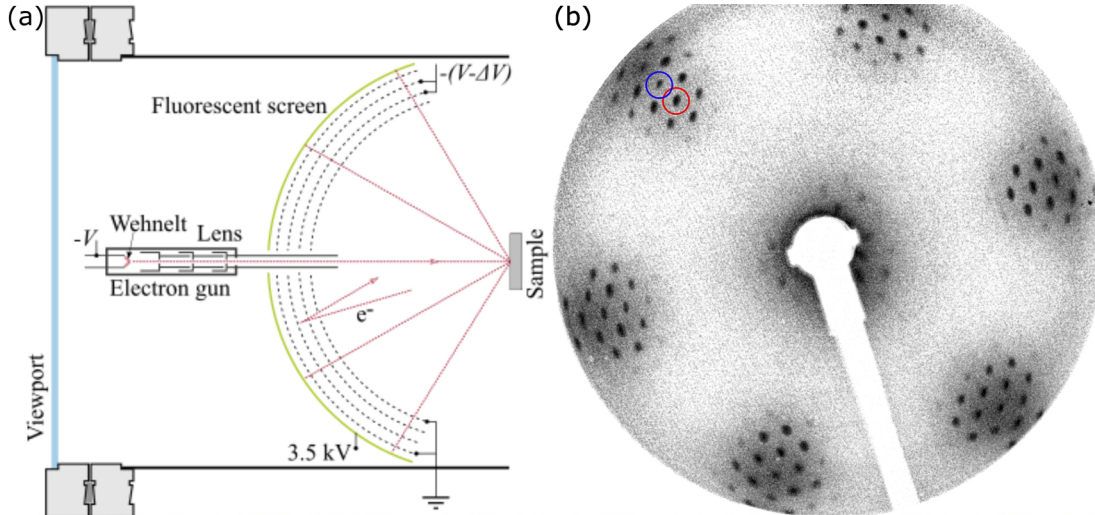$$\vec{k}_\sigma - \vec{k}_\nu = \vec{G}_{hk},\tag{3.1.2}$$

Figure 3.1: Low energy electron diffraction: (a) schematic drawing of a four-grid setup where electrons of the electron gun and focusing apparatus are accelerated to the sample and diffraction pattern detected on the fluorescent screen, adapted from [45]. (b) Diffraction pattern of gr/Ir(111) at 70 eV, while one reflex spot of Ir (red) and gr (blue) is highlighted. The contrast is inverted and will be for all images following.

with the scattered wave vector $\vec{k}_\sigma$, the incident wave vector $\vec{k}_\nu$, and the reciprocal lattice vector $\vec{G}_{hk}$. This condition for constructive interference is therefore only fulfilled, if the difference of the wave vectors parallel to the surface is exactly equal to the reciprocal lattice vector.
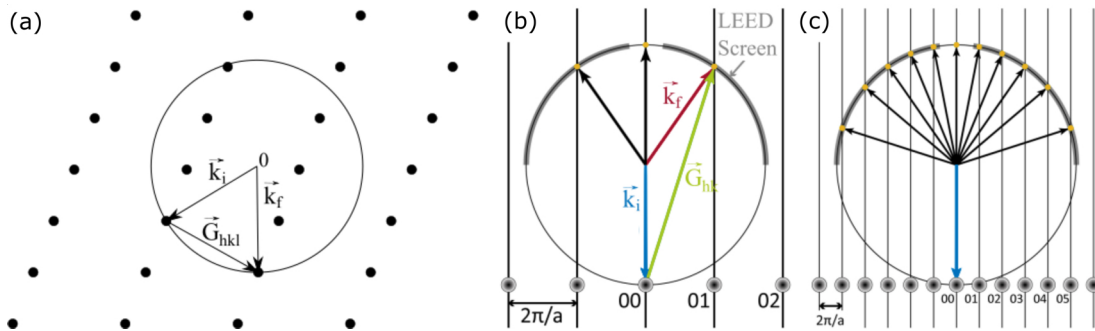

Figure 3.2: Ewald construction for diffraction in (a) 3D and (b,c) 2D. The Ewald sphere is constructed such that all lattice points which intersect the sphere fulfil the Laue condition of eq. (3.1.2.). The constructed Ewald sphere in the reciprocal space together with the wave vectors of the incoming electrons $\vec{k}_i$, of the scattered electrons $\vec{k}_f$, and the reciprocal lattice vector $\vec{G}_{hkl}$ with the Miller indices hkl are shown. The energy of the electrons in (c) is higher than in (b), resulting in a larger sphere and therefore more LEED reflexes. Adapted from [45, 46].

Geometrically, this can be realised by the Ewald construction, as visualised in fig. 3.2: an Ewald sphere can be constructed such that the Laue condition is fulfilled when the difference of $\vec{k}_\sigma - \vec{k}_\nu$ is exactly a reciprocal lattice vector $\vec{G}_{hkl}$. In subfigure (a), such a three-dimensional sphere is placed in reciprocal space so that the radius $|\vec{k}_\nu|$ terminates at lattice points. Due to low energies and therefore small penetration depths, typically a 2D lattice is assumed which consists of only wave vectors parallel to the surface. This alters a 3D lattice and introduces an infinite periodicity in orthogonal direction which

results in infinitely dense reciprocal lattice rods. Therefore, all diffraction spots are points where the Ewald sphere intercepts the rods, as shown in fig. 3.2 (b) with the corresponding Ewald sphere. At higher incident electron energy, the radius of the sphere increases, resulting in more visible diffraction reflexes, see subfigure (c) [47].

Superstructures of two different patterns in LEED images can be described by the Wood notation. The basis vectors of the superstructure are given as multiples of the basic lattice. Rotated superstructures are indicated by R and the angle between the two patterns [47].

Optical aberrations, distortions and systematic errors can limit the resolution of lattice constant determinations with LEED images. Calibration with very well-known crystal structures such as the 7×7 - Si surface can prevent this, but does not increase resolution significantly. For further insights, the work of [48] is referred.

3.2 STM

Scanning tunneling microscopy (STM) is a tool that shaped surface science. For this invention, Gerd Binnig and Heinrich Rohrer were awarded the Nobel Prize in Physics in 1986. The technique is based on the quantum tunneling effect. This effect makes it possible that a current flows between two electrodes separated up to a nanometer distance, when a bias voltage is applied, see schematic in fig. 3.3 (a). In this scenario, the electrodes consist of the surface to be examined and a metallic sharp tip. Ideally, then the current flows from the last atom on the tip to one atom on the surface, which in turn can provide atomic resolution [49]. The tip is attached to a piezoelectric motor, which consists of three individual piezoelectric transducers. Each of them is perpendicular to the other. The piezoelectric material contracts or expands when a voltage is applied, thus the tip can experience a movement in any direction. The tip itself is made of $99.9\,\%$ pure tungsten wire, because of its large electrical conductivity.

In order to describe the tunneling effect, different approximations can be used. In the
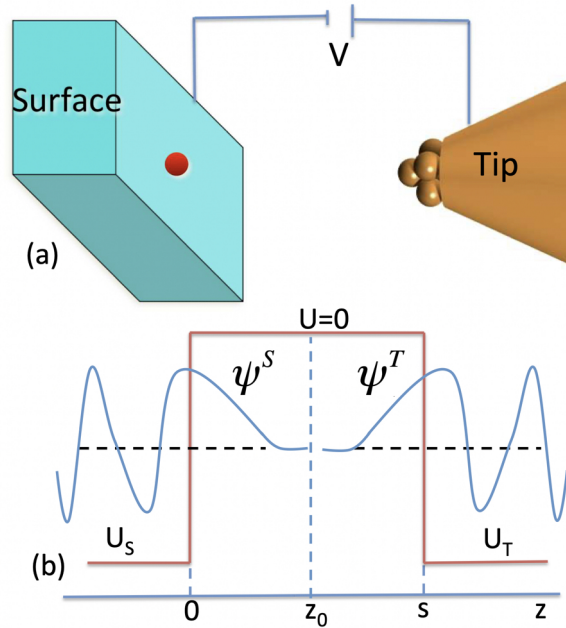

Figure 3.3: (a) Schematic view of a simplified STM with bias voltage V applied between tip (T) and conducting surface (S). (b) The tunneling effect is visualised with a simple one-dimensional barrier. The two wave functions Ψ decay into the vacuum, adapted from [50].

simplest model, a square potential can be assumed, which can be seen as an energy barrier due to the spatial gap. In the case of tunneling in STM, two electrodes are separated by this gap: the unperturbed substrate (S) and the free tip (T). A free electron can be found at the surface of the sample and at the topmost position of the tip, which is visualised in fig. 3.3 (a). When the distance between the two electrodes is large enough, each wavefunction satisfies the Schrödinger equation:

$$i\hbar\frac{\partial}{\partial t}\Psi^i = \left(-\frac{\hbar^2}{2m}\frac{\partial^2}{\partial z^2} + U_i\right)\Psi^i,\qquad(3.2.1)$$

where U_i is the potential function of either electrode i (S or T) and the wave function Ψ^i is dependent on time and spatial coordinates. In this case, as shown in fig. 3.3 (b), the wave functions resemble an oscillating wave outside the barrier and decay exponentially into the barrier.

When the distance between tip and substrate is reduced, the Schrödinger equation will contain the full potential $U_i \to U_T + U_S$. Therefore the approximations can be made that only one electron state at the energy ϵ is considered, that the tip and sample are described as free electrons and any electronic structure of both electrodes is neglected. This satisfies the semi-classical Wentzel-Kramers-Brillouin approximation. In this approach, the exponential decay of the transmission factor T in a potential barrier is given as probability of an electron tunneling through an effective barrier. The barrier height is then dependent on the work functions Φ_i of the tip and sample along with the applied bias voltage V. This results in the proportionality

$$T \propto \exp\left[-2d\sqrt{\frac{2m}{\hbar}\left(\frac{\Phi_T + \Phi_S}{2} + \frac{eV}{2}\right) - \epsilon}\right],\qquad(3.2.2)$$

where d is the tip-sample distance and ϵ the energy for the tunneling electron. The bias voltage shifts the Fermi level such that a tunneling current I occurs:

$$I = \frac{4\pi e}{\hbar}\int_0^{eV}\varphi_T(\epsilon - eV)\varphi_S T(\epsilon, V, d)d\epsilon,\qquad(3.2.3)$$

with the density of states φ_i.

Fig. 3.4 visualises the tunneling junction during STM measurements. The density of states (DOS) φ of tip and sample affect the tunneling current. The states in the sample can be shifted when a voltage difference is applied. In this specific case shown, the bias voltage is positive and shifts the unoccupied states of the sample downwards by $e \cdot V$ in regards to the Fermi level of the tip. This creates a tunneling current from the occupied states of the tip towards the unoccupied states of the sample. However, the transmission factor, which depends on the both work functions, the distance between tip and sample and the energy of the electron, also affects the tunneling current [47].

A more complex, but commonly used description of the tunneling theory in STM is the Tersoff-Hamann model based on Bardeen's description of tunneling [50]. The time evolution, while the tip-substrate distance reduces, can be discussed with perturbation theory. However, due to adiabatic switching, the potential of the tip after the approach will remain constant. The whole state Ψ consists of a linear combination of eigenfunctions from before the perturbation and a set of wave functions after.

The key point in Bardeen's description of tunneling is that the two sets of wave functions can be approximated as to be orthogonal to each other. The essence of the Tersoff-Hamann model is to focus on the electronic states of the tip close to the Fermi level. Since the tunneling current is described by the convolution of the electronic states of the tip and sample, this simplifies the problem to result in an STM image depended to
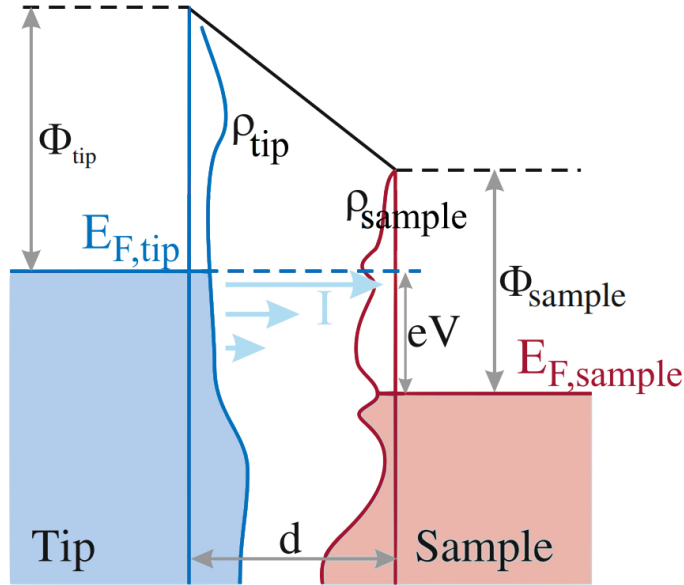
Figure 3.4: Sketch of the energetic levels of the tunneling junction between tip and sample during STM measurement. While a positive bias voltage is applied, the Fermi level E_{F} is shifted. The electron then flows from the occupied (coloured) to the unoccupied states. The density of states of the tip and sample are given as φ_{tip} and $\varphi_{\mathrm{sample}}$, respectively. Adapted from [45, 49].

the properties of the sample alone [50]. For a more detailed and advanced description, the reader is referred to literature [49–51].

The high vertical resolution of STM is due to the exponential dependence of the tunneling current on distance. The lateral resolution is largely due to the fact that the tunneling current predominantly flows between the last atom of the tip and the atom closest on the surface [47].

In practical use, the tip in STM moves across the sample to depict the structure of the surface. The tunneling current is typically kept constant during operation. This is achieved by regulating the tip-sample distance to modulate the overlap between the electronic states of the tip and sample. Since the local density of states of the sample greatly effects the tunneling current, not only geometric features but also information about the local density of states (LDOS) are incorporated in the obtained image.

All data presented in this work were analysed using the WSxM software [52].

3.3 STS

Scanning tunneling spectroscopy (STS) is an extended functionality of the STM to investigate the electronic structure of materials at the surface with high local resolution. Foremost, it is utilised to determine properties based on the LDOS, like bandgap measurements of semiconductors. For this specific experimental property, the applied bias voltage V is varied at one specific position in space where the tunneling current I is measured. This leads to $I(V)$ and is often referred as constant height STS. With this data, the derivative $\mathrm{d}I/\mathrm{d}V$ can be obtained. Since the probability of tunneling is directly influenced by the number of electronic states in the sample and the applied voltage can be seen as energy of the tunneling electrons, the derivative $\mathrm{d}I/\mathrm{d}V$ is proportional to the LDOS in regimes, where the tunneling current is predominantly dependent on the electronic states [47]. This method is especially useful to identify different regions and

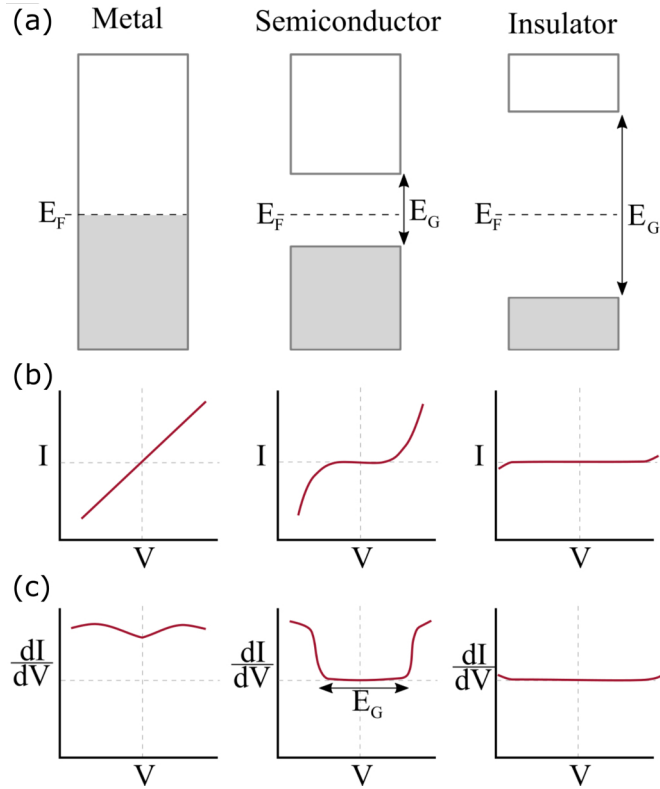gaining first knowledge about the electronic properties of the probed materials.

Figure 3.5: (a) Schematic drawing of the electronic structure of a metal, semiconductor and insulator with respect to Fermi energy E_F and bandgap E_G. (b) Expected electronic behaviour in terms of $I(V)$ measurements for each material class. (c) In order to measure the bandgap, the derivative is used. $\frac{\mathrm{d}I}{\mathrm{d}V}$ of the curves of (b) are shown. Adapted from [45, 53].

The general shape of the LDOS already gives information about the conductance of the probed materials, see fig. 3.5. Materials with metallic properties have a small variation in DOS across the energy landscape close to the Fermi energy E_F. This results in no band gap between conduction and valence band. In $I(V)$ measurements, this can be seen as a positive linear slope. Thus, in the derivative $\mathrm{d}I/\mathrm{d}V$ a nearly constant measurement will be observed. However, semiconductors and insulators do exhibit a band gap E_G of various size. Bandgaps of semiconductors are relatively small, whereas insulators have a gap larger than $E_\mathrm{G} > 3\,\mathrm{eV}$. This results for both material classes in no conductance around the Fermi level. With this, $I(V)$ and $\mathrm{d}I/\mathrm{d}V$ spectra are zero until the voltage is increased such that the measurements are outside of the band gap which results in a sudden onset of current due to a sudden increase in DOS. With this, bandgaps of semiconductors can be accurately determined.

In ideal conditions, the tip is purely a metal, such that the DOS of the conducting tip is featureless and does not contribute to the measurement. However, as a result of an approximation in the Tersoff-Hamann model, it can be assumed that only electron states near the Γ point of the surface Brillouin zone contribute to the tunneling current since the parallel momentum of the surface electronic state should be relatively small [51]. This makes this measurement technique in STM more sensitive to the Γ point.

In order to obtain the derivative $\mathrm{d}I/\mathrm{d}V$, the numerical derivation of $I(V)$ is possible but typically the lock-in amplifier technique is used. The advantages of this technique are, besides the direct measurement, the reduction in noise in the spectroscopy [54]. A small

sinusoidal modulation signal is added to the bias voltage $V_{\text{total}} = V_{\text{bias}} + V_{\text{ext}}\sin(\omega t)$, which in turn results in a modulation of the tunneling current. The modulation frequency ω is set to not interfere with STM measurement. The resulting tunneling current can be expressed by an expansion into a Taylor series. Inside the lock-in amplifier, this signal is compared to a reference signal V_{ref} in a phase-sensitive detector (PSD). The resulting signal is then filtered in a low-pass filter, such that a direct current output signal is obtained. Any other interfering signal will be filtered out, so that the output of the lock-in amplifier is nearly noiseless [54]. The setup of STM together with the lock-in amplifier is visualised in fig. 3.6.
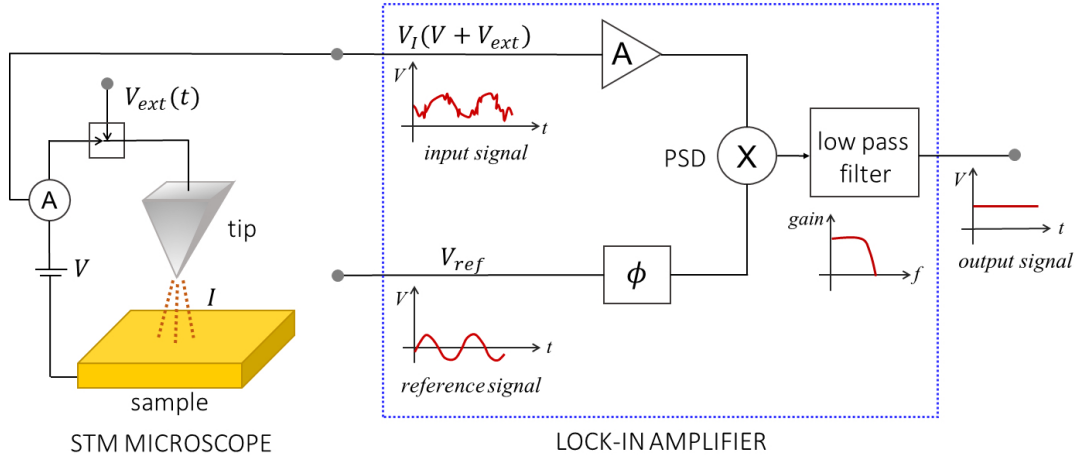

Figure 3.6: Schematic drawing of an STM in combination with a lock-in amplifier. The tunneling current is modulated by an external signal $V_{\text{ext}}(t)$. After multiplication by a reference signal V_{ref} through a phase-sensitive detector (PSD), the product is filtered by a low-pass filter. This results in a direct current output signal. Adapted from [55].

There are many more advanced surface properties, which can be obtained using different spectroscopy techniques. One of them is constant-current STS. Contrary to the constant-height mode, the current is fixed and only changes in the tunneling current will be detected in dI/dV. Since this mode is similar to the regular imaging, both can be performed in parallel. The spectroscopy images are referred to as dI/dV maps. The sample is probed at one specific bias voltage interval and therefore energy region. This interval is achieved by the external modulation voltage added to the bias voltage. The tip movement is slowed down significantly compared to regular imaging, such that the time for each measured pixel correlates to three time constants of the lock-in amplifier. This technique results in images based on electronic features in the specified energy interval, without any influence of topographical factors.

3.4 Setups

Two different UHV setups were involved in this study, a home-built CVD/PVD system for mainly chemical (CVD) and physical vapour deposition (PVD) and a variable temperature-STM (VT-STM) system. Both operate at a base pressure of 1×10^{-10} mbar to ensure a clean environment for surface-sensitive growth.

The main purpose of the CVD/PVD system is fast and convenient sample preparation [56]. The naming scheme is based on two deposition techniques which are possible at this machine. Generally, the system consists of two separate chambers, a fast entry lock (FEL) and a main chamber, both equipped with a turbo pump and connected via a manual gate valve, see fig. 3.7. The FEL is used for convenient sample exchange
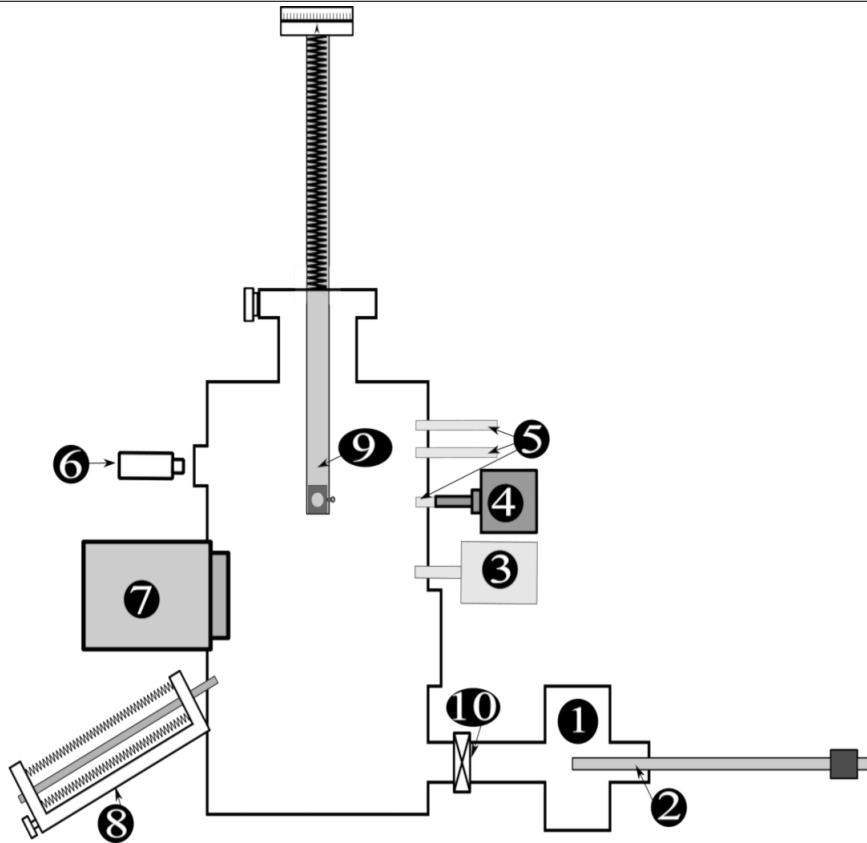
Figure 3.7: Schematic drawing of the CVD/PVD system. The side view shows the following components: (1) FEL, (2) transfer arm, (3) QMS, (4) sputter gun with argon gas inlet, (5) gas dosers, (6) pyrometer at a viewport, (7) LEED, (8) evaporator, (9) four-axis manipulator and (10) manual gate valve. Both chambers are equipped with turbopumps while only the main chamber has an additional ion-getter pump (not shown) [48].

without breaking the vacuum of the main chamber and therefore without introducing any contaminants. The main chamber is equipped with a sputter gun for sample cleaning, Oci 4-grid LEED optics for surface characterisation, gas inlets for cleaning and gr preparation, quadrupole mass spectrometer (QMS) for residual gas analysis, pyrometer for optical temperature measurement and a four-axis manipulator equipped with an electron beam heating stage and a quartz crystal microbalance (QMB). This system is mainly used for detailed characterisation of evaporation material and sample preparation. Through accurate growth techniques, the same preparation results could be converted to other systems.

STM measurements were conducted at a Scienta Omicron VT-STM system, see schematic drawing in fig. 3.8. It consists of three separate UHV chambers: FEL, preparation and deposition chamber. The deposition chamber is not involved in any sample preparation, or measurement in this study. Similar to the CVD/PVD system, the preparation chamber contains everything mentioned above, except a QMB device, but an STM. Due to the VT option, the sample temperature can be altered in a range from 120 K up to 450 K. If not mentioned otherwise, the STM was operated at room temperature.
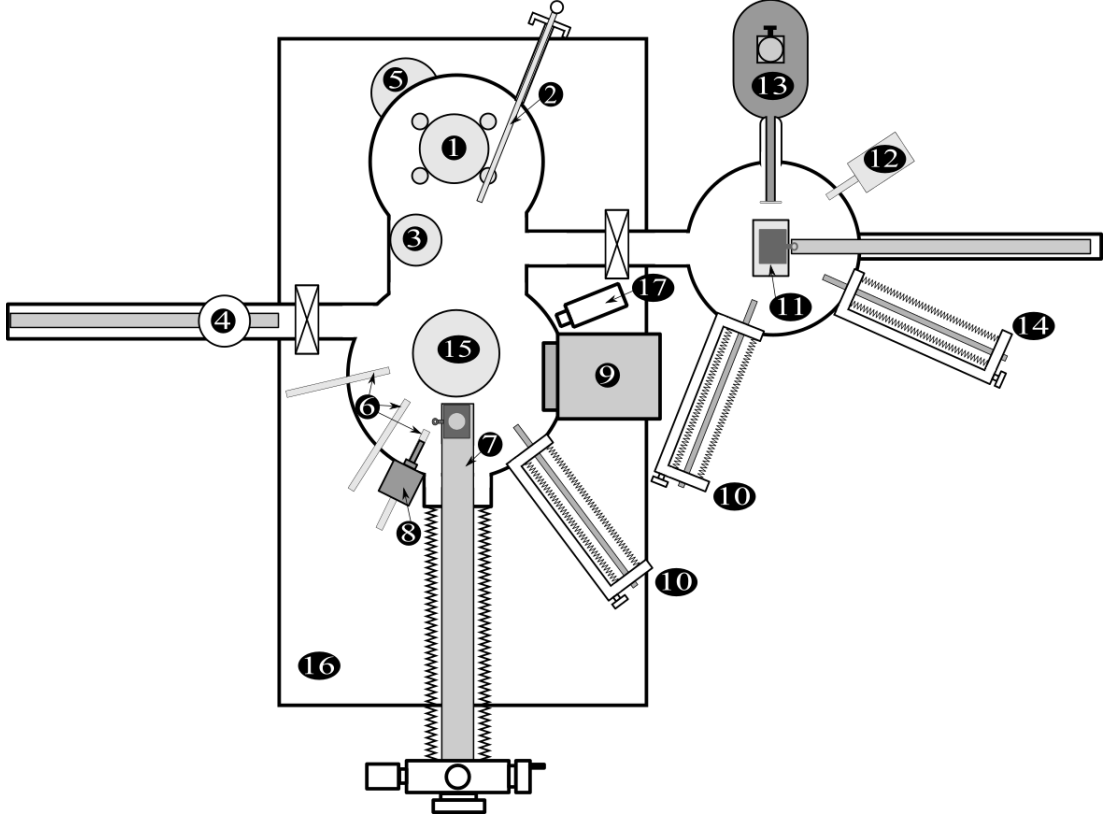
Figure 3.8: Schematic drawing of the VT-STM system. The top view shows the following components: (1) STM, (2) wobblestick, (3) carousel for sample storage, (4) FEL with transfer arm, (5) cooling reservoir, (6) gas dosers, (7) manipulator with e-beam heater and sample, (8) ion gun, (9) LEED/AES, (10, 13, 14) different evaporators, (11) heater stage, (12) QMS, (15) titanium sublimation pump and cooling trap, (16) table, (17) pyrometer. Both chambers are pumped with a turbo-pump and an ion getter pump (not shown) [45].

3.4.1 Pyrometer

In order to accurately determine sample temperatures in any used system, a pyrometer is used for contactless temperature measurement. It enables this option by measuring black body radiation. Any black body is an idealised object, that emits all radiation depending on its temperature. This can in turn be described for the spectral radiance B by Planck's law

$$B\left(\nu, T\right) = \frac{2h\nu^3}{c^2} \frac{1}{e^{\frac{h\nu}{k_{\mathrm{B}}T}} - 1},$$ (3.4.1)

where h is Planck's constant, ν the frequency, c the speed of light, k_{B} the Boltzmann constant and T the temperature of the radiating object. In practice, spectral intensity $I = \mathrm{d}P/\mathrm{d}\lambda$ or total power P are more accessible quantities and the latter can also be described by the Stefan-Boltzmann law

$$P = k \cdot \epsilon \cdot A \cdot T^4,$$ (3.4.2)

with k as a prefactor, ϵ as emissivity, and A as the surface area. Due to Wien's displacement law, the maximum of the intensity shifts to lower frequencies with higher temperatures. Since there are no perfect black bodies, the emissivity factor of the used metallic substrates is set by literature values. In experiment, a Lumasense IGA140 with

a detectable spectral range up to 1.8 μm is used [57]. Such a infrared radiation sensor is capable to determine temperatures of up to ≈ 1500 K. Note that since the total power is proportional to the forth power of the temperatures, there is a higher sensitivity at increased values. This results in limitations in lower temperatures or lower emissivity factors. Low temperatures (< 530 K) are estimated by a linear regression to the applied filament current. Measurements for materials with low emissivity factors, as for example in the case of the gold surfaces, result in large differences between measured and actual temperatures. This is overcome by a calibration of the pyrometer to a sample which is connected by a thermocouple. The calibration data can be seen in [58].

Similarly to [45], the error of pyrometer measurements $\sigma\left(T_{\mathrm{pyro}}\right)$ can be summed up due to three effects: the internal measurement uncertainty [59], the sinusoidal angular dependency of the optical measurement, and temperature dependent emissivity errors. This can be expressed as

$$\sigma\left(T_{\mathrm{pyro}}\right) = \sqrt{(3 \cdot 10^{-3} \cdot T + 276\,\mathrm{K})^2 + (1.122 \cdot 10^{-5} \cdot \frac{1}{\mathrm{K}} \cdot T^2 + 6.91 \cdot 10^{-3} \cdot T + 277\,\mathrm{K})^2}.$$
(3.4.3)

3.4.2 Quartz microbalance

Evaporation rates are an important parameter of preparations. Generally, there are two possibilities for rate determination. For sub-monolayer structures, STM is the most accurate way. The coverage seen in STM images is the outcome of evaporation rate times duration. A quicker way without intense STM study, is the use of a quartz crystal microbalance (QMB). In experiments at the CVD/PVD system, an Inficon QMB is used to detect small changes in mass over time. A piezoelectric crystal, like quartz, transforms mechanical stress into electric potential difference and vice versa. A voltage is applied to the crystal, in order to induce oscillations with the frequency $f = \frac{N}{d_{\mathrm{q}}}$, with $N = 1.67 \cdot 10^6$ Hz · mm and d_{q} the thickness of the quartz crystal. As the deposited material increases the thickness of the quartz crystal and subsequently also alters the mass by Δm, the resulting frequency changes. This shift Δf can be expressed by

$$\Delta f \propto \frac{f_0 \Delta m}{\rho_{\mathrm{q}} N A},$$
(3.4.4)

with ρ_{q} as the density of the quartz crystal, and A as the deposited area [60]. By measuring the frequency shift, the resulting thickness can be calculated by a useful calibration and the correct density of the deposited material. The rate is therefore the thickness in terms of ML per evaporation duration.

This method of rate determination is quite useful and typically in agreement with rate determination with STM. Differences can occur due to the assumption of bulk density of the deposited material, as well as a similar interaction between deposited material and quartz surface compared to the later used substrate.

3.4.3 Quadrupole mass spectrometer

For residual gas analysis, a quadrupole mass spectrometer (QMS) by Pfeiffer QM200 in CVD/PVD or mks e-Vision 2 in VT-STM is used. Molecules and atoms are ionised due to a radiative filament. The quadrupole itself consists of two sets of dipoles (DC current) where additionally an alternating electric field is superimposed. This arrangement allows, with careful manipulation of the AC frequency, to filter the particles by the ratio of mass and charge m/q. The resulting current from the ionised particles is then detected for each ratio m/q. The range on both devices enable measurements up to

200 amu.

Due to the missing information of q, the ratio m/q is typically presented as mass with $q = 1\,e$. For definitive characterisation of gases and evaporated materials, isotopic compositions and ionisation tendency are necessary. Comparison of measured QMS spectra to isotope abundance or already known spectra [61], result in definitive element determination.

3.5 Sample preparation methods

In the following section, standardised procedures for creating defined clean surfaces are described, which are used before each new preparation. Metallic single crystals, manufactured from MaTeck, with highly accurate orientation ($< 0.1°$) and very low roughness ($< 10\,$nm), are used.

A clean crystal surface is achieved by Ar$^+$ bombardment ($p_{\mathrm{Ar}} = 1{\cdot}10^{-5}\,$mbar, $E = 1\,$keV, $I_{\mathrm{emission}} = 10\,$mA, $t = 30\,$min) at room temperatures with subsequent annealing up to 1500 K in order to remove residual Ar atoms and flatten the surface. This is used for all platinum-group metals (e.g. Ir and Pt), for gold surfaces the bombardment process is performed at elevated temperatures with annealing only up to 900 K. Cleanliness is always subsequently checked by LEED.
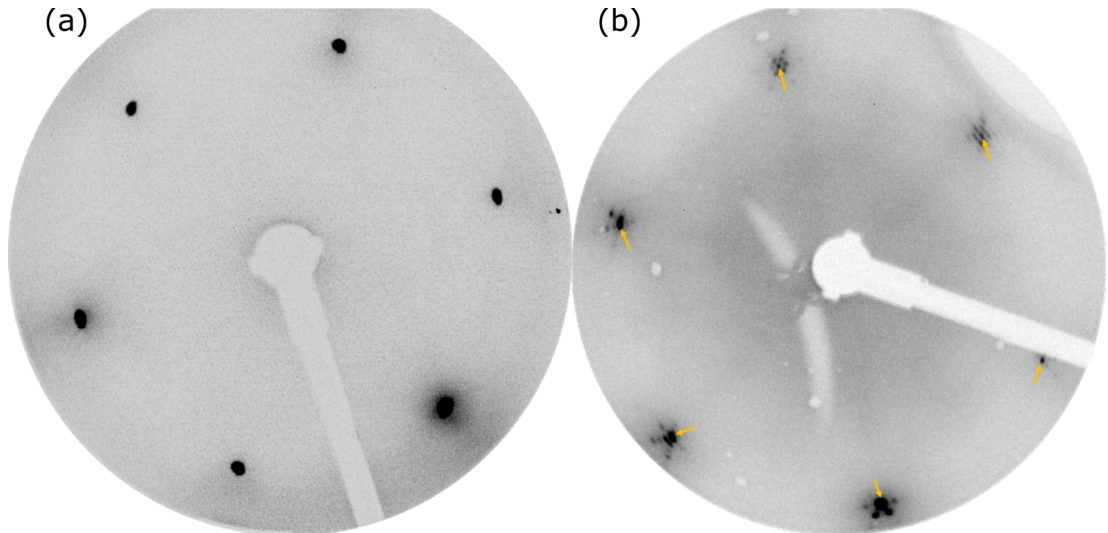

Figure 3.9: LEED measurements at 70 eV of clean surfaces for a (a) Ir(111) and (b) Au(111) crystal after the cleaning process described in the text. The Au spots are highlighted in (b), adapted from [58].

Fig. 3.9 shows exemplary LEED images for clean Ir(111) and Au(111) surfaces. Due to the specific cut resulting in a hexagonal lattice of the substrate atoms, six reflexes can be seen. Additionally, in the case of Au(111) spots stemming from the herringbone reconstruction can be seen. Therefore the main reflexes from the Au(111) are highlighted. Graphene preparation on platinum group metals follows the recipe by van Gastel *et al.* [62], in order to provide a full layer with an unrotated, homogeneous single phase. This recipe uses a two-step process. A temperature-programmed growth with exposure to 120 L of ethylene at RT, and subsequent thermal decomposition at a sample temperature of 1400 K. This step forms graphene nuclei which are well-orientated to the underlying substrate. Then as a second step, chemical vapour deposition is used to expand already existing nuclei to a complete layer by exposure of 120L of ethylene at an elevated sample temperature of 1250 K. Cleanliness and orientation of gr is verified by well-defined

LEED patterns. Fig. 3.1 (b) demonstrates such a LEED measurement for gr/Ir(111). The first-order reflexes can be summarised in six groups, each consisting of a Ir(111) (highlighted in red for one of the reflex groups) and a graphene spot (in blue). The reflex further to the center is corresponding to Ir(111) due to the larger lattice constant ($a_{\mathrm{Ir(111)}} = 2.72\,\text{Å}$ [63], $a_{\mathrm{gr}} = 2.46\,\text{Å}$ [62].) The graphene spot is also surrounded by satellite reflexes due to the moiré superstructure, stemming from the overlap of the two hexagonal lattices of Ir and gr.
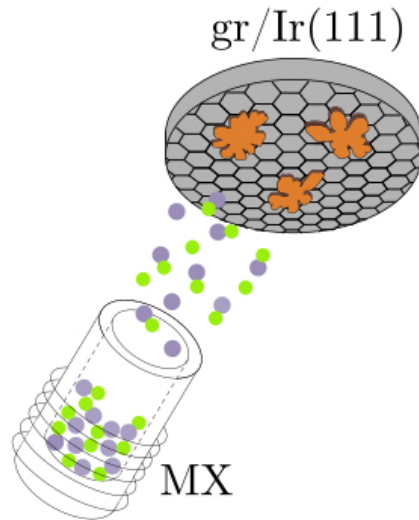

Figure 3.10: Schematic drawing of the evaporation process of MX from an effusion cell with heating spiral on a gr/Ir(111) surface.

Monochalcogenides were evaporated from powders in an effusion cell (Dr. Erberl standard effusion cell or Kentax 3-pocket evaporator). The cells were cleaned with ethanol and filled with $\approx 2\,\text{g}$ of powder. Specifications for each material are given at the beginning of each chapter. A schematic drawing of such an evaporator can be seen in fig. 3.10. The cell is heated by radiative heating of a tungsten wire. Temperatures are determined by inbuilt thermocouples. For temperature stability, the evaporator was held at the specified temperature for $20\,\text{min}$. A mechanical shutter (not shown in drawing) is used to control the evaporation duration. This results in three experimental parameter which can be set by using such evaporators: temperature, distance and evaporation duration.

In order to achieve transparent and repeatable results between each evaporator, evaporation rates and duration are used and given as preparation parameter. These rates were determined either by STM or QMB. This is especially necessary for evaporators with different orifices. Evaporation rates can be varied either by temperature or distance. In order to calibrate necessary distances for two effusion cells with differently sized orifices to achieve the same evaporation rate, the mathematical considerations in the appendix of [64] were used. Distances given in the text later generally refer to the Kentax evaporator due to the more frequent use case.

Chapter 4

Growth study of SnSe on gr/Ir(111)

Important properties of materials are directly linked to crystal structure and island shape. This relationship is further elucidated by examining the underlying geometrical characteristics of a specific two-dimensional ferroelectric in greater detail. Single layer of tin selenide (SnSe) form puckered sheets with an orthorhombic structure, see fig. 4.1. A single layer (often referred to as monolayer) is defined by two atomic rows, which differs from the orthorhombic unit cell with four atomic rows in c-direction. This structure is very similar to the one of phosphorene with the difference in the off-plane tilt of the Sn-Se bonds.
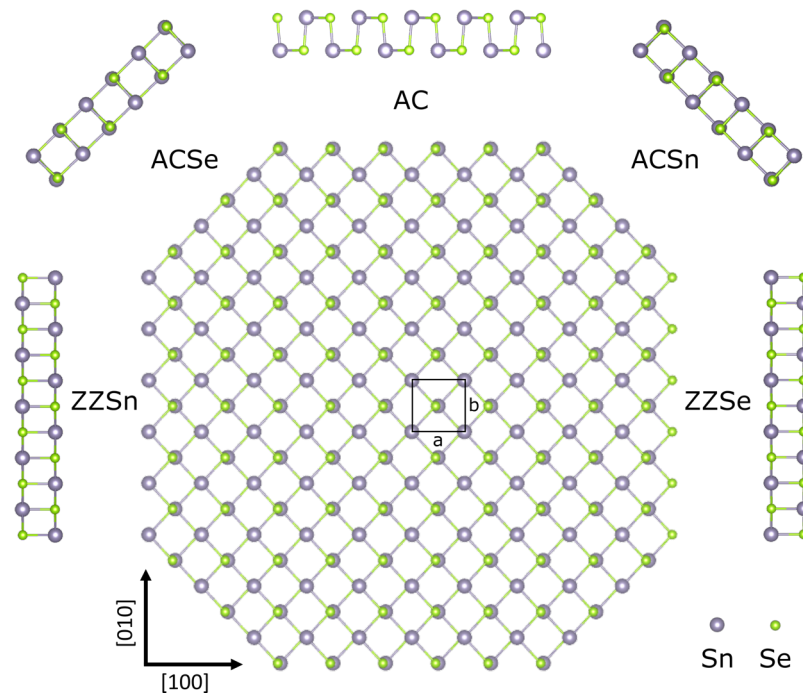

Figure 4.1: Crystal structure of freestanding monolayer SnSe from DFT calculation. Purple balls represent Sn, green Se atoms. The unit cell with lattice constants a and b is indicated as well as the corresponding lattice directions [100] and [010]. A hypothetical island with all possible dense-packed edge types assuming 2D-bulk termination is depicted. Edges are labelled according to structure (AC for armchair, ZZ for zigzag) and termination (Sn or Se), see text. Each different edge is also represented with a side view next to the edge.

The step edges are defined perpendicular to the crystal directions and for now are displayed as 2D-bulk-terminated edges. Since the crystal structure only has a mirror symmetry with respect to [100], this results in five different types of closed-packed edges. The nomenclature is similarly used in [65], where Wang *et al.* discuss the need to consider all zigzag (along primitive cell vectors) and armchair (along diagonal direction) edges in order to describe edge energies in any arbitrary direction via an energy decomposition ansatz.

The edges normal to [010] and [0$\bar{1}$0] are equivalent due to symmetry and form an armchair-like structure (labelled with AC). This edge is charge neutral since both species of atoms have the same distance from the step edge and in an equilibrium situation also the same partial charge. With slight variation, the edges normal to [110] and [$\bar{1}$10] are also of armchair type, but the Se atoms are closer to the step edge, which are therefore named ACSe and making this edge slightly negatively charged. The counterpart ACSn, which is slightly positive, can be found normal to [1$\bar{1}$0] and [$\bar{1}$10]. The final two step edges are normal to [100], which are completely terminated by Se in a zigzag arrangement (ZZSe), and [$\bar{1}$00], which is also in a zigzag arrangement but with Sn termination (ZZSn). Both of these step edges are strongly charged. Since the configuration as introduced above would leave individual positive point charges (Sn) on one side and negative point charges (Se) on the other one, this is only possible with the absence of pure zigzag edges.

This chapter starts by describing the growth of SnSe islands on a graphene on Ir(111) surface (sec. 4.1.). In order to determine the equilibrium shape, a compaction process with detailed focus on the edges is studied in sec. 4.2. After that, the effect of this shape and edge reconstruction on an electronic level are discussed (sec 4.3.).

The theoretical results based on density functional theory (DFT) were provided by Mahdi Ghorbani-Asl and Arkady Krasheninnikov [66]. The calculations were performed using the Vienna Ab initio Simulation Package (VASP) [67, 68]. The exchange-correlation functional was employed in the generalised gradient approximation of Perdew-Burke-Ernzerhof (GGA-PBE) [69]. For plane wave expansion an energy cut-off of 600 eV and for supercell calculations 400 eV were used. The simulation of the edge models were constructed with ribbons in various sizes ranging from 10×2 to 44×2 supercells for [100]- and [$\bar{1}$00]-edges, 10×2 to 45×2 supercells for [010]- and [0$\bar{1}$0]-edges, and ribbons with sizes of 7×2 to 32×2 supercells for [110]- and [$\bar{1}$10]-edges. The Brillouin zone of the primitive cells and supercells were sampled using $(12 \times 12 \times 1)$ and $(4 \times 1 \times 1)$ Monkhorst-Pack k-point, respectively. All structures are fully optimised until the maximum force on each atom is less than 0.01 eV/Å. In order to check for consistency, the optimised bulk structure was calculated. The resulting lattice constants are in agreement within 2 % of experimental results [70].

4.1   Nucleation of SnSe islands

Tin selenide islands can be grown by epitaxial methods on different substrates. In order to investigate the characteristics of a nearly freestanding monolayer, a rather weak interacting surface is selected. For this purpose graphene on an Ir(111) surface is used, which does not only fulfill this requirement but also can be grown as a complete and defect-free layer. Due to a rather low melting point, SnSe (5N powder, Alfa Aesar) can be evaporated from an effusion cell at a temperature of 723 K. This temperature was chosen since it resulted in a stable rate and maximum dimer content in a residual gas analysis (measured with QMS [71], not shown here) in the UHV chamber. Due to the ionic bonds of MXs, single atoms could also arise from evaporation. This cannot be distinguished from dimer splitting due to ionisation in QMS, resulting in

using this approach. Therefore the evaporation rate is varied by changing the distance between source and sample (in the range of 8 to 12 cm). Due to the fixed evaporation temperature, any preparation is described by the three parameters (rate, evaporation time, sample temperature), while STM images also have the addendum of (image size, bias voltage V, tunneling current I), which is given for any experimental figure. Due to our previous observation that SnSe is not stable when exposed to ambient conditions [71], the prepared samples needed to be investigated in STM without breaking the vacuum. Other reports state that SnSe nanostructures oxidise in atmospheric environment [72], which is in agreement with this finding.
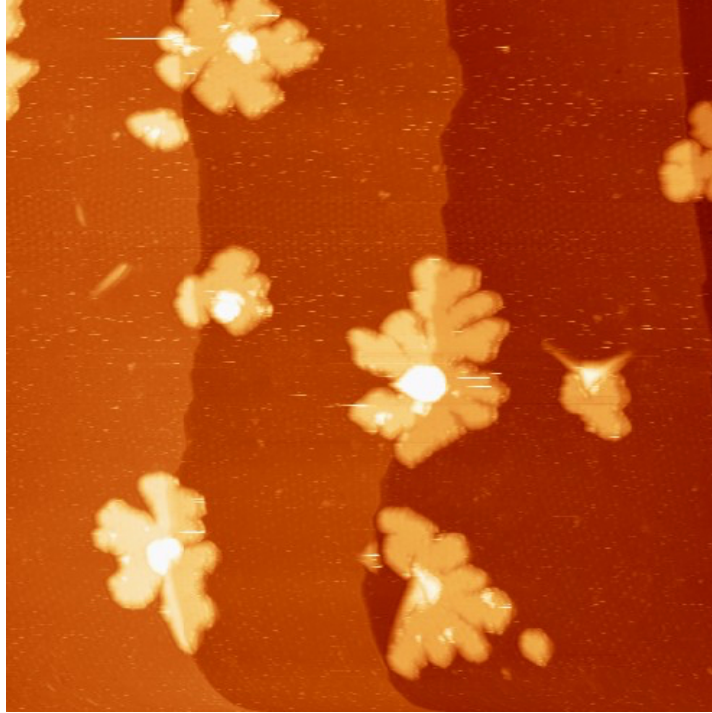

Figure 4.2: Large scale overview STM image of fractal-dendritic SnSe islands on gr/Ir(111); (5.2×10^{-3} ML/s, 30 s, RT); ($1\,750$ Å $\times$ $1\,750$ Å, 3 V, 10 pA).

Evaporation of SnSe for 30 s with a rate of 5.2×10^{-3} ML/s on gr/Ir(111) at RT leads to large, widely separated fractal-dendritic monolayer islands, see STM image in fig. 4.2. Most of the islands are centred at pre-existing step edges or defects which can be seen by the bright contrast. Defects can be clearly distinguished from bilayer formation (discussed in chapter 5) by an order of magnitude in height difference. Imaging was demanding and could only be performed at low currents, in order to prevent manipulation of the islands during scanning, and high voltages due to the semiconducting nature of the islands. The shown preparation resulted in a coverage of $\Theta_0 = (0.16 \pm 0.03)$ ML, measured over multiple large-scale overview images, whereas the resulting experimental single layer of SnSe corresponds to the monolayer structure as shown in fig. 4.1. The island density (islands per surface area) is determined by counting in many individual images and is for this case $n_0 = (1.8 \pm 0.3) \times 10^{-8}$ Å^{-2}. Such a low island density indicates that the precursors for growth are rather mobile on gr/Ir(111) at RT and / or that nucleation is a low-probability process. An indicator for hampered step-edge diffusion is the fractal-dendritic shape of the islands. The very easy manipulation with the STM tip also suggests a rather weak interaction between MX and substrate. The apparent height of the monolayer SnSe islands is $h = 5.50 \pm 0.06$ Å (calibrated by Ir step heights), compare fig. 4.3 (c), which did not significantly depend on tunneling

parameters.

In order to characterise the shape of an island, the ratio between its perimeter P and area A is decisive. As the physical quantity perimeter is difficult to determine and strongly depends on the resolution of the underlying STM image, the parameter A_{edge} is introduced which is proportional to P but experimentally more robust.

In order to motivate this introduction and demonstrate the problem, a closer look at a Koch snowflake can help [73], known for having a finite area although an infinite perimeter. This is not true for the real world as the atomic scale limits the smallest unit length. Nevertheless, this example demonstrates the increasing ratio P/A of perimeter P and area A with increasing resolution, here realised by an increasing number of iterations. Iteration one is an equilateral triangle with side lengths L. With each subsequent iteration, another equilateral triangle with $1/3$ of the original side length is added in the middle of each side of the edges.

n	Visualization	Perimeter P	Area A	P/A
1		$3L$	$\frac{\sqrt{3}}{4}L^2$	$\frac{4\cdot\sqrt{3}}{L} \approx \frac{6.9}{L}$
2		$3L + 3\cdot\frac{L}{3}$	$\frac{\sqrt{3}}{4}L^2 \cdot (1+\frac{1}{3})$	$\frac{12}{\sqrt{3}\cdot L} \approx \frac{6.9}{L}$
3		$4L + 12\cdot\frac{L}{9}$	$\frac{\sqrt{3}}{4}L^2 \cdot \left(1+\frac{1}{3}+\frac{12}{81}\right)$	$\approx \frac{8.3}{L}$
4		$4L + 12\cdot\frac{L}{9} + 28\cdot\frac{L}{27}$	$\frac{\sqrt{3}}{4}L^2 \cdot \left(1+\frac{1}{3}+\frac{12}{81}+\frac{28}{729}\right)$	$\approx \frac{9.7}{L}$

Table 4.1: Perimeter P, area A, and ratio P/A in dependence of iteration ($n \leq 4$)) with visualization for a Koch snowflake to motivate the use of the parameter A_{edge}/A.

Table 4.1 shows the calculations of perimeter P, area A, and ratio P/A for increasing iterations. The value $n = 4$ is a reasonable comparison to experimental conditions since a starting side length of $L = 100\,\text{Å}$ results in a smallest unit of $3.7\,\text{Å}$. Until then, the ratio P/A strongly alters with each iteration. From this, it is directly obvious that the ratio of perimeter and area is strongly dependent on resolution and therefore experimentally not ideal.

The parameter A_{edge} is defined as the area in the height interval $[h - \Delta h_1, h - \Delta h_2)$, where h is the average height of the island with $\Delta h_1 = 0.7\,\text{Å}$ and $\Delta h_2 = 0.2\,\text{Å}$. This is schematically visualised in fig. 4.3 for one exemplified island (subfigure (a)), where the parameter A_{edge} is in turn the corresponding area in the height interval $[4.8\,\text{Å}, 5.3\,\text{Å})$ with the island height of $h = 5.5\,\text{Å}$. This area is highlighted in fig. 4.3 (b) and (c) in green colour for the area in the topography image and the height interval in the line profile across the island, respectively. The total area A represents the total island area and is defined by a lower threshold in height h_0, which is chosen as low as possible but higher than any areas of the substrate including the gr/Ir moiré maxima. In this exemplary case, this threshold is set to $h_0 = 0.25\,\text{Å}$ above the substrate background level. This is indicated by the blue line in fig. 4.3 (c) and all pixels below h_0 are coloured in blue in subfigure (b). For this specific island, the phenomenological shape parameter results to $A_{\text{edge}}/A = 0.130$.

In this form, A_{edge}/A is by definition proportional to the perimeter normalised by island area P/A. Experimentally, the advantage is mostly the invariance to imaging errors and resolution differences because of calculating affecting regions out by the unit-less
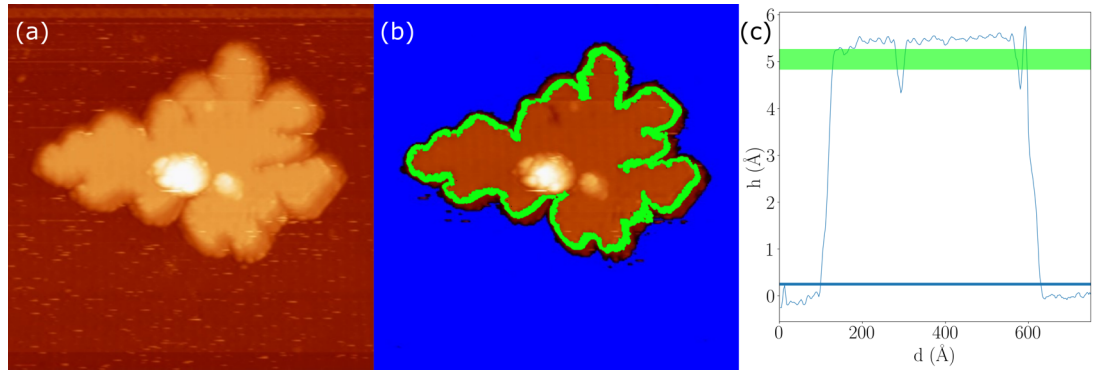
Figure 4.3: Determination of shape parameter A_{edge}/A. (a) STM image of SnSe/-gr/Ir(111), (750 Å×750 Å, 3 V, 10 pA), grown at $(5.2 \times 10^{-3}$ ML/s, 60 s, RT) and annealed at 503 K for 1200 s. (b) Same STM image as in a), but coloured in orange, green, and blue are 2D-bulk, edge area, and gr, respectively. (c) Height profile of the island. The height interval corresponding to A_{edge} and the background level are highlighted in green and blue, respectively.

fraction. For accuracy, this method was consistently used for multiple islands in each series and averaged.

For fractal-dendritic islands grown at RT, a value of $A_{\text{edge}}/A = 0.121 \pm 0.004$ is derived. These islands can also be characterised by their average branch thickness L_{b}, which is for the case at RT $L_{\text{b}} = 100 \pm 30$ Å. Analogous to the arguments from Prieto *et al.* that an island will result in a fractal dendritic shape if the time τ_e, required for an adatom to find the energetically favourable sites, is larger than the average time τ_i between two atoms add to the same island [74]. With that knowledge, the edge diffusion energy can be estimated for these islands. The average adatom arrival time can be written as

$$\tau_i = \frac{n}{R}, \tag{4.1.1}$$

with rate $R = 5.2 \times 10^{-3}$ ML/s and island density $n = 1.8 \times 10^{-8}$ Å^{-2}. The adatom scans the island in a random walk, so

$$\tau_e \approx \frac{L^2}{h_e}, \tag{4.1.2}$$

with the hopping rate h_e along the island edge. When both times become comparable, a compact starting island grows to a less compact shape and forms dendritic arms. The length L can then be expressed by the average branch thickness L_b [75], which results in:

$$L_b = 1.7 \cdot \left(\frac{h_e \cdot n}{R} \right). \tag{4.1.3}$$

From surface diffusion kinetics, the hopping rate can be expressed as energy and give us an expression for the edge diffusion barrier energy:

$$E_{\text{diff}} = -kT \cdot \ln \left(\frac{L_b^2 \cdot R}{n \cdot \nu_0} \right) = 308 \, \text{meV}, \tag{4.1.4}$$

where the attempt frequency is estimated as $\nu_0 = 10^{12} \, \text{s}^{-1}$. This value is comparable to similar fractal-dendritic growth processes, as for example in Co on a Cu(111) surface [74], where the shape is kinetically driven.

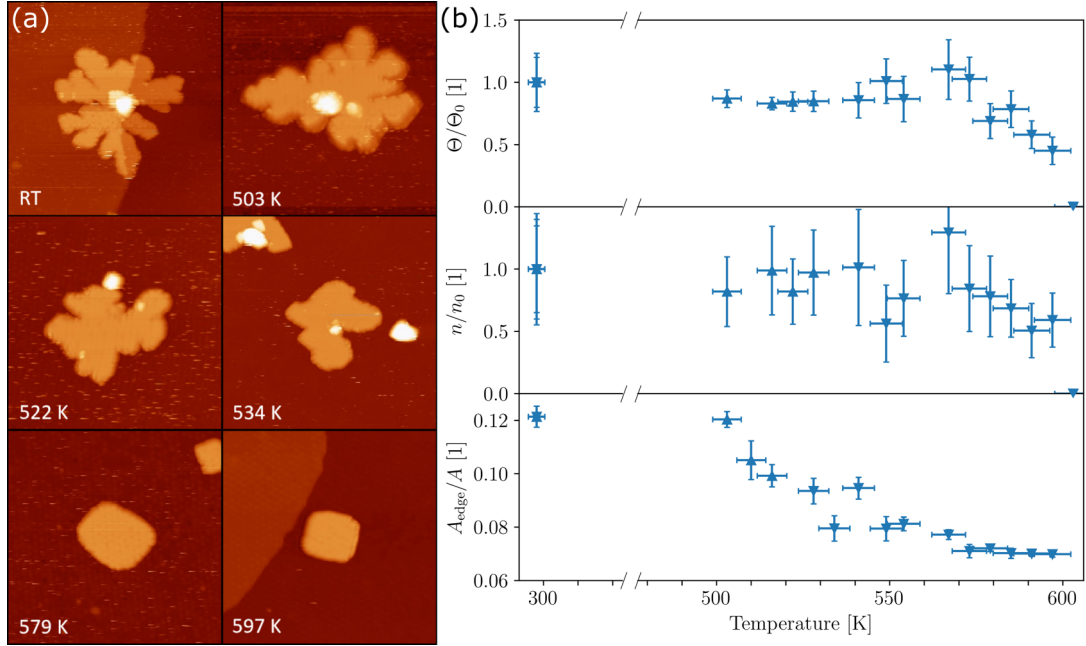The morphology of SnSe island changes through annealing, see fig. 4.4. Selected

31

Figure 4.4: Annealing sequence. (a) STM images of SnSe/gr/Ir(111) (750 Å × 750 Å, $1 - 3\,V$, $5 - 10\,pA$) annealed after growth ($5.2 \times 10^{-3}\,ML/s$, $10 - 30\,s$, RT) at the indicated temperature for $1200\,s$. An evolution from fractal-dendritic to compact islands can be seen. (b) Normalised coverage Θ/Θ_0 (top), normalised island density n/n_0 (middle), and shape parameter A_{edge}/A (bottom) in dependence of annealing temperature. Normalization: coverage ($\Theta_{0,\blacktriangle} = 0.16\,ML$, $\Theta_{0,\blacktriangledown} = 0.08\,ML$) and island density ($n_{0,\blacktriangle} = 1.8 \times 10^{-8}\,\text{Å}^{-2}$, $n_{0,\blacktriangledown} = 1.1 \times 10^{-8}\,\text{Å}^{-2}$).

heating steps, where the specific temperature is maintained for $1200\,s$, are represented by STM images of one typical island, given in subfigure (a). An extended data set with overview images is shown in fig. 4.5. In total, 20-40 islands were investigated for each annealing step. The morphology of the sample is characterised by three major parameters: coverage Θ, island density n and shape parameter A_{edge}/A, shown in dependence of temperature in subfigure (b). For Θ and n, the standard deviation between different images is represented by the error bars, while for A_{edge}/A the standard deviation between different islands is used. The error in temperature is due to the optical measurement technique via a pyrometer, explained in sec. 3.4.1. The initial coverage Θ_0 is varied between 0.08 and $0.16\,ML$ where no different behaviour in the morphology parameters could be observed. For that reason, different series are normalised by their initial values in Θ and n, which are indicated by different symbols (up- and downward facing triangles), and presented in the same graph. The same symbols are also used in fig. 4.5.

Coverage and island density do not change significantly in the temperature range from 298 to $567\,K$. This characteristic indicates that atoms do not detach from step edges, as this would lead to ripening via an adatom gas. Ostwald ripening is a process where smaller material accumulation decreases in size due to a comparatively lower vapour pressure, while all material is in a closed environment, so that larger clusters grow [18]. This could be identified by a decrease in island density. It also means that there is no irreversible desorption of material from the substrate in this temperature range, which would lead to a reduced coverage. Coverage and island density start to decrease at $574\,K$ until $603\,K$, when the islands disappear completely. Similar behaviour can be observed during the evaporation of SnSe powder, which also starts at around $600\,K$. Over the
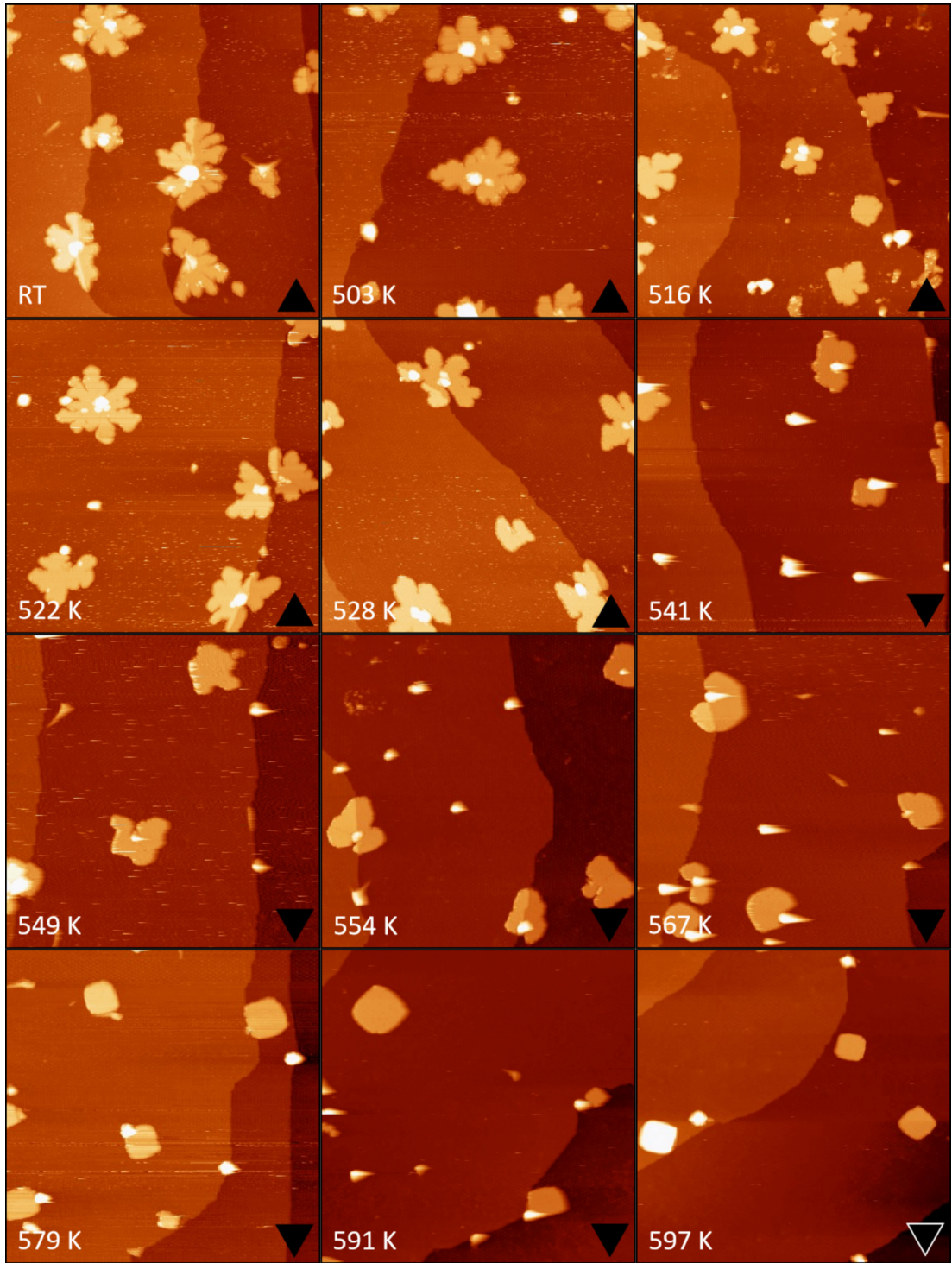
Figure 4.5: Overview images of the annealing sequence. STM images of SnSe/gr/Ir(111) ($2\,000\,\text{Å} \times 2\,000\,\text{Å}$, $1-3\,\text{V}$, $5-10\,\text{pA}$) annealed after growth ($5.2 \times 10^{-3}\,\text{ML/s}$, $10-30\,\text{s}$, RT) at the indicated temperature for $1200\,\text{s}$. The transition from fractal dendritic to compact islands can be seen. Different starting coverages Θ_0 and island densities n_0 are indicated by triangles in the bottom right corner of each image: $\Theta_{0,\blacktriangle} = 0.16\,\text{ML}$, $\Theta_{0,\blacktriangledown} = 0.08\,\text{ML}$ and $n_{0,\blacktriangle} = 1.8 \times 10^{-8}\,\text{Å}^{-2}$, $n_{0,\blacktriangledown} = 1.1 \times 10^{-8}\,\text{Å}^{-2}$.

whole temperature range, the average island size $\bar{A} = \Theta/n$ does not change. This excludes island migration and coalescence, which is known as Smoluchowski ripening. Most likely, the islands disappear one after the other, which could be due to a key process in the dissolution process of an island with a high activation barrier.

Although the islands do not interact among themselves, there is a significant reshaping process before the desorption starts. The ratio of A_{edge}/A (proportional to perimeter over area) starts to drop at 511 K. This compactification can be attributed to the onset of step edge diffusion. Since $E_{\text{diff}} >> k_{\text{B}}T$, Fickian diffusion around the edge can be assumed [18]. Any exchange process through an adatom gas as the underlying mechanism can be excluded because of the absence of ripening. The shape factor reaches a nearly constant value at 574 K, which indicates that the compactification is completed. This is also long before large changes in coverage or island density take place. Since the shape does not change with further annealing, it can be postulated that the islands already obtained their equilibrium shape. The shape resembles a rhombus with rounded corners. The islands investigated in reference [9] obtained by an analogical preparation show a similar shape. As no ripening process is involved in reaching the equilibrium shape, it can be concluded that at around 574 K each island is in local thermal equilibrium with itself.

It is plausible that each atom or dimer that detaches, directly desorbs from the substrate, which would cause ripening processes to be prohibited during annealing. This is supported by a stronger bond strength within the layer compared to the underlying material and could be a general mechanism for this class of materials on weakly interacting substrates like gr/Ir(111).

4.2 Equilibrium shape and edge reconstruction

In order to characterise the structural and electronic properties of SnSe islands, which are important to obtain a deeper understanding of the ferroelectric behaviour of the material, a high coverage of large, well-separated islands with defined shape and orientation is needed. Increasing the initial coverage results in high island density and also nucleation in the second layer, therefore a two-step process is introduced. First, small rectangular islands as described above are formed, which are then expanded by a second deposition step at an elevated sample temperature.

Fig. 4.6 (a) represents an overview image of SnSe on gr/Ir(111). The STM image displays several islands together with different kinds of defects on the substrate. There can be seen pre-existing substrate steps, graphene wrinkles which expand in any of the $\langle 11\bar{2}0 \rangle$-direction due to a threefold symmetry of the graphene on the iridium substrate [76], and areas with diffuse appearance that can be attributed to intercalation [77–79]. Regions with intercalation could only be observed when the deposition took place at elevated temperatures. The inset of this figure shows the LEED image corresponding to the STM image and depicted in the same orientation. LEED measurements result in six first-order Ir(111) spots, surrounded by reflexes from graphene and the moiré superstructure, and, closer to the center, 24 first-order spots contributed by SnSe. The SnSe spots can be sorted into three groups of 8 spots, which are marked in magenta, green, and blue. An orthorhombic lattice can be attributed to each group, as indicated by the blue lines. The [010]-direction of SnSe is in line with the zigzag $\langle 11\bar{2}0 \rangle$-direction of graphene. Lattice constants are determined as $a = (4.35 \pm 0.03)$ Å and $b = (4.26 \pm 0.02)$ Å, calculated according to [71]. Similar values were found for SnSe on graphitised 6H-SiC(0001) [9]. There are six equivalent $\langle 11\bar{2}0 \rangle$-directions that the SnSe can align with and there are six domains of SnSe/gr/Ir(111), since SnSe does not possess any rotational symmetry around the c-direction. Only three groups of spots can be observed as two of each are
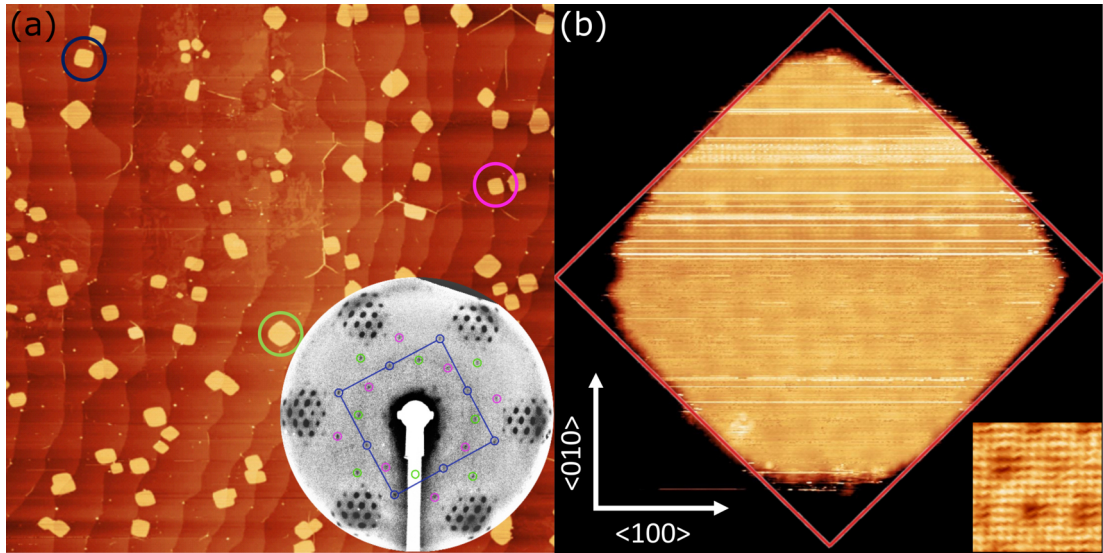
Figure 4.6: Orientation and equilibrium shape of SnSe/gr/Ir(111). (a) Overview STM image ($17\,500\,\text{Å} \times 17\,500\,\text{Å}$, $3\,\text{V}$, $20\,\text{pA}$) with LEED ($73\,\text{eV}$) inset (bottom left) showing the SnSe alignment to gr and marked in corresponding colours in the diffraction and exemplary in the topography image. The sample is grown in a two-step process at ($5.2 \times 10^{-3}\,\text{ML/s}$, $60\,\text{s}$, RT) and subsequently ($1.72 \times 10^{-3}\,\text{ML/s}$, $600\,\text{s}$, $570\,\text{K}$). (b) STM image showing an equilibrium SnSe island; ($5.2 \times 10^{-3}\,\text{ML/s}$, $10\,\text{s}$, RT) and subsequently annealed at $570\,\text{K}$; ($400\,\text{Å} \times 400\,\text{Å}$, $-0.1\,\text{V}$, $200\,\text{pA}$); with atomically resolved inset; ($5.2 \times 10^{-3}\,\text{ML/s}$, $30\,\text{s}$, RT) and subsequently ($1.72 \times 10^{-3}\,\text{ML/s}$, $300\,\text{s}$, $570\,\text{K}$); ($60\,\text{Å} \times 60\,\text{Å}$, $1\,\text{V}$, $200\,\text{pA}$). The topography is rotated to align the lattice with the image.

related to each other by inversion. Diffraction is insensitive to this according to Friedel's law, which states that a diffraction image is always centrosymmetric even though the crystal structure is not, resulting in $I_{hkl} = I_{\bar{h}\bar{k}\bar{l}}$.

Another indication that the SnSe islands are in thermal equilibrium is that all islands have very similar shapes. Fig. 4.6 (b) shows one example of a particularly well-formed island. Throughout the island a superstructure is visible. Lattice parameters of this superstructure are identical to the gr/Ir(111) moiré superstructure [80], which can be faintly seen in the background of figs. 4.2 (b), 4.3 (a), and 4.4. This phenomenon is also observed in related systems where the gr/Ir(111) moiré superstructure shines through the ultrathin overlayer.

The inset of fig. 4.6 (b) displays an atomically resolved image with protrusions that form a primitive lattice with similar parameters as determined by LEED within error bars. Therefore, there is a strong indication that only one of the four atoms in the unit cell is observed.

Since SnSe crystallises in a layered, strongly buckled structure, only atoms in the topmost layer will be visible in STM. The difference between the two atomic species in local density of states, which is a direct parameter of STM measurements, can explain why only every other atom of the upper ones is visible. Analogous to Frezza *et al.*, who compared non-contact atomic force microscopy (ncAFM) and STM measurements of SnSe/Au(111) [81], it is proposed that here also only the lattice of the upper Sn atoms can be observed, which is indicated by the unit cell in fig. 4.1.

The limited information (only observing one out of the four atoms in the unit cell) leads to the problem, that neither [100] and [$\bar{1}$00] nor [010] and [0$\bar{1}$0] can be distinguished in STM. Therefore, since there is no full geometric equivalency, from now on a slightly sloppy

notation will be used, with the definition: $\langle 100 \rangle = \{[100], [\bar{1}00]\}$, $\langle 010 \rangle = \{[010], [0\bar{1}0]\}$, and $\langle 110 \rangle = \{[110], [\bar{1}10], [1\bar{1}0], [\bar{1}\bar{1}0]\}$.

The islands are always limited by edges perpendicular to $\langle 110 \rangle$. This fact helps in determining the island orientation in a large-scale image as fig. 4.6 (a). All three orientations can be observed and are equally distributed across the sample. One island is highlighted in correspondence to the LEED image as an example.

Since experimentally the island edges are always perpendicular to $\langle 110 \rangle$, the equilibrium shape follows as a parallelogram. When taking the mirror symmetry in [100] of the lattice, this changes to a rhombus. This justifies the unconventional nomenclature, as even edges of different types in a rhombic shape have the same length. The rounding effect at the corners of the rhombus could be explained by either entropy causing sharp edges to be unfavoured or secondary facets in the equilibrium shape itself. Since zigzag edges are mostly non-existent in the equilibrium shape, any edge effect on polarisation is most likely small.

The equilibrium shape of 2D islands is defined as the shape that minimizes edge energy and can therefore also be extrapolated mathematically from the total step free energy $\delta(\theta)$. In a simple model $\delta(\theta)$ can be calculated from the least number of broken bonds for each direction in the lattice per unit length.

Therefore, the total step free energy $\delta(\theta)$ can be expressed by

$$\delta(\theta) = E_{\mathrm{B}} \cdot \frac{N_{\mathrm{bb}}}{2L}, \tag{4.2.1}$$

whereas E_{B} is the energy needed to break a single bond, N_{bb} is the number of broken bonds and L the normalising length.

Due to symmetry reasons in the crystal structure, it is sufficient to consider only two intervals of the angle α in a sector of $\pi/2$ in the parametric space, defined as seen in Fig. 4.7 (a).
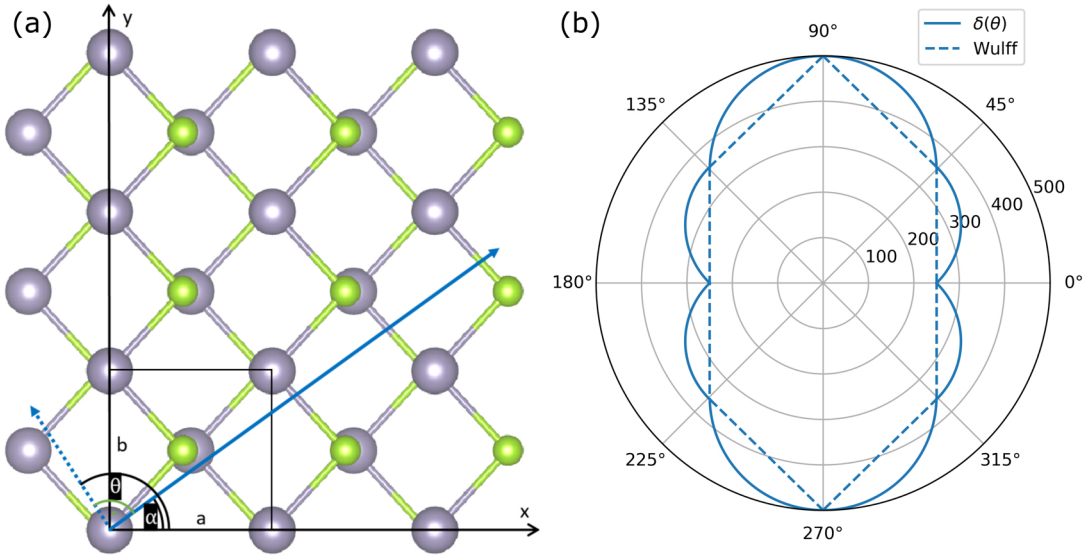
Figure 4.7: (a) Tin selenide atomic structure with unit cell in parametric space. An arbitrary vector (blue) with angle α and corresponding orthogonal vector (blue dashed) with angle θ are shown. Therefore the angle α can be expressed by $\tan(\alpha) = \frac{y}{x}$. The conventional angle θ is defined by $\theta = \alpha + \frac{\pi}{2}$, located between the orthogonal vector and the x-axis. (b) Edge energy $\delta(\theta)$ (in meV/Å) calculated from a simple bond-counting model (further explained in text), with corresponding Wulff construction (dashed) is shown in a polar plot to emphasise the angular dependency.

For $0 \leq \alpha \leq \tan^{-1}\left(\frac{b}{a}\right)$ an arbitrary vector can be expressed as

$$\begin{pmatrix} x \\ y \end{pmatrix} = m \cdot \begin{pmatrix} a \\ b \end{pmatrix} + n \cdot \begin{pmatrix} a \\ -b \end{pmatrix}. \tag{4.2.2}$$

The number of broken bonds N_{bb} is therefore given as

$$N_{\mathrm{bb}} = 2m + 2n \tag{4.2.3}$$

$$\frac{N_{\mathrm{bb}}}{L} = \frac{2m + 2n}{\sqrt{x^2 + y^2}} = \frac{\frac{x}{a} + \frac{y}{b} + \frac{x}{a} - \frac{y}{b}}{\sqrt{x^2 + y^2}} \tag{4.2.4}$$

$$= \frac{\frac{2}{a}}{\sqrt{1 + \frac{y^2}{x^2}}} = \frac{\frac{2}{a}}{\sqrt{1 + \tan^2(\alpha)}} \tag{4.2.5}$$

$$\rightarrow \delta_2(\alpha) = E_{\mathrm{B}} \cdot \frac{N_{\mathrm{bb}}}{2L} = E_{\mathrm{B}} \cdot \frac{\frac{1}{a}}{\sqrt{1 + \tan^2(\alpha)}}. \tag{4.2.6}$$

The remaining α in $\tan^{-1}\left(\frac{b}{a}\right) \leq \alpha \leq \frac{\pi}{2}$ can be calculated in a similar way, with the difference that the cut in direction of b only breaks one bond, which alters the parametrisation of an arbitrary vector as following:

$$\begin{pmatrix} x \\ y \end{pmatrix} = p \cdot \begin{pmatrix} a \\ b \end{pmatrix} + q \cdot \begin{pmatrix} 0 \\ b \end{pmatrix}. \tag{4.2.7}$$

The number of broken bonds N_{bb} is now

$$N_{\mathrm{bb}} = 2p + 1q \tag{4.2.8}$$

$$\frac{N_{\mathrm{bb}}}{L} = \frac{2p + 1q}{\sqrt{x^2 + y^2}} = \frac{\frac{2x}{a} + \frac{y}{b} - \frac{x}{a}}{\sqrt{x^2 + y^2}} \tag{4.2.9}$$

$$= \frac{\frac{1}{a} + \frac{y}{xb}}{\sqrt{1 + \frac{y^2}{x^2}}} = \frac{\frac{1}{a} + \frac{\tan(\alpha)}{b}}{\sqrt{1 + \tan^2(\alpha)}} \tag{4.2.10}$$

$$\rightarrow \delta_1(\alpha) = E_{\mathrm{B}} \cdot \frac{N_{\mathrm{bb}}}{2L} = \frac{\frac{1}{2 \cdot a} + \frac{\tan(\alpha)}{2 \cdot b}}{\sqrt{1 + \tan^2(\alpha)}}. \tag{4.2.11}$$

As convention, the total step free energy is given with respect to the angle θ, which is the angle between the orthogonal vector and x-axis and can therefore be expressed as $\theta = \alpha + \frac{\pi}{2}$. Due to this conversion $\delta(\theta)$ results as
$0 \leq \theta \leq \tan^{-1}\left(\frac{a}{b}\right)$:

$$\delta_A(\theta) = E_{\mathrm{B}} \cdot \frac{\frac{1}{2a} + \frac{\cot(\theta)}{2b}}{\sqrt{1 + \cot^2(\theta)}} \tag{4.2.12}$$

and $\tan^{-1}\left(\frac{a}{b}\right) \leq \theta \leq \frac{\pi}{2}$:

$$\delta_B(\theta) = E_{\mathrm{B}} \cdot \frac{\frac{1}{a}}{\sqrt{1 + \cot^2(\theta)}}. \tag{4.2.13}$$

The energy needed to break a single bond E_{B} can be calculated from the cohesive energy E_{coh}. Cohesive energy is the energy gained due to crystallization and therefore needs to be adjusted per bond: $E_{\mathrm{B}} = \frac{2}{3} \cdot E_{\mathrm{coh}}$.

Now, this leads to the complete edge energy in all directions, often presented in a polar plot like in fig. 4.7 (b). The Wulff construction is a method to determine the equilibrium shape for a crystal structure in a single phase from any minimised edge energy $\delta(\theta)$. The construction is the geometrical interpretation of the Wulff theorem [82]. In order to obtain the equilibrium shape from the edge energy in a δ plot, a line perpendicular to the radius vector at each point is drawn. The resulting inner envelope of all those lines is then geometrically equivalent to the equilibrium shape [18]. This construction only resembles shape and is not a representation to the island size. The Wulff construction is added to fig. 4.7 (b), indicated by dashed lines. The resulting shape resembles an elongated hexagon with a length to width ratio of *a/2b*. In comparison to the experimental measured islands, as seen in fig. 4.6 (b) with a rhombic shape, there is a clear difference.

To further understand the mechanics behind the equilibrium shape, the edge energy needs to be determined differently. In a different point of view to further support a theoretical investigation is that this simple model leads to $\delta_{\langle 100 \rangle} \propto 1/b \approx 1/a$, $\delta_{\langle 010 \rangle} \propto 2/a$ and $\delta_{\langle 110 \rangle} \propto 2/\sqrt{a^2 + b^2} \approx \sqrt{2}/a$. From this view, the $\langle 100 \rangle$ are energetically favoured and should dominate the island shape. Therefore, the experimental finding of preferred formation of $\langle 110 \rangle$ is surprising. As discussed in sec. 2.3., 2D relaxation and reconstruction of edges can be an efficient way to reduce edge energy and therefore transform equilibrium shapes [23, 27, 28, 83]. For this reason, density functional theory (DFT) was used to gain a deeper understanding of the SnSe edges and potential reconstructions, which could be a reason for this discrepancy.

After relaxation of the infinite lattice structure, as presented in fig. 4.1, lattice constants $a = 4.39\,\text{Å}$ and $b = 4.29\,\text{Å}$ and cohesive energy $E_{\text{coh}} = -3.29\,\text{eV/atom}$ could be determined. The calculations also result in a spontaneous polarisation of 0.11 C/m^2 along the [100] direction. These results are in good agreement with other calculations in both lattice constants and cohesive energy [8, 84, 85], as well as the experimental results, shown earlier.

The cohesive energy E_{coh} of the structure was calculated as the difference between the energy of atoms in the 2D infinite SnSe crystal with respect to the number n and chemical potential μ of the isolated atoms:

$$E_{\text{coh}} = \frac{E_{\text{SnSe}} - n_{\text{Sn}}\mu_{\text{Sn}} - n_{\text{Se}}\mu_{\text{Se}}}{n_{\text{Sn}} + n_{\text{Se}}}. \tag{4.2.14}$$

Edge energies were obtained by calculating the energy of a ribbon with two edges of a specific type, which has a finite width perpendicular to the edges but extends infinitely parallel to them. With this method, the edge energy δ for a specific edge is determined by the difference between the specific ribbon and the periodic slab structure, normalised to the edge length:

$$\delta = \frac{E_{\text{ribbon}} - E_{\text{slab}}}{2L}. \tag{4.2.15}$$

Three ribbons ($\langle 100 \rangle$, $\langle 010 \rangle$ and $\langle 110 \rangle$) contain all five different dense-packed edges, because of the low symmetry of the lattice and can be individually seen as cuts from a large SnSe structure containing all different edges, as shown in fig. 4.1.

In a strict manner, it is even impossible to define the edge energy of a given energy in such a low symmetry lattice. It is only possible to calculate the average energy of a pair of two edges related by symmetry. Despite this, the resulting shape is still uniquely defined and can therefore be calculated [65].

DFT calculations result in a general observation that $\delta_{\langle 110 \rangle} < \delta_{\langle 010 \rangle} < \delta_{\langle 100 \rangle}$, which is in agreement with the experimental observations. In contrast to other 2DMs, the exact energies strongly depend on the details of the theoretical model. This behaviour is exemplified by different ribbon widths, as presented in fig. 4.8 for (a) $\langle 100 \rangle$- and
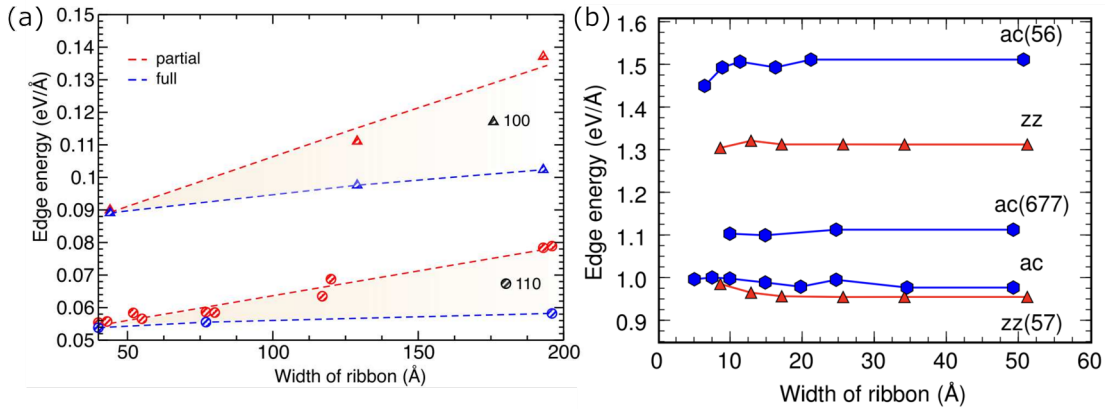
Figure 4.8: Dependence of the edge energy δ on the width of the ribbon for (a) SnSe [66]. The results are compared for different optimization methods i.e. with ('full') or without ('partial') relaxation of the lattice constant perpendicular to the edge. This rather unconventional behaviour is highlighted by the comparison to graphene in (b) (adapted from [22]), where no dependency on ribbon width is present.

$\langle 110 \rangle$-edges of SnSe and (b) AC and ZZ edges of graphene [22]. In order to estimate the true edge energy of the edges, different ribbon widths (from 40 Å up to 200 Å) were used, whereas each ribbon was either allowed to fully optimise the supercell or only partially with the restriction that the lattice parameter perpendicular to the edge is held to the value of the 2D infinite lattice. With both methods, the edge energy of a particular direction can be assumed by an upper bond from the partial and a lower bond from the full optimization.

Unsurprisingly, any edge energy is lower for the fully optimised model. An interesting trend can be seen for the dependence on ribbon width. The edge energy increases with width for all directions, compare fig. 4.8 (a), whereas $\langle 010 \rangle$ is not shown, but behaves analogously. Therefore, it is important to state that for the equilibrium shape analysis, the difference between the edge formation energies of the various types matters more, since the edge energy values converge only very slowly with increasing ribbon width. As Koskinen *et al.* [22] demonstrate for graphene, already at rather small ribbon widths edge energies remain constant for different directions and reconstructions.

The slow convergence in SnSe is due to the fact that even for the widest ribbons, the structural position of each atom relaxes throughout the whole system, in comparison to just the edges. In a broader way, the atoms are shifted from their equilibrium position to the atom positions of the paraelectric phase. One unit cell of the middle of the widest fully optimised $\langle 110 \rangle$-ribbon was repeated periodically. This results in a 2D infinite lattice structure, which is only 2 meV/uc larger than the 2D infinite equilibrium lattice. Such an energy gain is small compared with the reduced energy due to relaxation, enabling the ribbon to relax throughout the full width. However, this energy gain would still be dominant at some critical width, where the interior lattice of the ribbon will convert to the equilibrium structure. Unfortunately, the determination of such a large critical width is beyond available computational capabilities.

Other studies also report similar findings. The potential energy landscape of freestanding SnSe was investigated with respect to a variation of the lattice constants a and b [43], which results in an energy difference between the ferroelectric ground state and the paraelectric transition state of just ≈ 13 meV/uc. This can be seen as the maximal energy gain due to lattice distortion, which is still comparably small to the energy due to edge relaxation. As a result, a ribbon in the computational model within a system that is close to a phase transition, like for SnSe, is undergoing the transformation towards

the paraelectric phase. With this its edge energy is lowered, although its compensating the energetic penalty for the phase transition. Those competing mechanisms can be of the same magnitude in energy and are most pronounced for the narrowest ribbons.

In another recent study, the atomic positions of bulk SnSe were studied in detail through dynamic order-disorder phase transitions [86]. This results in the potential energy landscape being rather flat and could even entail additional local minima.

The mechanism to fully relax throughout the full width to the paraelectric phase can be excluded for the experiment since lattice constants do not convert to a square lattice but are always $a \neq b$. The values derived from the widest ribbons are assumed to be the most reliable ones and therefore listed in table 4.2. Those values are also used in any further prediction of the equilibrium shape. This comparison of energies also emphasises the important role of relaxation in this system, since there is an energy reduction of up to 80 % between the simple bond-counting model and the DFT calculated values.

	$\delta_{\langle 100 \rangle}$ (ZZSe / ZZSn)	$\delta_{\langle 010 \rangle}$ (AC)	$\delta_{\langle 110 \rangle}$ (ACSn / ACSe)
bond-counting model	0.256	0.500	0.357
DFT (non opt.)	0.231	0.177	0.141
DFT (partially opt.)	0.137	0.089	0.079
DFT (fully opt.)	0.102	0.088	0.058

Table 4.2: Edge energy δ in eV/Å from the different types of edges using the simple bond-counting model (see text) with $E_{\mathrm{bond}} = \frac{2}{3} E_{\mathrm{coh}}$ and three flavours of DFT calculations (see text).

For the full derivation of the equilibrium shape the edge energy $\delta(\theta)$ is necessary. In order to model any other energy, a similar interpolation ansatz as described in the supplementary section 5 of Ref. [65] is used. Less dense packed edges are compositions of segments of the main edges and therefore also the energy compounds accordingly to the basic energies. After trigonometry transformations, the general edge energy can be expressed through the following equations, for $0 \leq \theta \leq \tan^{-1}\left(\frac{a}{b}\right)$:

$$\delta(\theta) = \frac{\delta_{\langle 110 \rangle} - \delta_{\langle 010 \rangle} \cdot \frac{\xi \cdot \tan(\theta)}{\sqrt{a^2 + b^2}}}{\sqrt{1 + \cot^2(\theta)}} \tag{4.2.16}$$

where $\xi = 5.24$ is an adjustment factor to fulfill continuity conditions and for $\tan^{-1}\left(\frac{a}{b}\right) \leq \theta \leq \frac{\pi}{2}$:

$$\delta(\theta) = \frac{\frac{\delta_{\langle 110 \rangle}}{b} \cdot \sqrt{a^2 + b^2} + \delta_{\langle 100 \rangle} \cdot \left(\tan(\theta) - \frac{a}{b}\right)}{\sqrt{1 + \cot^2(\theta)}} . \tag{4.2.17}$$

This conversion leads to the complete edge energy in all directions, presented in a polar plot in fig. 4.9 for all three flavors of the DFT calculation. In subfigure (b) the corresponding Wulff constructions for the calculated edge energies $\delta(\theta)$ can be seen.

The full edge energy $\delta(\theta)$ presents the values of table 4.2 in a polar plot. It can be directly seen that due to relaxation the energies in all directions decrease significantly. Evaluating the two different optimised models, which in this case represent upper and lower boundary values of the respected edge, show that the significant change is due to much reduced energy at $\delta_{\langle 100 \rangle}$ and $\delta_{\langle 110 \rangle}$. These values are demonstrated between the angles around $0° \pm 46°$ and $180° \pm 46°$.

Fig. 4.9 (b) displays the same functions in a polar plot with added Wulff constructions in dashed lines. For demonstrative purposes, the same colours as in (a) were used and
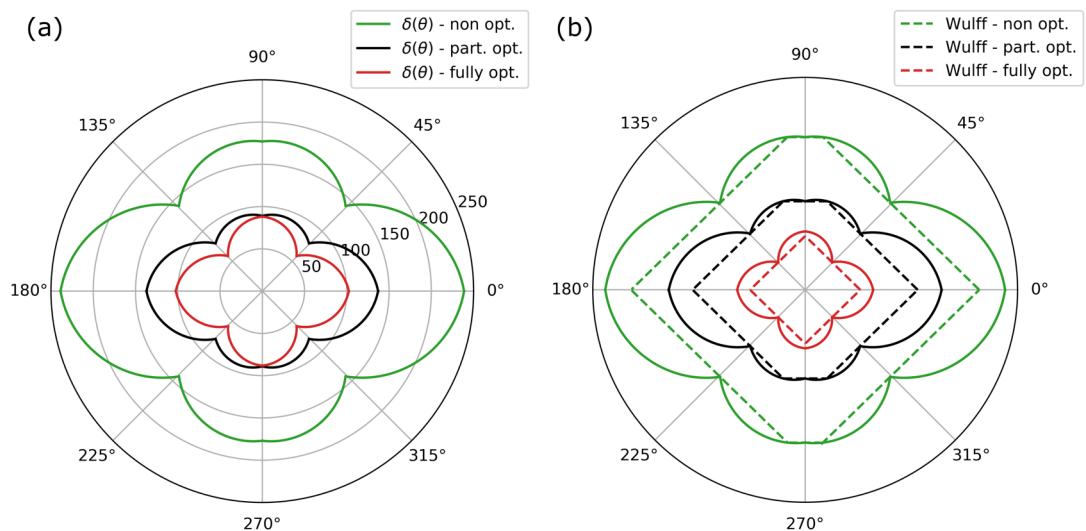
Figure 4.9: Edge preference from different relaxation models. (a) Edge energy $\delta(\theta)$ (in meV/Å) at $\mu = 0\,\text{eV}$, for three DFT models: non optimised (green), partially optimised (black), and fully optimised (red). (b) Corresponding Wulff constructions (dashed) to each model are shown without scaling dependency to demonstrate the resulting island shapes. While $\langle 110 \rangle$ is the most preferred edge for all models, there is an occurrence of $\langle 010 \rangle$ edge for non and partially optimised models.

the functions were spaced out more because Wulff-construction provides only the shape. It can be clearly seen that most edges are determined by the energy value at $\langle 110 \rangle$. Only at the non and partially optimised models, the effect of an $\langle 010 \rangle$ edge is noticeable. Due to the overestimation of energies in the partially optimised model and the fact that $\langle 110 \rangle$ edges are energetically favourable after relaxation, it can be assumed that the equilibrium shape is primarily defined by a rhombus, as seen also in red for the fully optimised model.

This shape is also in agreement with the experimental results, presented in fig. 4.6 (b) as a comparison with the overlay of the red Wulff construction from fig. 4.9 (b). The description of a rhombus of only $\langle 110 \rangle$ and no other edges is consistent. The only difference between the experiment and the predicted shape from the Wulff construction can be found in the corners which are rounded. A reason for this deviation is that this method of shape determination does not take into account any entropy effects at temperatures above $0\,\text{K}$, which prohibit the formation of sharp corners. Nevertheless, this does not alter the fact that the $\langle 110 \rangle$ edge is the primary shape-defining element. Similar to the argument used earlier, the dependence of the actual edge energy on ribbon width and boundary conditions is not shape-defining, but the decisive parameter is the ratio of energies. For a group of ribbons with the same widths and optimization conditions, these ratios are approximately constant.

Wang *et al.* also cover calculations on stoichiometric SnSe edges at various chemical potentials [65], but only consider very narrow ribbons with a width of $\approx 20\,\text{Å}$. At $\mu = 0\,\text{eV}$, the equilibrium shape also resembles a rhombus, even with quantitative agreement in energies to the presented values for a similar sized ribbon.

While taking a closer look at the edge in STM measurements, the lattice does not continue seamlessly until the edge of the island. This atomic change is the result of the edge relaxation in the $\langle 110 \rangle$ edge, which can be seen in fig. 4.10. As outlined in the beginning of this chapter, no difference between any $\langle 110 \rangle$ edge can be seen in STM. Therefore only one example is shown here. The 2D lattice inside the island
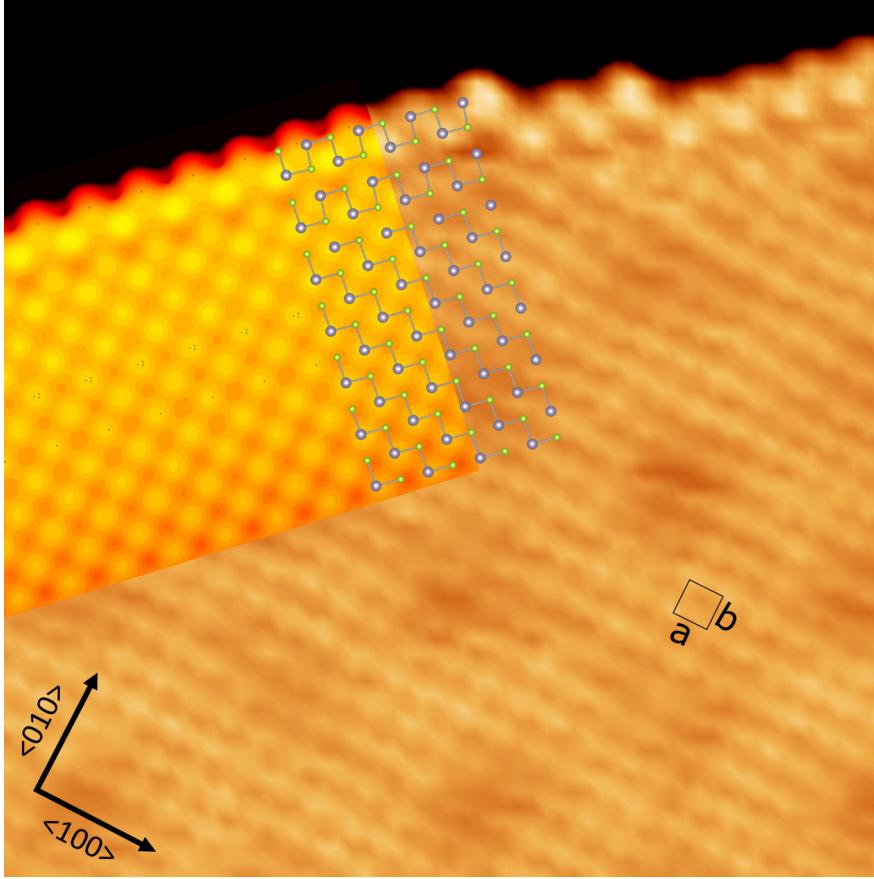
Figure 4.10: Atomically resolved STM image of SnSe island with edge reconstruction in $\langle 110 \rangle$ direction; ($100\,\text{Å} \times 100\,\text{Å}$, $1\,\text{V}$, $200\,\text{pA}$), grown at ($5.2 \times 10^{-3}\,\text{ML/s}$, $60\,\text{s}$, RT) and subsequently ($1.72 \times 10^{-3}\,\text{ML/s}$, $300\,\text{s}$, $570\,\text{K}$). The topography is superimposed with a simulated STM image (top left). On top of the measured and simulated STM images the atomic structure obtained by DFT is superimposed (only the topmost atoms included).

consists of the typical rectangular structure and moiré superstructure, which starts to be interrupted up to two atomic rows parallel to the $\langle 110 \rangle$ edge. At this position also an alteration of the spacing of the atomic rows takes place, which is an increase of around 6% compared to the interior of the island after the second row. The edge also appears brighter than the interior lattice in STM.

The DFT model of the relaxed structure also contains an increased row distance close to the edge, see fig. 4.11. This change in lattice parallel to the $\langle 110 \rangle$ edge is in turn mostly compensated by the first and third atomic row. In addition, a constant current STM image simulation of the edge was performed and can also reproduce the bright contrast at the edge which is in turn followed by a darker gap. The simulation was performed using the Tersoff-Hamann approximation. All states up to $1.2\,\text{eV}$ above the highest occupied state were incorporated, since this is estimated to be the best match to the experimental image measured at a bias voltage of $1.0\,\text{V}$. DFT model (top row only, for full model see fig. 4.11) and simulation are both added as overlay in fig. 4.10, where the model overlaps both simulated and experimental STM images. This is another indication that there is a good agreement between experiment and theory for the model of edge relaxation.

In order to reflect the importance of the ionic bonds in the extraordinary reduction in edge energy due to relaxation, a comparison to the isostructural material phosphorene
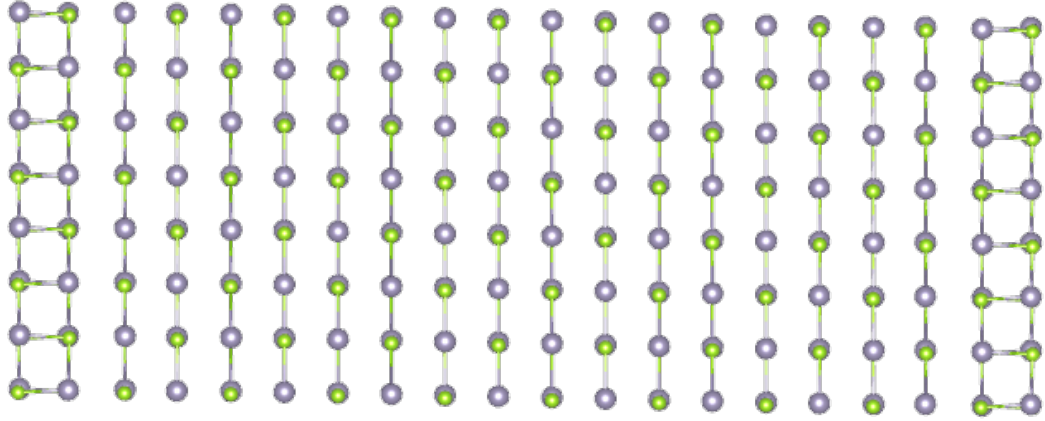
Figure 4.11: Structural model from DFT calculations of the fully optimised $\langle 110 \rangle$ ribbon, where the edges are located on the left and right.

with only covalent bonds would be helpful. Unfortunately, the work from Masih Das *et al.* only incorporated the edges corresponding to $\langle 100 \rangle$ and $\langle 010 \rangle$ [23], as already mentioned in sec. 2.3. For these edges, the energy reduction from the relaxation mechanism is up to 26% compared to the simple bond counting model, introduced earlier.

For further insight into the stability of various edge orientations and the option of different terminations, including non-stoichiometric edges, the calculations were extended to edge energies in dependence of the Se chemical potential, which is shown in fig. 4.12. Several edge compositions are presented, ranging from 0 up to 100% Se coverage in steps of 25%, indicating the Se concentration at the edge. Hence, fully covered Se edges are stoichiometric, the others present a Se deficiency and are non-stoichiometric. Contrary to the stoichiometric edges, here there are several cases with a change in lattice periodicity, which means that also a reconstruction takes place. In terms of energetic values, the stoichiometric $\langle 110 \rangle$ is the most favourable one and lower than any other non-stoichiometric edges, even over the wide range of the Se chemical potential.

As already shown for the different optimised DFT models, edge energy values can be used to predict island shape via a Wulff construction. This can be seen in fig. 4.13, which demonstrates all Wulff constructions from the data shown in fig. 4.12.

At full Se coverage, the stoichiometric case, the already presented rhombic shape can be seen. The influence on other edges starts at deviations of the ideal edge compositions. The shape changes from rhombic to octagonal, due to facets stemming from the $\langle 100 \rangle$ and $\langle 010 \rangle$ edges. The presence of these edges dominate the shape at lower Se contents, but at the same time, there is no trend to decrease $\langle 110 \rangle$ edge proportion. There are fluctuations in the composition. Notably, some $\langle 110 \rangle$ edge stays present throughout the whole range of Se coverage, resulting in all three edge types being present at Se deficient edges. Although no direct correlation between edge type appearance and Se content could be found, this insight gives awareness to other possible island shapes due to deviations in edge stoichiometry.

There are significant hints that previously discussed experimental SnSe islands are stoichiometric. In energetic terms, the stoichiometric $\langle 110 \rangle$ edge is lower than any other edge, considering different stoichiometry, type, and chemical potentials. Therefore, even for minor deviations from the ideal ratio, the equilibrium shape presented here will be reached. Another strong argument is that, the evaporation from a single source leads to SnSe dimers which can be found as the primary content in QMS measurements. And also
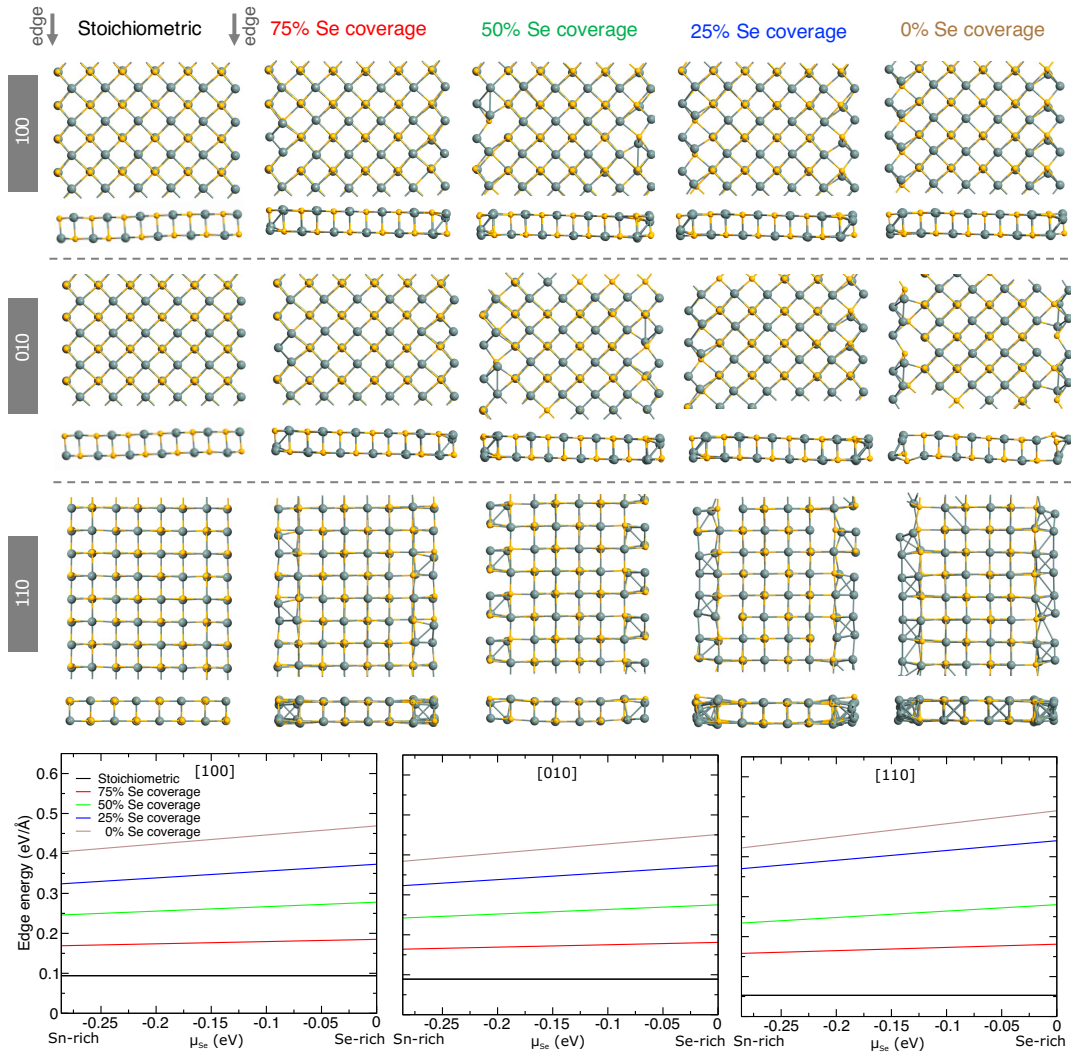
Figure 4.12: Atomic structures and edge energies δ of stoichiometric and non-stoichiometric SnSe edges as functions of Se chemical potentials μ and Se coverage in steps of 25% from 0 to 100%, where lastly mentioned represents the stoichiometric state. Atomic models for the three edges ($\langle 100 \rangle$, $\langle 010 \rangle$ and $\langle 110 \rangle$) are shown with top and side view. Below are the edge energies in dependence of the chemical potential summarised for each edge and Se coverage.

other experimental reports state that even in significant non-stoichiometric conditions (large deviation from the ideal 1:1 flux ratio) the stoichiometric SnSe is formed and therefore is the most stable form [87, 88]. Therefore, the non-stoichiometric study can be seen as demonstrating the importance of edge relaxations and reconstructions in this material. It is also important for systems which are using alternative preparation methods compared to evaporation from SnSe powder as a single source, like co-evaporation of Sn and Se using two effusion cells which is already used by others for the growth of multilayers [87, 88], by trying to achieve metastable edge configurations. In principle, this preparation method could also be used for monolayer growth. It enables the option to tune the fluxes of Sn and Se independently from one another. Although the aforementioned reports did not find the absence of no non-stoichiometric gowth, it can be expected that there could be a deviation of the Sn:Se ratio at the edges which differs from the 1:1 bulk ratio.
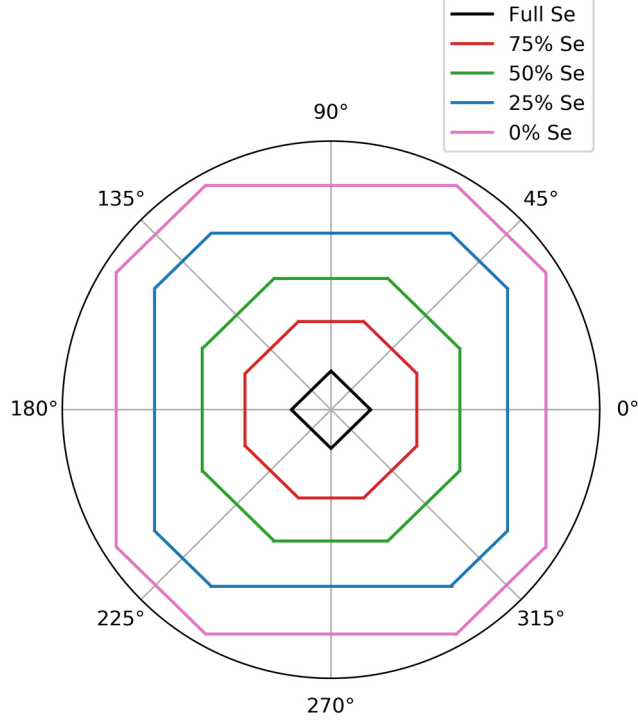
Figure 4.13: Shape influence on stoichiometry. Wulff plots, constructed from edge energies of stoichiometric and non-stoichiometric SnSe edges, shown without any scaling dependency. Colour and Se coverage steps are identical to fig. 4.12.

4.3 Effect on electronic structure

Chang *et al.* presented in a groundbreaking study that rhombic shaped tin selenide monolayer exhibit a strong ferroelectric behaviour [9]. They measured the in-plane electrical polarisation of large islands in the range of tens of nm, similar to the ones grown in this thesis, by measuring the band bending of valence and conduction band due to an increased / decreased electrostatic potential at the edges. This results in large electric fields, which are ideally measurable at low temperatures. The estimated experimental Curie temperature is $380 - 400\,\mathrm{K}$ [9]. This study was performed on graphitised 6H-SiC(0001), where some differences could arise compared to the nearly freestanding gr on Ir(111) surface used here. It is known for metal substrates, that the substrate interaction can be estimated by the gr-metal separation. In this special case, this also correlates with the energy of the d-band center of the transition metal [89]. Another major difference are the different characteristics of metal and insulator.

Due to these differences and the newly reported edge relaxation [66], there could be differences in the electronic properties as well. Therefore the electric potential landscape of a SnSe island is investigated theoretically. For that an island with a significant size, in this case 4000 atoms, resulting in edge lengths of $\approx 100\,\text{Å}$, was used. It consists in principle of only $\langle 110 \rangle$ edges, as presented in fig. 4.14. Parallel to x is the periodic slab structure, while the edge at the top and bottom is allowed to optimise.

The potential V of each position was calculated by adding up all charges Q_i in dependency of their polarity and relative distance:

$$V = \frac{1}{4\pi\epsilon_0} \sum_{i=1}^{n} \frac{Q_i}{r_i},$$
(4.3.1)

where ϵ_0 is the vacuum permittivity and r_i is the distance between the calculated position and atom i. The reference plane is set to the middle of the SnSe layer, the average of each z-component of the atomic positions.
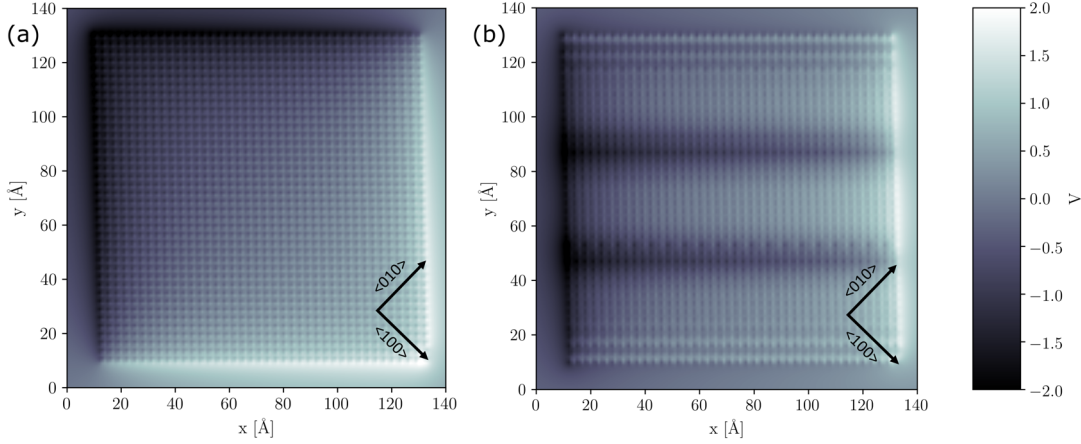

Figure 4.14: Electric potential of SnSe islands from (a) non optimised and (b) optimised model. Each island consists of 4000 atoms. Orientations are marked in the image. Both graphs share the same colour scale seen on the right-hand side.

The structural data from the DFT model, mentioned earlier are extended along x to minimise effects of the periodic edge and used here: the non optimised and fully optimised structures. The charges for the non optimised model were constant at $0.84e$. The resulting electric potential can be seen in fig. 4.14 (a) and (b) for non and optimised model, respectively.

Both structures are on the same length and colour scale, seen on the right-hand side of the figure. The calculations clearly show that one edge (bottom, low x values) exhibits a positive and the opposite edge a negative potential. This is already present due to the nature of the crystal structure itself, as seen in subfigure (a). The larger potential values at the edge subside quickly to a level close to 0. The reduction to a constant value in the 2D-bulk area can be explained by a screening effect [90]. The influence of additional charges equalises any electric field and only edge effects with broken bonding contribute to the potential landscape. The non relaxed edges (along the periodic axis) also exhibit an edge effect, because they are also $\langle 110 \rangle$ type edges. A periodic pattern in the interior of the island can be seen which is due to the positions of the atoms, which is also visible for the optimised model. As already discussed for the optimised structure, the increased spacing in the lattice parallel to the $\langle 100 \rangle$ edge at the relaxed edge can also be seen in potential. There is still the same edge effect with the same polarity (positive and negative) in potential but in a reduced form. The interior of this island exhibits some periodic corrugation which is not visible in structural data. This will be seen as an artefact in the calculation. Since the relevant part is the edge and the edge effect is rather localised, it will be excluded from the analysis, similar to the effect at the periodic edge.

In order to compare the effect of the relaxation on potential, ribbons of a length of $40\,\text{Å}$ close to the edge are selected and presented in fig. 4.15. Not only the previously shown models are shown ((a)-(d)), but also a calculation that includes the effect of a metallic substrate underneath. Metallic substrates often induce mirror charges. For this, the charges of the same polarity, x and y position as their counterpart are replicated in a distance of $\Delta z = -5.22\,\text{Å}$.

The figure is divided into six subfigures, where the top ones ((a), (c), and (e)) represent
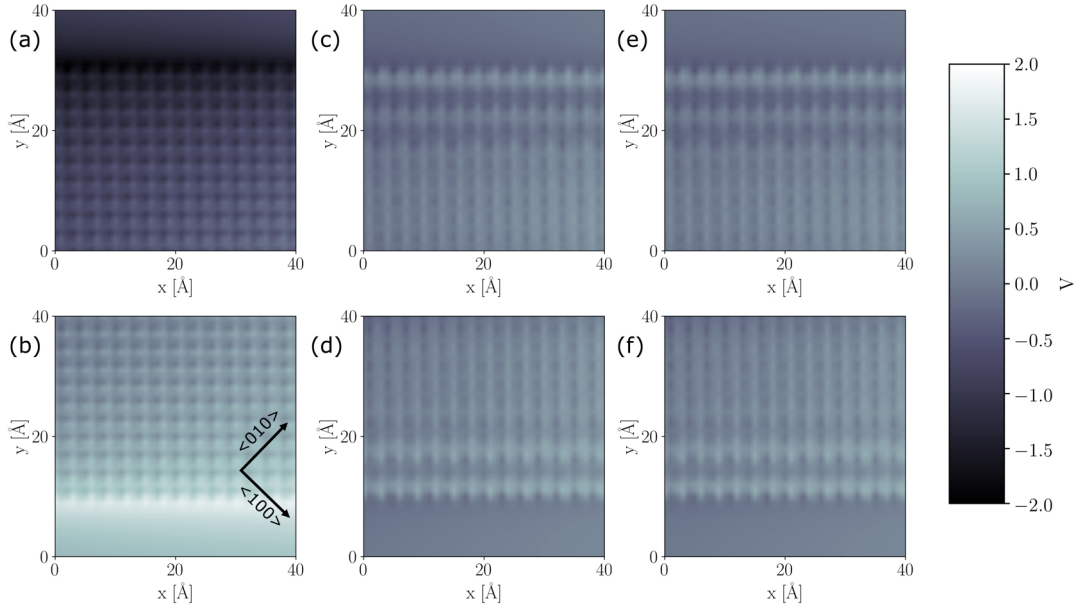
Figure 4.15: Electric potential comparisons in the form of same-sized ribbons at the edge between (a),(b) non optimised model, (c),(d) optimised model including Bader charges and (e),(f) the model from (c),(d) with mirror charges introduced. The top row (a), (c), (e) represents the negative edge, while the bottom is the positive one. The structural change due to the edge relaxation can clearly be seen. Orientations are marked in (b) and are the same for all images. Every image is colour-coded to the scale on the right-hand side.

the negative edge and the bottom row the positive edge. Each pair corresponds to the models non optimised, optimised, and optimised with mirror charges, respectively. This method with a constant colour scale for all subfigures allows a visual comparison between the individual models, where a clear reduction in potential can be seen from left to right. Comparing the values at the edge, the decrease in potential from non optimised at $\pm 1.90\,\mathrm{V}$ to $\pm 0.62\,\mathrm{V}$ in the optimised structure is the largest effect. The introduction of mirror charges reduces the potential further to $\pm 0.52\,\mathrm{V}$ in the model shown in (e) and (f).

This does not only reflect a large reduction in electrical potential at the edge but it can also be seen as a value for polarisation due to a proportional relation. Therefore, this should also result in lower maximal polarisation values.

Experimentally, the electronic structure can be investigated by STS, which probes the local density of states. In the 2D-bulk area, a bandgap of $2.153 \pm 0.047\,\mathrm{eV}$ can be detected, which is presented in fig. 4.16 (a). This is similar to other experimental results, which state a bandgap of $2.13\,\mathrm{eV}$ with similar valence and conduction band onsets [9]. This is surprising, since literature and band structure analysis from first-principle calculations, shown in fig. 4.16 (b), suggest a direct bandgap of $0.91\,\mathrm{eV}$. Besides the band structure, the DOS is given with respect to the bands stemming from Sn (blue) and Se (orange). It is known that STM is most sensible to the band structure at Γ, where theoretically a direct bandgap of $2.16\,\mathrm{eV}$ is predicted. This value is in good agreement with experimental results.

In order to investigate the edge of the islands experimentally, low-temperature STS would be needed due to the largely reduced edge effect, as argued by the reduction in electrical potential. In the experiments used for this thesis, no clearly from noise level distinguishable effect at the edge could be observed.
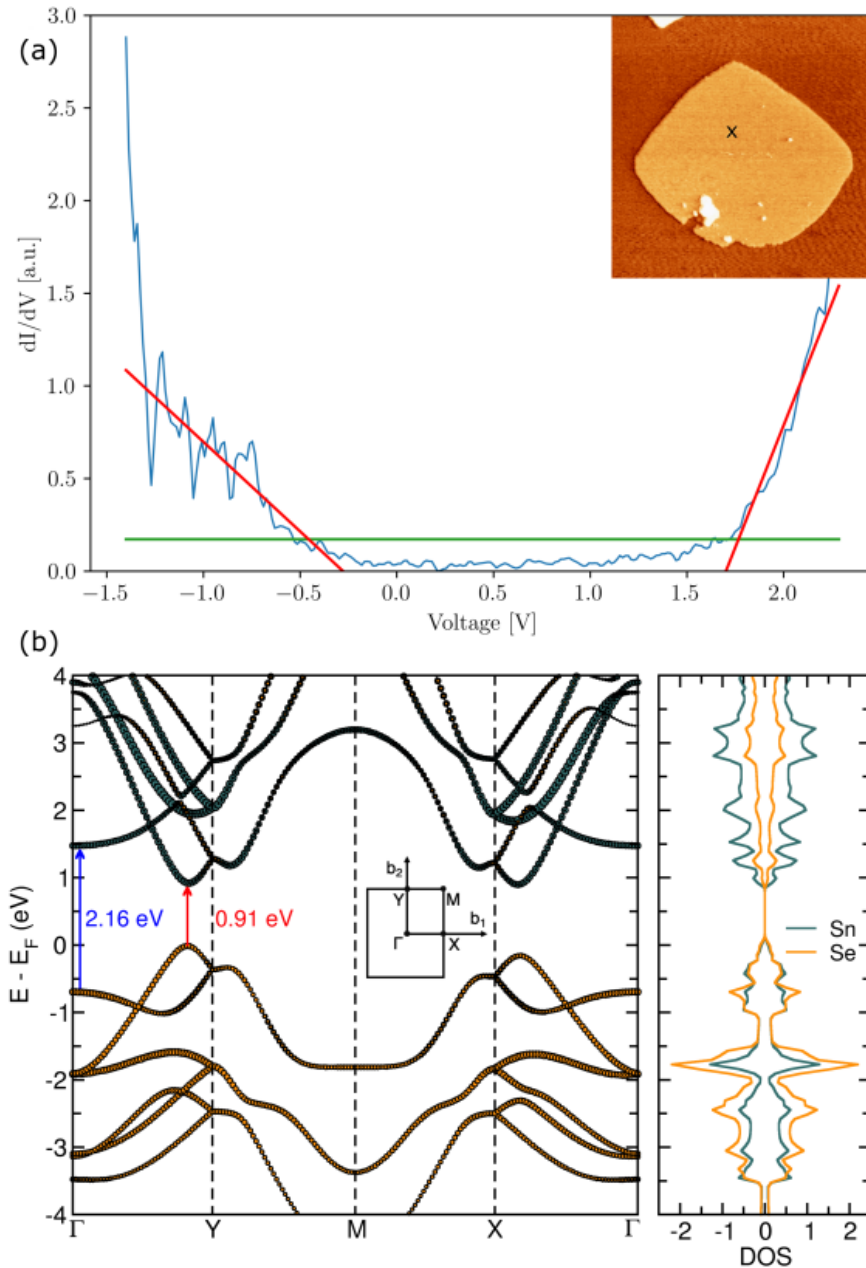
Figure 4.16: Bandgap of a ML SnSe island on gr/Ir(111). (a) *dI/dV* measurement of the 2D bulk, resulting in a bandgap of $2.153 \pm 0.047\,\text{eV}$ with the corresponding island as inset ($1\,500 \times 1\,500\,\text{Å}$, $-0.3\,\text{V}$, $50\,\text{pA}$, $T = 120\,\text{K}$) grown at ($5.2 \times 10^{-3}\,\text{ML/s}$, $15\,\text{s}$, RT) and subsequently ($1.72 \times 10^{-3}\,\text{ML/s}$, $300\,\text{s}$, $570\,\text{K}$). STS were measured with $V_{\text{mod}} = 20\,\text{mV}$ and $\nu_{\text{mod}} = 1337\,\text{Hz}$. The red lines are fitted to the initial slope, the green line represents the error-free level at $3\,\sigma$ above the noise level in the gap. (b) Bandgap calculation from first-principle studies, resulting in a direct bandgap of $0.91\,\text{eV}$. Band structure and DOS are given with respect to bands stemming from Sn (blue) and Se (orange).

Chapter 5

Bilayer formation of SnSe on gr/Ir(111)

Although bilayer (BL) SnSe islands are not candidates for two-dimensional ferroelectrics, the study of second layer formation can give further insight into the growth process. Such bilayer structures can express vastly different characteristics to their monolayer counterpart. For example, it is known that the isostructural black phosphorous is able to form a second layer quite easily as well. Interestingly, many electronic properties are strongly dependent on the induced strain or stacking configurations [39], and new properties, like magneto-transport, can emerge [91].

This chapter focuses on the growth conditions needed to form bilayer structures and their characterisation by STM and LEED measurements (sec. 5.1). Furthermore, a first look into their electronic structure and, based on these results, stacking order options are given (sec. 5.2).

5.1 Growth and orientation

For SnSe on gr/Ir(111), the formation of a second layer is observed rather quickly and the preparation in chapter 4 needed a two-step process to actively avoid those conditions. This happens likely due to the preference to counter the ferroelectric island and form antiferroelectric stacking from two oppositely orientated layers.

This chapter still uses the two-step process and therefore the starting point is the growth from the monolayer. However, high coverage, rates, or evaporation duration in the first nucleation step at room temperature, directly lead to the formation of a second layer and thus to BL growth. Once this regime is entered, BL growth is strongly preferred and monolayer islands become rare/non-existent. A similar temperature dependence on the shape as described for the island compactification in sec. 4.1 could be observed and therefore mainly islands close to the equilibrium shape will be investigated here.

Fig. 5.1 (a) shows a large-scale STM image. Multiple islands in close proximity across several Ir steps on the unaffected gr surface can be seen. These steps are also visible through the islands. The coverage is high due to a long evaporation time in the second step. Most islands have straight edges with rounded corners but form irregular shapes. This can be led back to the fact that each island is a combination of smaller rhombic islands itself. Those are in line with the shape of ML islands at the annealing temperature of 585 K. Similar to ML islands, these edges stem from the ⟨110⟩ facets. Note that the presence of holes inside a larger island, which were not present in ML growth, can be explained by a combination of correctly placed rhombic islands. A possible reason why these gaps do not grow together can be due to differences in the orientation of the original island or due to charge effects at the edges. It can be assumed that due
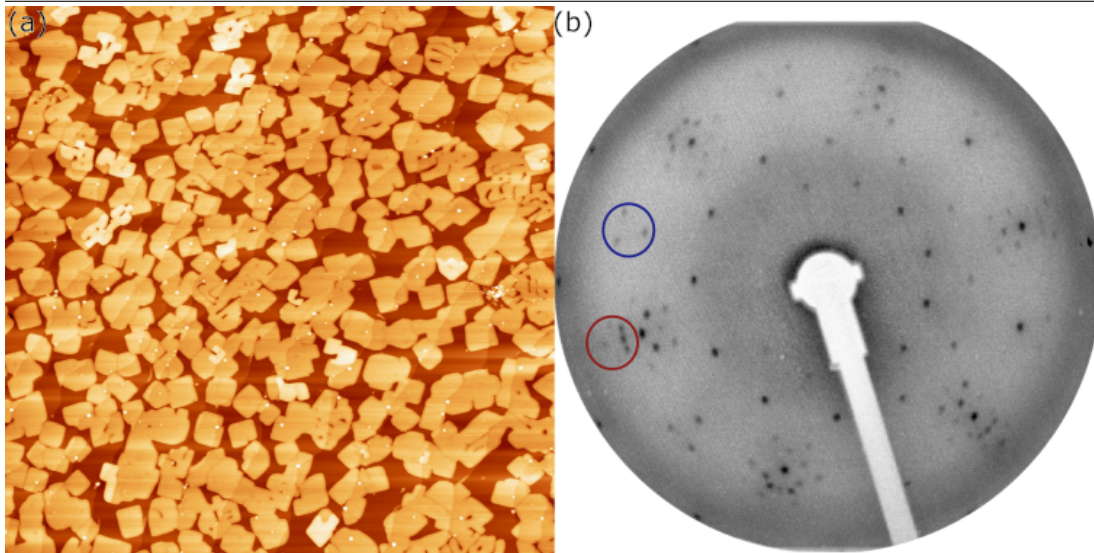
Figure 5.1: (a) Overview STM image of multiple bilayer SnSe islands on gr/Ir(111), grown at $(5.2 \times 10^{-3}\,\mathrm{ML/s}, 30\,\mathrm{s}, \mathrm{RT})$ and subsequently $(1.72 \times 10^{-3}\,\mathrm{ML/s}, 900\,\mathrm{s}, 585\,\mathrm{K})$ $(20\,000\,\text{Å} \times 20\,000\,\text{Å}, -300\,\mathrm{mV}, 50\,\mathrm{pA})$, with occasional third layer, resulting in a total coverage of $\Theta = 1.46\,\mathrm{ML}$. (b) Diffraction spots in LEED at higher energies than typical images seen before $(100\,\mathrm{eV})$ after deposition of $\Theta_{\mathrm{total}} = 1.96\,\mathrm{ML}$. Additional reflexes compared to ML measurements are highlighted in red and blue.

to this observation, islands do not change their orientation or dipole momentum after nucleation. But two islands can grow together, into one larger one, which is typically known as Smoluchowski ripening.

In order to characterise the coverage in more detail, different layers need to be defined. For this reason, the naming scheme as bi- and trilayer with a height of $12\,\text{Å}$ and $18\,\text{Å}$, respectively, is used. In the given image nearly all islands are bilayer structures, while only the very bright overlayers are a third layer. This results in coverage of the second layer alone $\Theta_{\mathrm{2L}} = 0.68\,\mathrm{ML}$ and the third layer $\Theta_{\mathrm{3L}} = 0.04\,\mathrm{ML}$. The total coverage can then in turn be calculated as $\Theta = 1.46\,\mathrm{ML}$.

At a closer look, not only iridium step edges can be seen through the islands, but also vaguely domain boundaries between two smaller rhombic islands. This means that bilayer islands also have low interaction with the substrate, with a similar argumentation as for the monolayer structures. Domain boundaries can be explained by the merging of two differently orientated islands.

Fig. 5.1 (b) shows the LEED measurement of BL SnSe at $100\,\mathrm{eV}$. At the smaller lattice parameter (outer part of the image) first-order Ir and gr spots with the moiré satellite pattern can be seen. Further inside the grouped 3 times 8 spot pattern for SnSe can be seen. As discussed for monolayer SnSe, similar orientations can be identified. For lower diffraction energies, there is no significant difference in LEED between mono- and bilayer SnSe visible. At such higher energies, the appearance of additional diffraction spots, which are not present for ML, can be seen. Instead of only one spot above the gr reflection, the pattern is split up, see highlighted part in red. This six spot pattern resembles a crown with a base of three and another three in a upward-facing triangle above that. There is also a pattern between the gr/Ir(111) reflexes which can be described as three spots in a inward-facing triangle, highlighted in blue. This pattern can be used to differentiate monolayer from the existence of additional layers. With this knowledge, in a direct comparison between monolayer and bilayer SnSe, a slight broadening of the first-order diffraction spots should be observed. This can not be
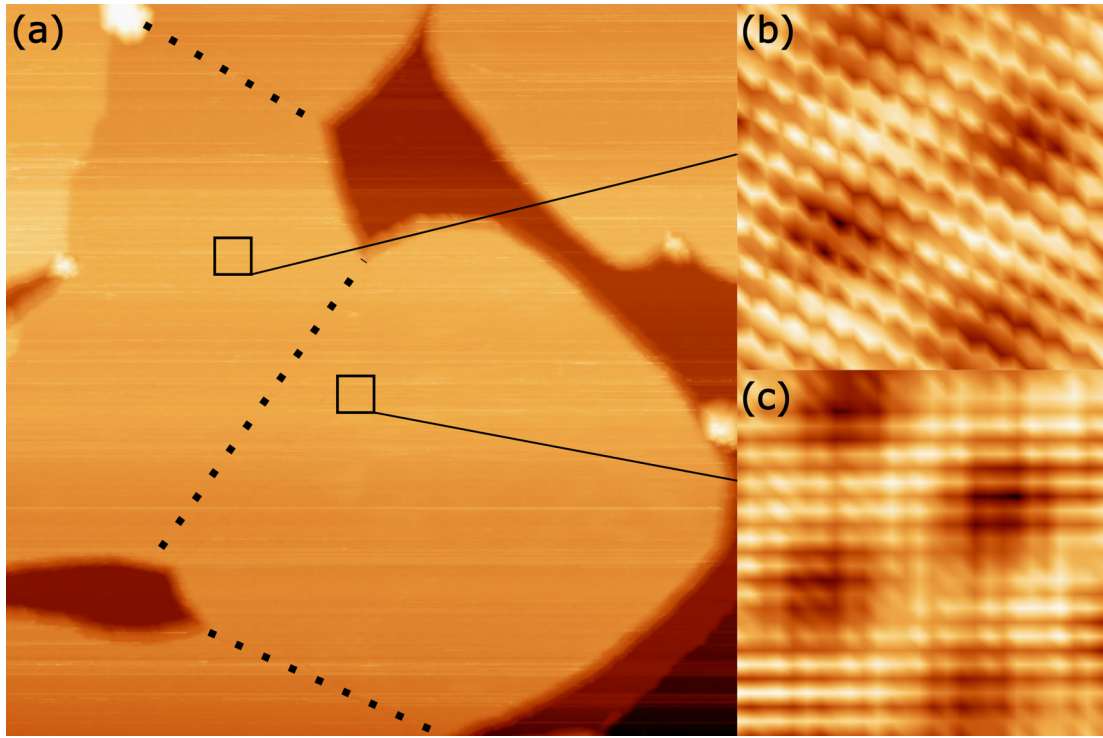
Figure 5.2: SnSe bilayer islands grown together creating domain boundaries. (a) Overview STM image, grown at $(5.2 \times 10^{-3} \, \text{ML/s for 30 s, RT})$ and subsequently $(1.72 \times 10^{-3} \, \text{ML/s, 900 s, 545 K})$, $(1\,500\,\text{Å} \times 1\,500\,\text{Å}, -200\,\text{mV}, 100\,\text{pA})$. (b), (c) Fourier-filtered images, each $(50\,\text{Å} \times 50\,\text{Å})$ in size, of the left and right domain, respectively.

reliably determined due to uncertainty error. Despite those differences both have similar lattice constants a and b. Lattice constant evaluation leads to $a = 4.29 \pm 0.06\,\text{Å}$ and $b = 4.20 \pm 0.04\,\text{Å}$, which do not deviate a lot from the monolayer lattice constants, but are lower than previously reported values. Note that the increased error could suggest a broadening of the reflection spot. Since LEED has an increased depth sensitivity than STM, the broadening can be due to a superposition of two closely similar lattice constants that have the same orientation. The lattice constants a and b are quite close. Therefore this model would suggest that not only b can align to the $\langle 11\bar{2}0 \rangle$-direction of graphene but also a, which is surprising due to the good fit of $b \approx \sqrt{3} \cdot a_{\text{gr}}$ while $a > b$. This results that there could be the possibility for some BL structures that in one layer a, in the other b is orientated to gr or that there are BL structures with a and others with b aligned to gr. Such a model suggests a total of up to 12 different SnSe bilayer stackings: two sets of alignment with the three equivalent gr orientations and two mirror symmetries in c times three orientations of mixed alignment. Since STM is only surface sensitive, other methods are needed to investigate stacking properties. First XRD results reveal that there are six different SnSe bilayer stackings with mixed alignment possible [48].

As a result of an increase in coverage and therefore higher island densities compared to the monolayer growth, the possibility of islands growing together increases significantly. When doing so, there is the possibility of an encounter of islands with a mismatch in orientation. In turn, the islands can not form a continuous lattice, but rather a domain boundary is formed. These are typically at positions inside the islands where an unforeseen shape can be divided into sections. These sections do not have to be in the shape of the equilibrium shape. Note that this phenomenon is to be distinguished from Ir steps, which shine through gr and the islands. Both can be seen by a contrast

change in STM images, like fig. 5.1 (a). In more detail, such a boundary is shown in fig. 5.2 (a), where the boundary is only very vaguely visible and therefore highlighted with dashed lines in the figure. Three different orientations on the surface, similar to the ML experiments, could be observed. Although LEED suggests the possibility of further orientations, this can not be determined or disproven by STM. Since the lattice constants a and b are very close, the differentiation in STM is difficult. Furthermore, no insight into stacking can be gained, as STM is mostly sensitive to the topmost layer. Fig. 5.2 demonstrates one particular domain boundary with two of those orientations. Due to the large aspect ratio between island and substrate and the same difficulty of measurement as mentioned for ML, atomic resolution could only be achieved in Fourier-filtered images, see subfigure (b) and (c). These indicate two differently-orientated rectangular lattices. The moiré superstructure pattern, formed by the lattice constant mismatch of gr and Ir, still shines unaffected through the SnSe islands, despite the increased dimensionality of the bilayers. At a closer look at the boundary, both islands do not grow seamlessly together, but rather form a distinct border, separating both orientations.

For multilayer experiments, it is important to distinguish between the observable coverage Θ and actual total coverage Θ_{total}. STM images result in a two-dimensional interpretation of the surface, where Θ can be easily extracted. With the knowledge of height levels of the structures, total coverage can be extrapolated which in turn approximately correlate with fluence from calibration measurements.
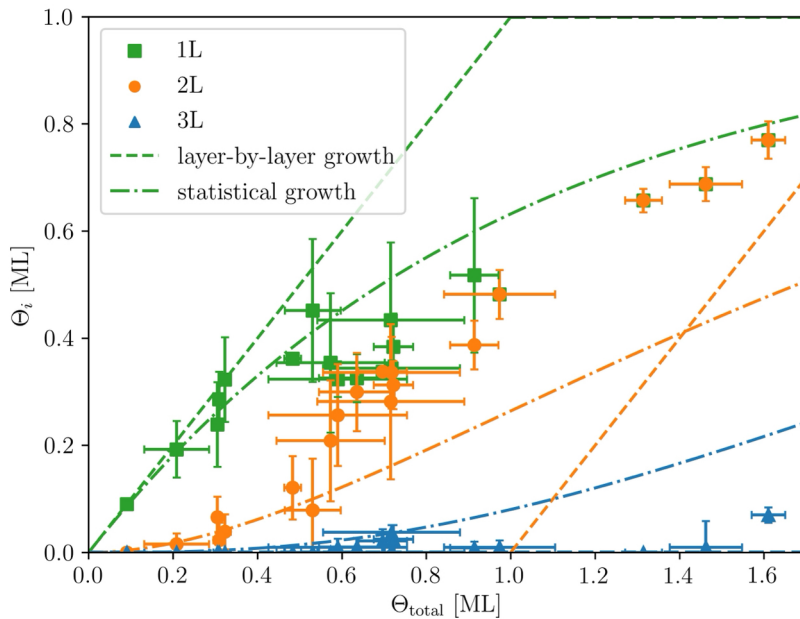

Figure 5.3: Evolution of coverage of individual layers (first layer in green, second in orange, third in blue) with increasing total coverage up to $1.7\,\text{ML}$, which is a nearly fully covered bilayer sample. Plotted together with most common growth theories, layer-by-layer as dashed and statistical in dot-dashed, for each of the layers, colour-coded the same as coverages.

The dependence of the growth of each layer (in terms of coverage) to the total coverage Θ_{total} can give insight into the growth regime behind multilayer formation. In fig. 5.3 the coverage of each individual layer for multiple experiments is displayed against Θ_{total}, where always $\Theta_{\text{total}} = \Theta_{1\text{L}} + \Theta_{2\text{L}} + \Theta_{3\text{L}}$ is true and $\Theta_{i\text{L}}$ is the coverage of the ith layer. Note that $\Theta_{i\,\text{L}}$ is not the observable amount of the ith layer but already takes into

account the interpretation of height. The error of each measurement point results from the standard deviation of multiple images evaluated, which are averaged for the final result. Each data point represents one preparation with the two-step method and is not a sequence of further depositions. It is important to emphasize that the first step is still tuned for ML growth, as discussed in chapter 4. This was checked by STM measurements after the first step. Longer deposition time or higher rates in this step directly lead to bilayer formation. Therefore, the formation of bilayer structures is discussed from the point of monolayer instability. Since the onset of desorption does not start until $\approx 574\,\text{K}$, as discussed in chapter 4, all preparations with a lower annealing temperature were taken into account and treated equally. In the same figure, the two standard growth models are also presented on the same scale. As described in sec 2.1, for layer-by-layer growth the first layer grows linearly with total coverage. Only after one layer is complete, the new one can start to grow. This model is indicated with a dashed line. Statistical growth can be simply explained by the random occurrence of particles on the surface, which are in turn accumulate at said position. This enables early multilayer configurations by chance that a second particle is at the same position. This model is indicated by the dot-dashed line [18]. Each layer is colour-coded: the first layer in green, the second in orange, and the third in blue.

Initially until approximately $\Theta_{\text{total}} = 0.5\,\text{ML}$, first and second layer growth can be described by the statistical growth model, with a nearly linear growth of first layer and an early onset of second layer formation. After roughly $\Theta_{\text{total}} = 0.6\,\text{ML}$, this is no longer true, since the growth of the second layer rises more quickly while the growth of the first layer rather stagnates. This happens up to $\Theta_{\text{total}} = 0.9\,\text{ML}$ since no individual monolayer structure can be identified and mainly bilayer structures exist. In the presented total coverage range, the growth of the third layer is present but majorly suppressed. At even larger total coverage, bilayer growth continues. Arguably, at $\Theta_{\text{total}} = 1.6\,\text{ML}$, where the sample is nearly fully covered with SnSe bilayers, the growth of the third layer starts to become more significant. At this point, it is difficult to distinguish layer thickness with STM since regions with only substrate get sparse and the identification is performed with a height analysis from island to substrate.

Known models of kinetic growth fail to describe this behaviour of transition to bilayer structures. With caution, statistical growth can be used for sections of the total coverage, until approximately $\Theta_{\text{total}} = 0.5\,\text{ML}$. It can be argued that without the carefully chosen first nucleation step to create ML structures, the complete growth for BL would be considered statistical. The preferred formation of the second layer is most likely due to the low step edge energy, such that adatoms can overcome this barrier, and the opportunity to compensate energetic penalties of charge effects of the ferroelectric layer by a second layer in mirrored orientation, as known for antiferroelectrics.

Due to the clear transition from mono- to bilayer islands between 0.6 and 0.9 ML, the study of the size distribution of islands can help to understand this process. The main idea for SnSe could be, that large monolayer islands become energetically unstable due to a too large edge surface. After surpassing a critical size, they collapse to form an energetically favoured bilayer structure. In order to check this theory, islands of different experiments, but in equilibrium shape, are studied for their dimensions. Therefore all islands are of similar rhombic shape consisting of only $\langle 110 \rangle$ edges. As per definition, each side length of this rhombus is equally long and in order to simplify this size analysis, only the side length d is considered. With this simplification, the circumference U of an island can be expressed as $U = 4 \cdot d$ and the area $A = d^2$.

This simplification is here feasible due to the similar geometric form of each island and the large expected effect. For the shape compactification, this was not given.

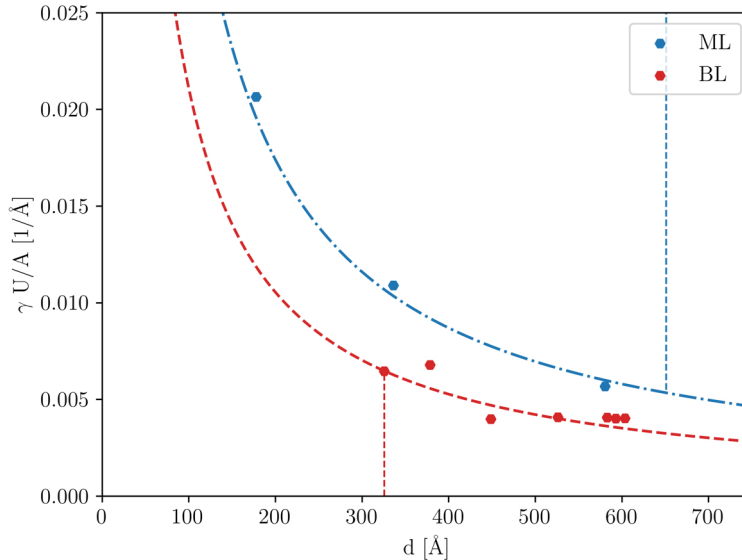In order to compare mono- to bilayer structures, the geometric factor γ needs to be

Figure 5.4: Transition from mono- to bilayer, in blue and red, respectively. Energy factor $\gamma \frac{U}{A}$, consisting of scaling factor γ, circumference U, and area A, in dependence of island length d, with best fit curve as dot-dashed or dashed line. All variables are introduced in the text.

introduced as following:

$$\gamma = \begin{cases} 2 \cdot \left(\sqrt{2} - 1\right) & \text{for ML} \\ 1 - \frac{1}{\sqrt{2}} & \text{for BL.} \end{cases} \tag{5.1.1}$$

The factor γ is needed since area and circumference scale differently for a single or a double layered structure, and is purely based on geometric factors. Note that for bilayers, the circumference is doubled, since each layer has an edge of length d. This results in the parameter $\gamma \frac{U}{A}$ resembling a parameter proportional to energy, which ideally is minimised.

Fig. 5.4 presents this parameter in dependence of island length d. Only islands with ideal rhombic shape, without the close proximity of clusters or any joined second island were investigated, which reduced the sample size significantly. A clear trend between the energy parameter $\gamma \frac{U}{A}$ and island length d can be seen, whereas monolayer islands tend to have generally higher values than bilayer ones. This behaviour is expected since the formation of bilayers should reduce this energy factor. Both follow a trend line proportional to $\propto \gamma/d$, indicated by the dashed and dot-dashed line, respectively. This fit supports the theory for this system, that large monolayer islands tend to become energetically unstable. In order to quantify a critical size, there are two options: the smallest BL or the largest ML island which was observed. Methodically, it is difficult to completely distinguish one singular grown monolayer island from two merged ones, resulting still in a rhombic shape. Therefore, the smallest observable bilayer island was chosen. This argument is possible since the first nucleation step always resulted in ML, otherwise smaller BL islands could be possible. As a result, the smallest bilayer size was found to be $d = 320\,\text{Å}$ and therefore a critical size of ML structure at around $d = 640\,\text{Å}$. Both values are indicated in the figure with vertical dashed lines in the respected colour of ML and BL. The dashed line upwards indicates an upper boundary, while the line downwards indicates a lower boundary. Interestingly this simple model indicates that no energy from this structural change is directly gained, which would reduce the energy factor between crossing points of the two vertical dashed lines with the fit. Since this

energy factor is purely geometrically based, this observation emphasises the presence of rising electric fields with increasing size as another hampering factor of large ML islands.
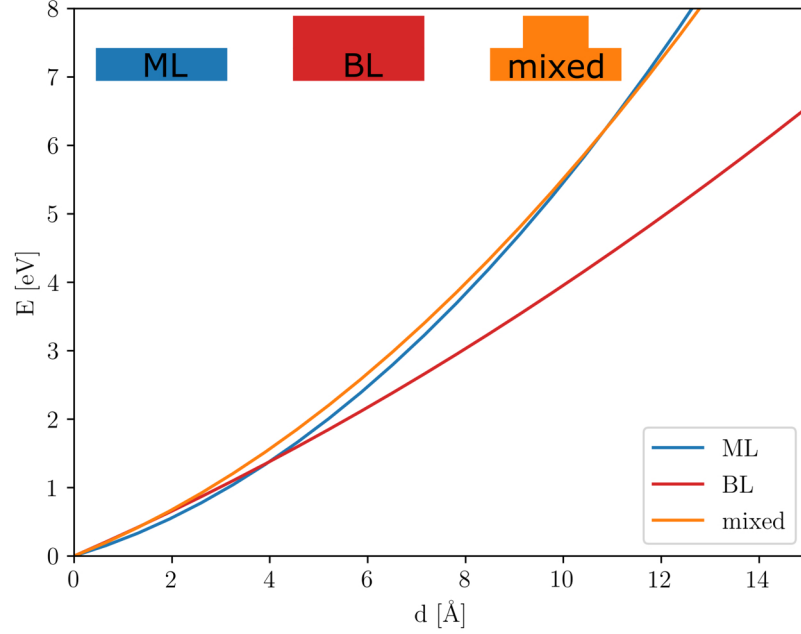

Figure 5.5: Simple formation energy E consideration of different island shapes of identical volume. The parameter d gives the equivalent monolayer side length. For SnSe a mixed stacked island shape (orange, ratio given in text) is always energetically unfavourable, while complete monolayer (blue) and bilayer (red) island preference are size dependent.

This model is based on the observation that only structures with rhombic shape in different defined heights exist and no mixture of underfilled second layer islands, from now on called mixed bilayer. Indeed, no such island with mixed individual layer areas in equilibrium shape could be experimentally observed. Theoretically, this can easily be shown with a consideration of formation energies. In a simple model, the total energy of any island can be estimated by

$$E_{\text{mono}} = \gamma_{001} \cdot d^2 + \gamma_{int} \cdot 0 + 4 \cdot \gamma_{110} \cdot d + \gamma_{gr} \cdot d^2, \tag{5.1.2}$$

$$E_{\text{bi}} = \gamma_{001} \cdot \left(\frac{d}{\sqrt{2}}\right)^2 + \gamma_{int} \cdot \left(\frac{d}{\sqrt{2}}\right)^2 + 4 \cdot \gamma_{110} \cdot \left(\frac{d}{\sqrt{2}} + \frac{d}{\sqrt{2}}\right)$$
$$+ \gamma_{gr} \cdot \left(\frac{d}{\sqrt{2}}\right)^2, \tag{5.1.3}$$

$$E_{\text{mixed}} = \gamma_{001} \cdot b^2 + \gamma_{int} \cdot u^2 + 4 \cdot \gamma_{110} \cdot (u + b) + \gamma_{gr} \cdot b^2, \tag{5.1.4}$$

$$= \gamma_{001} \cdot \left(\frac{1}{\sqrt{\frac{5}{4}}} \cdot d\right)^2 + \gamma_{int} \cdot \left(\frac{1}{\sqrt{5}} \cdot d\right)^2 + 4 \cdot \gamma_{110} \cdot d \cdot \left(\frac{1}{\sqrt{\frac{5}{4}}} + \frac{1}{\sqrt{5}}\right)$$
$$+ \gamma_{gr} \cdot \left(\frac{1}{\sqrt{\frac{5}{4}}} \cdot d\right)^2, \tag{5.1.5}$$

with the parameter d as equivalent monolayer side length, the parameter u is the upper layer, while the parameter b is the bottom layer for the mixed structure. The bottom

layer should have exactly double the length of the top layer, such that $b = 2 \cdot u$. The volume of all islands can be given as $h \cdot d^2$, while h is the monolayer height. The energy coefficients for interface (001), interlayer interaction (int), edge (110), and substrate interaction (gr) are estimated as

$$\gamma_{001} = 16.8 \, \text{meV/Å}^2, \qquad\qquad \gamma_{\text{int}} = 0 \, \text{meV/Å}^2,$$
$$\gamma_{110} = 58 \, \text{meV/Å}, \qquad\qquad \gamma_{\text{gr}} = 16.56 \, \text{meV/Å}^2.$$

These parameters are either from literature and already mentioned in chapter 2 or from the results of the DFT calculations in chapter 4. The interface coefficient γ_{001} scales with the exposed island area under the assumptions that $A = d^2$ as previously considered. The interlayer interaction γ_{int} between SnSe top and bottom layer is difficult to estimate, but set here to zero, in order to underestimate the values of BL and mixed. Step edge energy $\delta_{\langle 110 \rangle}$ is named here γ_{110} for consistency reasons and is the energy per edge. Since BL structures have two layers, there is also more edge contribution to this energy. The parameter γ_{gr} represents the energy to overcome for the exposed gr surface which would have been covered by the island and scales accordingly to the top layer area.

The total energy, estimated by equations (5.1.2)-(5.1.4), of a standard monolayer, a bilayer, and a mixed bilayer island, all with identical volume of $d^2 \cdot h_{\text{ML}}$, whereas bilayer and mixed structure have a height of $2 \cdot h_{\text{ML}}$, is presented in figure 5.5. The mixed structure (orange) is formed with a bottom layer length of double the upper layer length (arbitrarily chosen), whereas the island length of a monolayer (blue) is d, and of a bilayer (red) is $d/\sqrt{2}$. In order to compare these energies, the data is plotted against the equivalent monolayer side length. The total energy of all three structures in dependence of island side length d is visualised in fig. 5.5 with drawings of the models (not true to size). All curves start to increase energy due to increased size. The mixed bilayers always have a higher energy than monolayer structures, whereas at some point bilayers become the most energetically favourable state. Due to this estimation, it is clear that from an energy perspective, mixed bilayer formations are always energetically unfavourable, even with zero interface interaction, which would increase the energy of the mixed islands the most. This explains the preference for clean bilayer structures, without any smaller second layer formation.

It is also notable, that at smaller island sizes monolayer structures are preferred, while at larger side lengths bilayer become more dominant, which fits the narrative of the previous coverage investigation. However, the crossing point at 12 Å does not match with experimental results of a critical size of 640 Å. This gives reason to believe that the growth of bilayers is more kinetically driven than energetically, which is possible due to growth conditions far from equilibrium. Despite the simplicity of this model, it correctly predicts the preference of bilayer structures with increased size and can be used to justify the observation of only pure mono- and bilayers.

5.2 Effect on electronic structure

In order to gain a deeper understanding of the bilayer formation, especially due to its preferred growth in comparison to mono- or trilayer structures, measurements of the electronic landscape can help. It is difficult to compare this system to other materials due to the possible strain difference due to stacking, whose effects have already been studied for example for monolayer SnS [92]. The authors found that tensile strains of $\pm 5\%$ along $\langle 010 \rangle$ are stable and alter the bandgap of this material significantly. Similar effects can play a role here as well, due to the slight but present lattice constant mismatch compared to the ML structure.
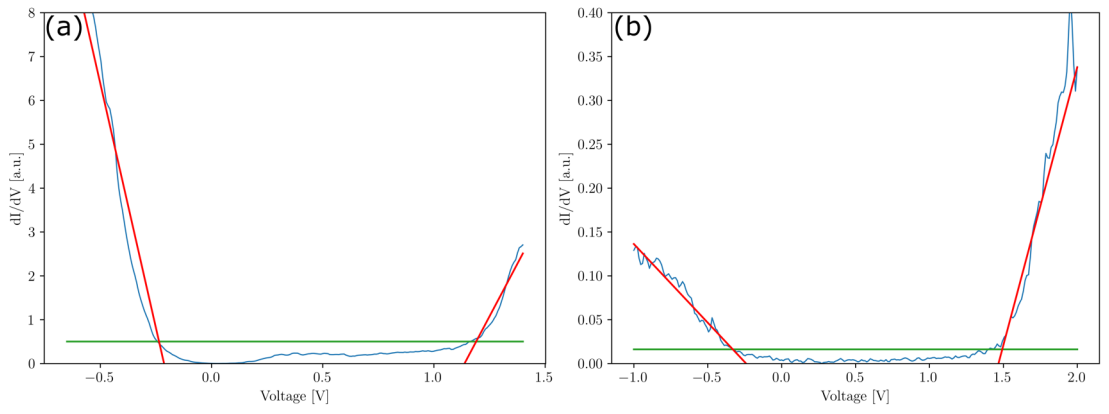
Figure 5.6: STS measurements ($\mathrm{d}I/\mathrm{d}V$) of bilayer SnSe 2D-bulk islands, averaged over multiple spectra, in (a) with a bandgap of $E_\mathrm{G} = 1.455 \pm 0.014\,\mathrm{eV}$ and (b) $E_\mathrm{G} = 1.887 \pm 0.012\,\mathrm{eV}$. The red lines are fitted to the initial slope, the green line represents the error free level at 3σ above the noise level in the gap. STS were measured at tunneling conditions of $(-0.6\,\mathrm{V}, 50\,\mathrm{pA}, T = 120\,\mathrm{K})$ and $(-1\,\mathrm{V}, 50\,\mathrm{pA}, T = 120\,\mathrm{K})$, respectively, and with $V_\mathrm{mod} = 20\,\mathrm{mV}$ and $\nu_\mathrm{mod} = 1337\,\mathrm{Hz}$.

Scanning tunneling spectroscopy of the inner part of multiple BL SnSe islands reveal that two semiconductors with different bandgaps could be detected. Fig. 5.6 shows the averaged $\mathrm{d}I/\mathrm{d}V$ curves of both different bandgaps. The evaluation of these results in $E_\mathrm{G,a} = 1.455 \pm 0.014\,\mathrm{eV}$ and $E_\mathrm{G,b} = 1.887 \pm 0.012\,\mathrm{eV}$. These bandgaps are reduced from monolayer measurements and significantly differ from each other. The reduction of bandgap with increased dimensionality can also be seen in other systems, e.g. phosphorene, where this phenomenon is attributed to more available bands in the system [39]. The observation of two different bandgaps with no structural difference suggests that two phases are present. In imaging, no difference between those two phases could be seen over a range of tunneling conditions, while both have always the same height, appearance, and lattice. Since LEED measurements also indicate different phases due to the splitting of reflexes, a closer look at possible options from theory could give more insight.

Yang *et al.* studied different stacking options of bilayer SnSe and their influence on the band structure [40]. They identified six different possible phases, with two layer orientations to each other, see fig. 5.7 in top- and side-view. The layers can be stacked in the same orientation or rotated by 180°. This is indicated by the nomenclature AA and AB, respectively. The other phases arise from one layer shifted by half a lattice constant in their respective direction. The XX* named phases are shifted along [010]. The XX′ named phases consist of one layer rotated into the [110] orientation.

	AA	AB	AA*	AB*	AA′	AB′
direct band gap at Γ [eV]	2.86	2.07	1.97	2.05	-	1.69

Table 5.1: Band gap values extrapolated from band structure calculation from [40]. There are no data available for AA′.

Table 5.1 summarises the values for the bandgap at the Γ point, which is the value typically seen in measurements, as already demonstrated for ML SnSe. The values are based on the calculated band structures as reported in [40]. Unfortunately, none of these values at the Γ point can be attributed to the results from the STS measurements. Most theoretical bandgap values are too large for the observed structures. The argument of additional strain would only increase the given values for bandgaps and is therefore not
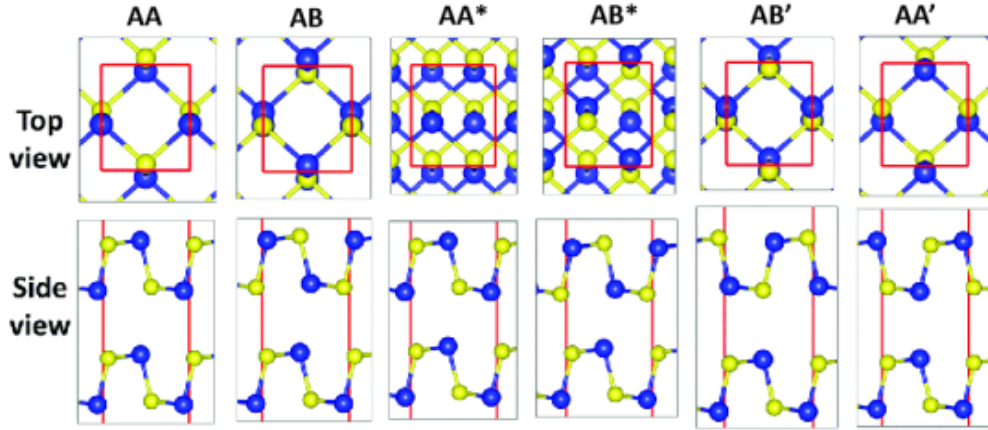
Figure 5.7: Stacking options of orthorhombic MX bilayer lattices as present for SnSe, adapted from [40]. Lattices are presented in a top and side view, whereas Sn atoms are blue and Se are yellow. The unit cell is drawn in the top view. The stacking conditions in one direction are indicated by the parallel lines in the side view, while AA and AB differentiate due to one mirrored layer. The other direction is indicated by the sketch in the top view.
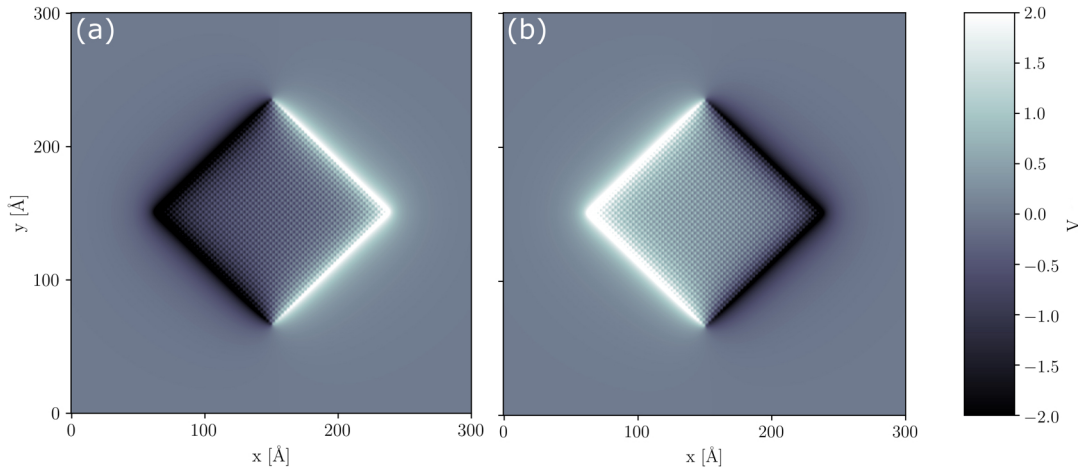
valid.

Figure 5.8: Potential calculation of bilayer SnSe islands consisting of 12800 atoms each, shaped only by $\langle 110 \rangle$ edges, for the phases (a) AA and (b) AB, where only the top layer is rotated. The reference layer is chosen in the bottom layer. Both resulting potentials are mirror images of each other.

In order to differentiate the two bilayer orientations AA and AB, potential calculations are performed. Fig. 5.8 presents two islands consisting each of 12800 atoms arranged in a bilayer formation. Both share the same bottom layer and are only differentiated by a rotated top layer to form the phases AA and AB as shown in subfigures (a) and (b), respectively. Both exhibit very similar behaviour, such that two neighbouring sides of the edges are on positive, the other on negative potential. In the interior of the islands, the potential is attenuated with a periodic pattern due to the positions of the topmost atoms. Both phases differ only in the orientation of the charged edges. They are mirror images of each other. From this simple calculation follows, that in electronic measurements of the surface, those two phases should have distinctive properties. Unfortunately, this is

not distinguishable from the ferroelectric switching mechanism, which reorientates the electric potential. Generally, this finding is in line with reported characteristics of bulk MoS_2, where the surface can effectively be treated as an isolated quasi-freestanding monolayer [93]. Due to a higher response in STS, spectroscopy maps are technically feasible and should demonstrate this insight.
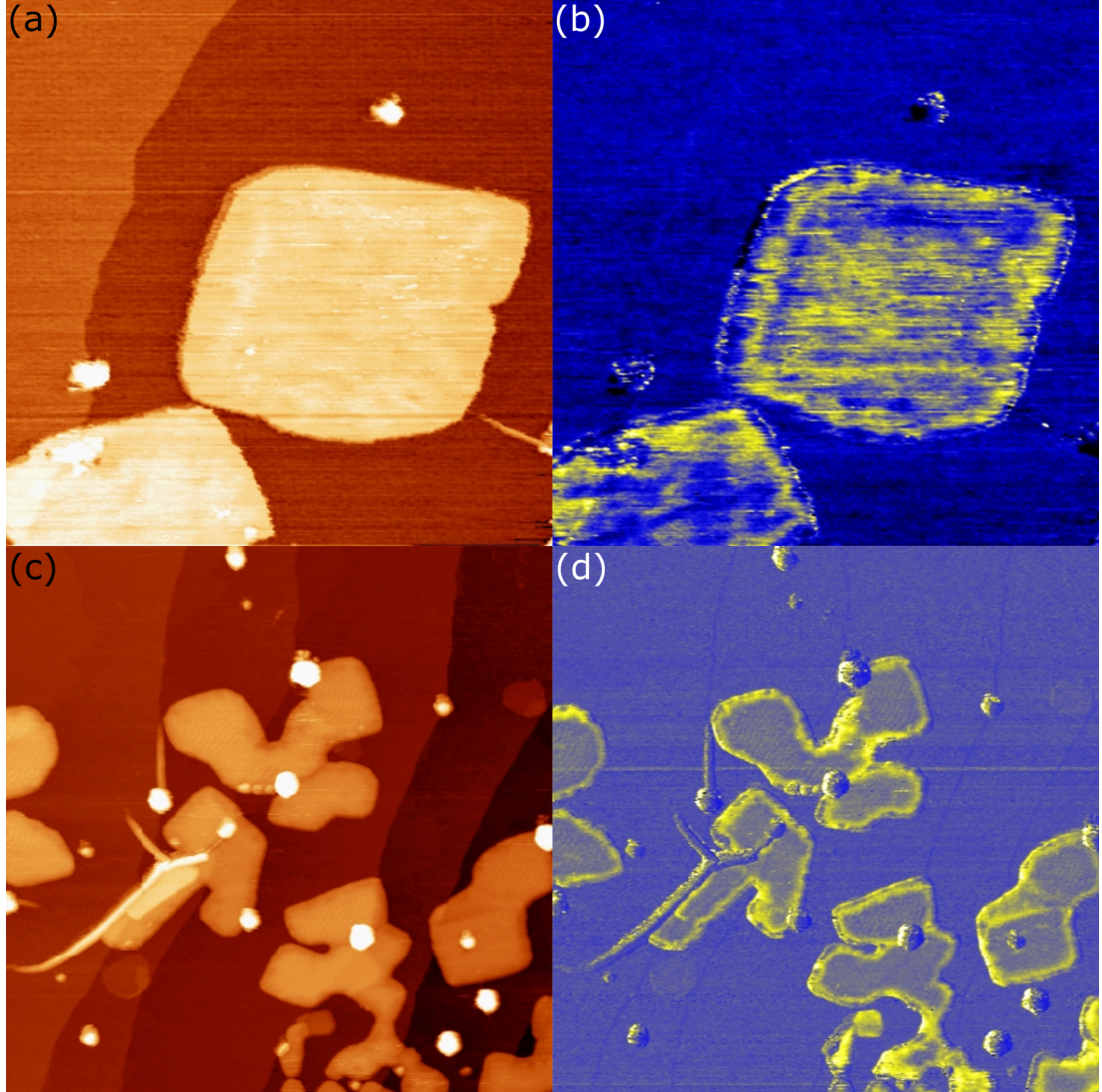

Figure 5.9: STM images and STS maps of slightly different SnSe bilayer structures: (a) STM image, grown at $(5.2 \times 10^{-3}\,\mathrm{ML/s},\ 15\,\mathrm{s},\ \mathrm{RT})$ and subsequently $(1.72 \times 10^{-3}\,\mathrm{ML/s},\ 1200\,\mathrm{s},\ 570\,\mathrm{K})$, $(1\,500\,\mathrm{\AA} \times 1\,500\,\mathrm{\AA},\ -0.3\,\mathrm{V},\ 300\,\mathrm{pA},\ T = 120\,\mathrm{K})$ with (b) corresponding map. (c) STM image, grown at $(5.2 \times 10^{-3}\,\mathrm{ML/s},\ 30\,\mathrm{s},\ \mathrm{RT})$ and subsequently $(1.72 \times 10^{-3}\,\mathrm{ML/s},\ 1200\,\mathrm{s},\ 567\,\mathrm{K})$, $(4\,000\,\mathrm{\AA} \times 4\,000\,\mathrm{\AA},\ -0.4\,\mathrm{V},\ 100\,\mathrm{pA},\ T = 120\,\mathrm{K})$ with corresponding map in (d). STS maps were measured with $V_{\mathrm{mod}} = 20\,\mathrm{mV}$ and $\nu_{\mathrm{mod}} = 1337\,\mathrm{Hz}$.

In order to investigate the potential at the edges in STM, the option of constant height STS maps at one bias voltage is used. It is performed for two different preparations with slightly different island shapes and can be seen in fig. 5.9. While (a) and (c) are topography images, (b) and (d) are the corresponding maps, measured simultaneously with the lock-in method, mentioned in sec. 3.4.

While the difference in the growth parameters between those two preparations is marginal, the shapes differ significantly. In subfigure (a) the islands resemble nearly

the equilibrium shape and are relatively separated from each other. However, the islands in subfigure (c) have quite straight edges, but each formation has an irregular shape. This shape can be described as clusters of multiple conjoined islands, where each island individually considered is close to the equilibrium shape. This difference in structure does not occur due to a kinetic reason, since the annealing temperatures of both preparations are very close. The larger initial coverage after the first step for the preparation in subfigure (c) results in less separated nucleation spots, such that islands need to form clusters of conjoined islands. This is an example for the complexity of the growth in this system.

The measurement of STS maps pronounces differences in the electronic structure in the interval around the bias voltage and the added modulation voltage. Therefore, any elevation changes, such as Ir steps, are only barely visible in these kind of images. The islands in both preparations exhibit similar electronic behaviour. The entire edge of each individual island expresses a charge effect compared to the interior of the islands. The separation of edge effect and the interior is more pronounced in the islands that are conjoined, most likely due to the slight difference in bias voltage. The slightly more negative bias voltage can shift the measurement more to the steep increase in DOS, resulting in a stronger signal in this measurement. This behaviour could also be seen at different (positive) bias voltages and is only demonstrated here for the negative branch. The measurement method strongly increases the visibility of the previously mentioned domain boundaries.

In the islands from subfigure (c), a substructure in the interior of the islands can be seen, which resembles a bend stripe pattern. This pattern has a lateral spacing of roughly $2 \times a_{\mathrm{gr}}$. This could be explained by the introduction of intercalation. Other studies also see an enhanced preference for grown-together islands when intercalation is present [45]. This intercalation is probably introduced during the longer nucleation phase in this preparation. Due to the layered system, there are many options for intercalation, most likely in the plane between Ir and gr or gr and the bottom layer SnSe, but any distinct statement is difficult.

In comparison to the simple theoretical model of the electric potential, there is no separation of charges in the islands from experiment. One possible explanation for this deviation from the theoretical idea could be the occurrence of edge relaxation and/or reconstruction. Due to the increased dimensionality of bilayers, there are more degrees of freedom and therefore also a greater possibility for such mechanisms. For the isostructural phosphorene, reports state several different bilayer reconstructions that can occur in various conditions [72]. Due to the complexity and total size of this system, any theoretical approach to calculate edge reconstructions/relaxations is directly associated with great computational effort.

Chapter 6

Germanium Selenide

Germanium selenide (GeSe) became important early on as a van der Waals semiconductor with a suitable bandgap ($\approx$ 1.2 eV) for various applications [94], and its excellent thermoelectric properties [95]. Beyond that monolayer structures are theoretically predicted to be ferroelectric which enables another important field for sensing and devices. Theory gives insight into five different polymorphs, see sec. 2.4, out of which two should be ferroelectric [35]. This wide variety of phase space gives an opportunity for new studies. The growth of well-defined two-dimensional ferroelectric islands is still rather scarce in literature and no MBE-grown GeSe monolayer could yet be achieved. This chapter will cover the evaporation of GeSe dimers from powder and the resulting amorphous clusters on gr on different substrates (sec. 6.1). Furthermore, the growth and first characterization of the experimentally new β-phase will be covered in sec. 6.2. Although clear naming schemes for the standard in-plane ferroelectric α-phase is used, other phases are not clearly defined. In this work, the convention introduced by Zhang *et al.* is used [35].

The experimental data of sec. 6.2. were obtained in cooperation with V. Blecker [58] and with further knowledge analysed here.

6.1 Amorphous GeSe

A similar setup, evaporation out of an effusion cell from powder, as presented in fig. 3.10 is also used for GeSe (AKos Consulting & Solutions GmbH, 5N).

In order to describe the evaporation of GeSe, deposition rates are measured by a QMB. The evaporated material is investigated for its composition by QMS, both shown in fig. 6.1. The onset of evaporation can be seen at 520 K with a typical exponential behaviour in temperature (indicated by fit). The temperature error is given by the error of the used pyrometer. The onset of GeSe evaporation can also be observed in QMS measurements, with peaks at around 152 amu starting to appear. Earlier evaporation of pure Se and Ge could also be detected but did not result in a measurable amount in QMB. Those could occur due to dimers being separated in QMS itself or naturally during the evaporation process. The reason for this early onset of individual peaks is more likely due to low vapour pressures compared to the dimer itself. The accumulation of peaks around the main peak at 152 amu can be explained by the isotope composition. Since the results from QMS measurements can be ambiguous, the isotope composition can confirm the affiliation to GeSe. For this, the ratio of two QMS peaks is compared to the ratios of the theoretical isotope occurrence of the corresponding masses, calculated by the superposition of the individual elements. This method confirms that these peaks stem from GeSe. In the shown spectra peaks at around 110 amu and 180 amu can be seen, which are also present at RT, and therefore can be considered as background noise.
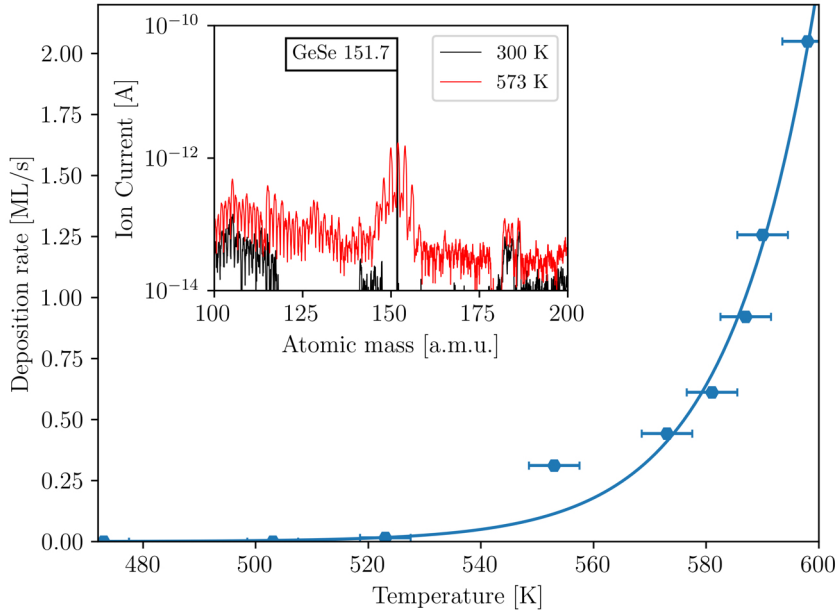
Figure 6.1: Evaporation of GeSe. Deposition rate in dependence of evaporator temperature with an exponential fit is measured by QCM. The inset represents the molecular composition at $300\,K$ and $573\,K$, measured by QMS, indicating the evaporation of dimers.

The peaks corresponding to Ge, Se, and GeSe coexist in a wide temperature range. Therefore it is important to optimise the temperature for maximising the GeSe peak, regardless if the Ge and Se peaks are stemming from ionisation in QMS or are actually due to changes in the evaporation material. It is important to note that the phase diagram sets a hard upper limit of usable evaporation temperatures [96]. At high temperatures the most stable configuration tends to gravitate more to $GeSe_2$, resulting in a shorter usable duration of the evaporation material before renewal is necessary for higher evaporation temperatures [96]. This feature opens up the parameter space for crystallisation since temperature is now not only controlling rate but also the possible chemical composition. Rate can also be varied by the distance between evaporator and sample.

Multiple crystallisation experiments via evaporation of GeSe on gr/Ir(111) were performed. In order to induce crystallisation multiple parameters were varied individually. Evaporation rates were varied from $0.01\,ML/s$ up to $2\,ML/s$ and mostly independent of that, evaporator temperatures from $563\,K$ up to $773\,K$ to introduce different possible atomic compositions. Coverage was varied between $0.12\,ML$ up to multiple ML, and annealing temperatures up to $617\,K$, at which the material completely desorbed from the surface. The annealing was performed both, during and after evaporation. In the case of post annealing, it was performed with and without Ar background pressure up to $1 \times 10^{-4}\,mbar$. No additional reflexes to the gr/Ir(111) spots in LEED could be found, see inset of fig. 6.2 (a) and (b), resulting in GeSe not forming crystalline films on gr/Ir(111). However, different amorphous structures could be observed. Two widely differently shaped structures can be seen in the STM images in the main frame of the figure. The preparation in (a) is grown with subsequent annealing and in (b) with annealing during deposition. In both cases, clusters of material, possibly GeSe, are observed on the fully enclosed gr surface. The moiré superstructure of gr is still present and slightly visible, which is supported by LEED measurements where the gr and Ir reflexes are present. The preparations also result in similar observable coverage
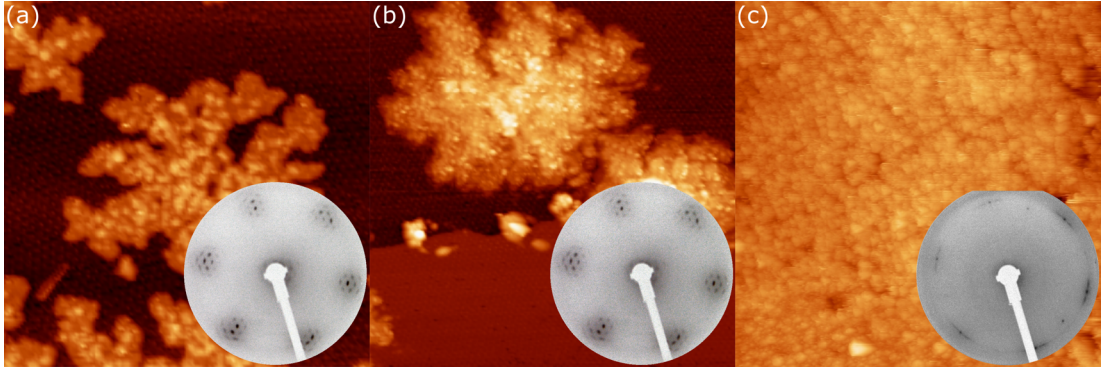
Figure 6.2: STM images of GeSe on various gr samples; grown at (a) (643 K, 2 ML/s, 10 s, RT) with subsequent annealing at 561 K on Ir(111), resulting in a coverage of $\Theta = 0.30$ ML, (1 000 Å × 1 000 Å, 1 V, 5 pA), and (b) (643 K, 2 ML/s, 10 s, hot sample of 561 K) on Ir(111), resulting $\Theta = 0.36$ ML, (1 500 Å × 1 500 Å, 2 V, 5 pA), each with LEED measured at 75 eV inset. The preparation in (c) is at (623 K, 1.8 ML/s, 10 s, RT) on Pt(111), (4 000 Å × 4 000 Å, 1 V, 5 pA), with LEED inset at 72 eV.

Θ. Note that the rates measured by QMB overestimate the resulting coverage, due to possible desorption during annealing. Both shapes can be described as fractal-dendritic. However, the agglomeration of atoms differ in terms of lateral and vertical growth. Both preparations result in islands with no clear height, with the maximum still below 20 Å. The islands with evaporation on a hot sample (as shown in (b)) tend to prefer vertical growth. This leads to the understanding that vertical amorphous growth on gr/Ir(111) is generally preferred, which could be limited by depositing at low temperatures, while crystallisation would be needed to be induced afterwards. The study of such films in STM is challenging. Due to very low interaction with the substrate and the material cluster itself, the imaging process requires very low tunneling currents and high bias voltages.

When the underlying metallic substrate was replaced with a different platinum-group metal, as shown exemplary for Pt(111) in fig. 6.2 (c), no significant difference could be observed. The preparation of such a surface is identical to Ir(111). The gr layer here is predominated by *R30°*-rotated and other orientation of gr, leading to the ring-like structure with reflexes between the Pt spots in LEED. The example here shows a high coverage (> 1 ML) preparation. Crystalline structures could not be identified in STM images. LEED also does not show any new reflection spots. All this leads to the presumption that crystallization of GeSe on gr on platinum-group metals is not feasible in this setup.

After growth at lower rates, very large expanding and flat structures could be observed, see fig. 6.3. This preparation leads to large structures, very widely separated with regions of no or amorphous clusters as described earlier. These structures differ from those previously described in having a distinct height of 1.9 Å and creating long straight edges. The edges form either triangular or hexagonal shapes, which can be seen in either island shape or in larger holes within the island. At the edges, a similar structure to the previously described amorphous dendritic islands can be observed. Larger agglomerations tend to grow outwards, while they also coexist separately in close proximity, as shown in subfigure (a). Due to post-annealing, defects in the gr layer are introduced, primarily next to the islands, which can be seen due to the lifted moiré superstructure and can typically be attributed to intercalation [77–79]. Such a region can be seen in subfigure (a) with a pattern resembling stripes below the island. Still, no LEED spots, either from those flat islands or the intercalation could be observed. Although
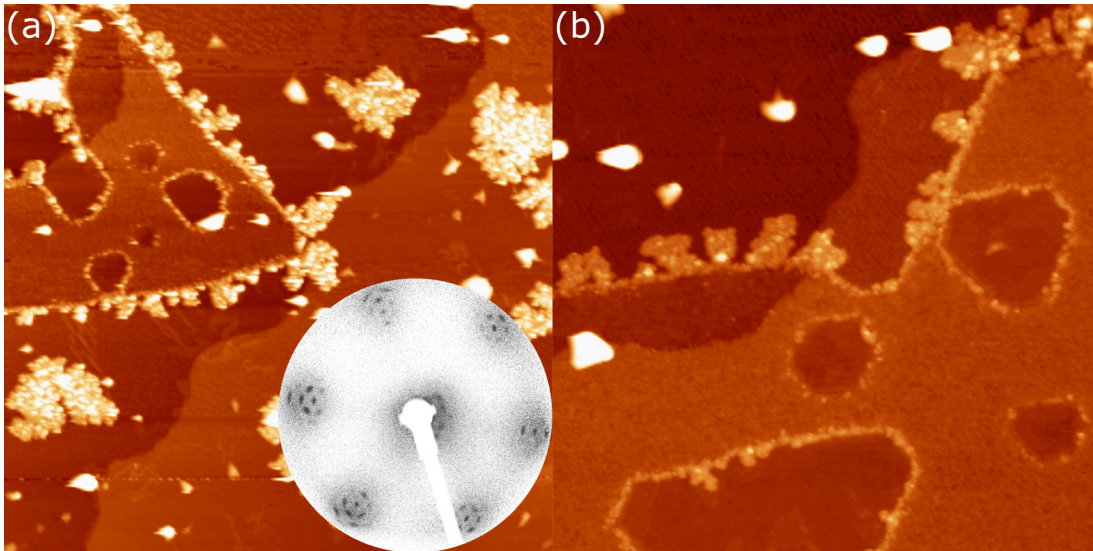
Figure 6.3: Flat, glass-like, GeSe structures on gr/Ir(111), grown at (563 K, 2.0 × 10^{-2} ML/s, 300 s, RT) with subsequent annealing at 530 K: (a) STM images measured at (4 000 Å × 4 000 Å, 3 V, 5 pA) with LEED inset at 65 eV; and (b) (4 000 Å × 4 000 Å, 1.5 V, 5 pA.)

geometrically formed islands are an indication of crystallinity, LEED measurements reflect that the flat islands are also amorphous. One possibility here would be the creation of 2D GeSe glass. Glass-like structures are a specific type of amorphous film. While any amorphous formation does not have a regular and repeating atomic structure, amorphous solids that exhibit a glass transition are called a glass. Glass can be described as a disordered arrangement of atoms with short-range order. The glass state is not in thermodynamic equilibrium. Monochalcogenide glasses have already been studied in terms of bulk optical applications [97].

Due to limited technical possibilities in those regards, such as XPS or Raman measurements, and since these preparations are not stable in ambient conditions, this glass structure is meant for future investigation.

6.2   β-GeSe

The benefit of studying materials with nearly no substrate interaction, as with gr on metallic substrates, is that a quasi-freestanding structure can be investigated. But there are also other suitable substrates. In order to gain further information about possible crystallisation preferences and different growth processes, several substrate options, like gr/Ir(111), gr/Pt(111), and Au(111), were tested. This experiment was performed in an encapsulated environment in the group of Schmedt auf der Günne. Each crystal was separately encapsulated with some GeSe powder at a pressure 1 bar of N_2 in glass tube. After 60 min at 530 K in a furnace, it led to no crystallisation for the gr surfaces under these conditions, but a crystalline film on the gold surface could be observed due to reflexes in LEED (not shown). Here is the possibility that the reactive Au(111) surface acts as a catalyst or that the different lattice offers a better agreement with GeSe. This is seen as motivation to study the growth of GeSe on Au(111) via MBE in UHV.

Similar to the deposition of GeSe on gr, no reflexes in LEED could be observed for the deposition on Au(111) at room temperature. But during annealing at elevated sample temperatures (≈ 550 K), crystallisation takes place. The same behaviour could also be found for deposition on a hot sample. The structure after crystallisation
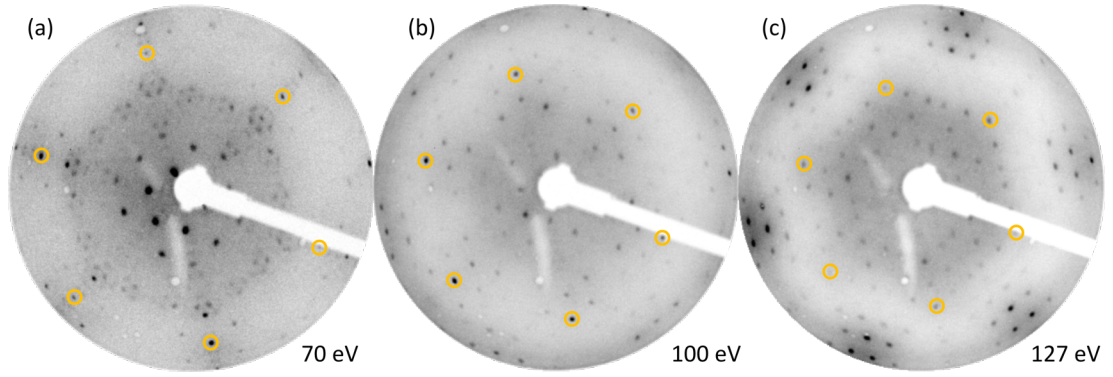
Figure 6.4: LEED images after GeSe deposition at ($623\,\mathrm{K}$, $3.0 \times 10^{-2}\,\mathrm{ML/s}$, $1200\,\mathrm{s}$, $553\,\mathrm{K}$) on Au(111) for different energies, given at bottom right corner. Au-reflexes are highlighted in yellow.

can be seen in LEED images at different energies, as shown in fig. 6.4 after $623\,\mathrm{K}$, $3.0 \times 10^{-2}\,\mathrm{ML/s}$, $1200\,\mathrm{s}$ deposition at a sample temperature of $553\,\mathrm{K}$. Note that this annealing temperature is already surpassing the temperature where GeSe desorption took place for gr/Ir(111), indicating a different interaction between layer and substrate. In subfigure (a) the diffraction pattern at $70\,\mathrm{eV}$ can be seen. In yellow the first-order Au(111) reflexes are marked. Just around them, the six herringbone reconstruction reflexes are slightly visible, not to be mistaken with the six larger spots around the Au(111), which are part of the complex GeSe diffraction pattern.

Generally, the main pattern can be described as $\left(\frac{5}{4} \times \frac{5}{4}\right)$ in Wood notation, which results in four reflexes in between each Au spot and continuing the pattern in all three symmetry directions of the gold. Notably, not all of the GeSe reflexes have the same intensity, some are even completely missing from the ideal $\left(\frac{5}{4} \times \frac{5}{4}\right)$ pattern. This is mostly due to the structure factor. Additionally, at low energies (subfigure (a)) each spot is surrounded by six reflexes in the size of the herringbone reconstruction. These finer spots are dampened for inner main reflexes. As discussed in sec. 3.1. diffraction energies are directly linked to the inelastic mean free path, meaning that here the lower energies in subfigure (a) are more surface sensitive than the higher ones. The complex LEED pattern and the energy-dependent behaviour indicate a complex surface. Just from LEED a thin film ($< 5\,\mathrm{ML}$) can be assumed, since the Au(111) spots including the herringbone reconstruction can be seen.

As the energy increases, the first-order Au(111) reflexes get further to the center, since the wavelength is increased, and the herringbone reflexes are no longer visible. In subfigure (b) the diffraction pattern at $100\,\mathrm{eV}$ of the sample can be seen. The main pattern with $\left(\frac{5}{4} \times \frac{5}{4}\right)$ and its exceptions are still present, but the finer structure around each spot completely vanishes. At even higher energies, as seen for $127\,\mathrm{eV}$ in subfigure (c), where the (11)- and even slightly the second-order spots of Au(111) can be identified, the $\left(\frac{5}{4} \times \frac{5}{4}\right)$-pattern is manifesting and even the previously missing reflexes start to appear more clearly. Therefore this main pattern can be attributed to the 2D bulk diffraction pattern of this GeSe phase.

Since the main pattern can be directly described by the $\left(\frac{5}{4} \times \frac{5}{4}\right)$ Wood notation, the mismatch between Au and GeSe can also be described as commensurate. This leads to GeSe also having a hexagonal pattern like Au(111). The periodicity can be explained as a 4×4 cell of GeSe, which is equivalent to a 5×5 cell of Au. The lattice constant of
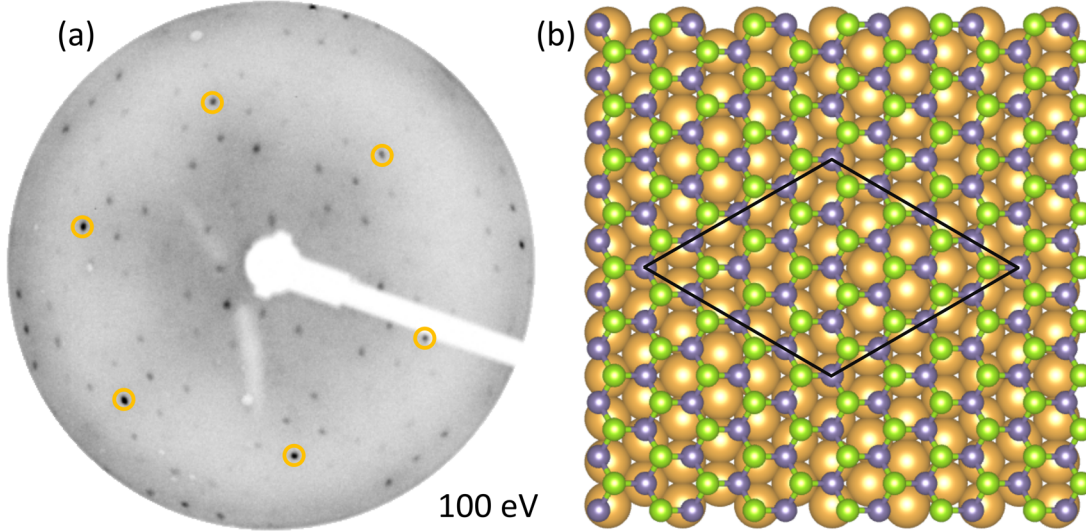
Figure 6.5: LEED image (a) of β-GeSe/Au(111), already seen in fig. 6.4, with (b) model of the GeSe structure on top of the Au(111) lattice (yellow). The side view is presented to the right-hand side. The hexagonal GeSe layer is represented by purple Ge and green Se balls. The superstructure unit cell is highlighted in black.

GeSe can then be directly calculated from the Au(111) lattice constant a_{Au} [21] as

$$a_{\text{GeSe}} = a_{\text{Au}} \cdot \frac{5}{4} = 2.885\,\text{Å} \cdot \frac{5}{4} = 3.606\,\text{Å}. \tag{6.2.1}$$

This is visualised in fig. 6.5. Subfigure (a) is the LEED image already seen in fig. 6.4, showing the hexagonal pattern of Au(111) and the commensurate $\left(\frac{5}{4} \times \frac{5}{4}\right)$ GeSe main pattern. Directly next to a real-space model in (b), made with the program VESTA [98], where Ge is purple and Se is green. The top as well as the side view (right-hand side) is shown. The supercell of the main pattern is drawn in black. This directly demonstrates that the lattice constant of GeSe is slightly larger than the one of Au(111), while having the same orientation, resulting in a supercell where Ge and Au only have the same position to each other after four lattice constants a_{GeSe}. Note that, the GeSe lattice is slightly buckled, resulting in one atom sort being closer to the Au surface than the other, see the side view in fig. 6.5 (b). In an analogous argumentation, already discussed for SnSe/gr/Ir(111) in sec. 4.2., Frezza *et al.* state for hexagonal SnSe/Au(111) that Sn atoms are closer to the Au(111) surface [81]. Since GeSe is structurally very similar to SnSe, the idea is that also here the metal atoms, therefore Ge, are closer to the surface. For that reason, the model is constructed such that a Ge atom (top of supercell) is positioned directly on top of one Au(111) atom and the supercell is drawn for this atom type.

The hexagonal phase of GeSe has already been described theoretically in many studies [35, 99, 100]. As there is no consensus in naming the hexagonal phase, contrary to α for the orthorhombic phase, the nomenclature of the hexagonal phase as β-GeSe is chosen, based on the work from Zhang et al. [35]. Further insight into the phase space of MX is given in sec 2.4.

Literature already provides the theoretically optimised geometric structures, lattice constants, bandgaps, and STM simulations for the β-phase [35, 100]. Fig. 6.6 shows in (a) the top and side view of the hexagonal structure with a lattice constant of 3.63 Å, bond length of 2.53 Å, and a layer height of 1.41 Å. Due to the buckling, the bond angles differ from the ideal hexagonal lattice. In subfigure (b) STM simulations at a
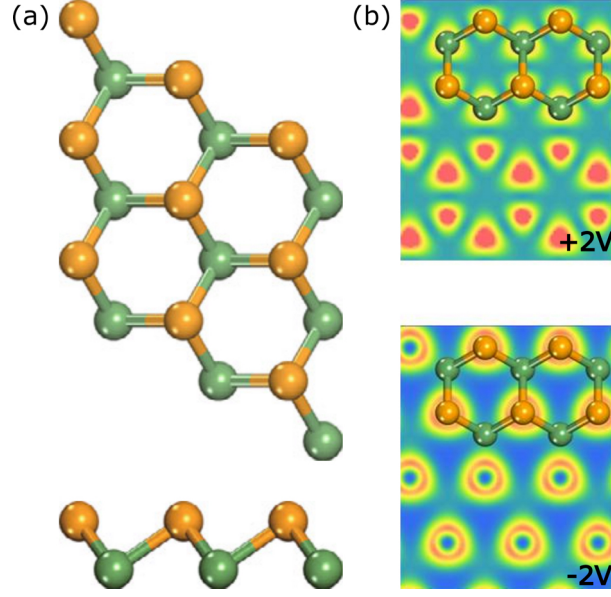
Figure 6.6: (a) Atomic structure of the optimised geometry of β-GeSe in the top (top) and side view (bottom), with Ge and Se as green and yellow balls, respectively. Lattice constants of the hexagonal unit cell lead to $a = b = 3.63\,\text{Å}$ with an layer height of $h = 1.41\,\text{Å}$. In (b) simulated STM images at a bias voltage of $\pm 2\,\text{V}$; adapted from [35].

bias voltage of $\pm 2\,\text{V}$ indicate either a hexagonal or a triangular pattern.

The lattice constant of $3.61\,\text{Å}$ is in good agreement with theory. In a similar argumentation to the α-phase, a clear indication of out-of-plane ferroelectricity can be seen from the lattice structure. The buckled lattice with one atom sort always in a different z-plane than the other enables a dipole moment to arise across the whole structure. This is also confirmed by the theoretical reports of Liu et al. with a predicted polarisation of $6.48 \cdot 10^{-12}\,\text{C/m}$ and a strong dependency on strain and doping [100].

LEED measurement suggest that there is no change in the diffraction pattern for a calculated coverage over $\approx 1\,\text{ML}$. This behaviour is also quantified by measuring LEED intensities over a large range of deposited material, characterised by fluence, the product of rate and deposition time. This can be seen in fig. 6.7, where the spot intensity ratio is plotted against fluence. The intensity of one individual spot is defined by its greyscale values summed up over the accumulated area. Only the GeSe reflex closest (on the radial axis further in) to a Au(111) reflex was used because of the fluctuation of intensity of the GeSe pattern. In order to take different screen brightnesses and possible distortion errors into account, the values are normalised by the intensity of the Au spot closest to the GeSe reflex. This can be seen as stable over different film thicknesses, since for monolayer growth the intensity will not change significantly. Therefore, this normalisation factor does not alter and the ratio I_{GeSe}/I_{Au} gained from greyscale values is directly proportional to I_{GeSe}. This data can be seen in fig. 6.7. While the error for the intensity ratio is due to statistics, the error for fluence is the combination of the rate error of the used QMB and a fixed error of $\pm 1\,\text{s}$ for deposition time. This observation leads to the idea that the growth of β-GeSe is self-limited and no growth on GeSe itself takes place. In other words the formation of a second layer is not possible. Such a model can be described by a sigmoid curve, which is fitted in the form of

$$I_{GeSe}/I_{Au} = S \cdot \left(1 - e^{-R \cdot t}\right), \tag{6.2.2}$$

where R is the rate, t is the deposition time, and S is a fitting parameter. The fit is in good agreement with experimental data and reveals the parameter $S = 0.320$ and
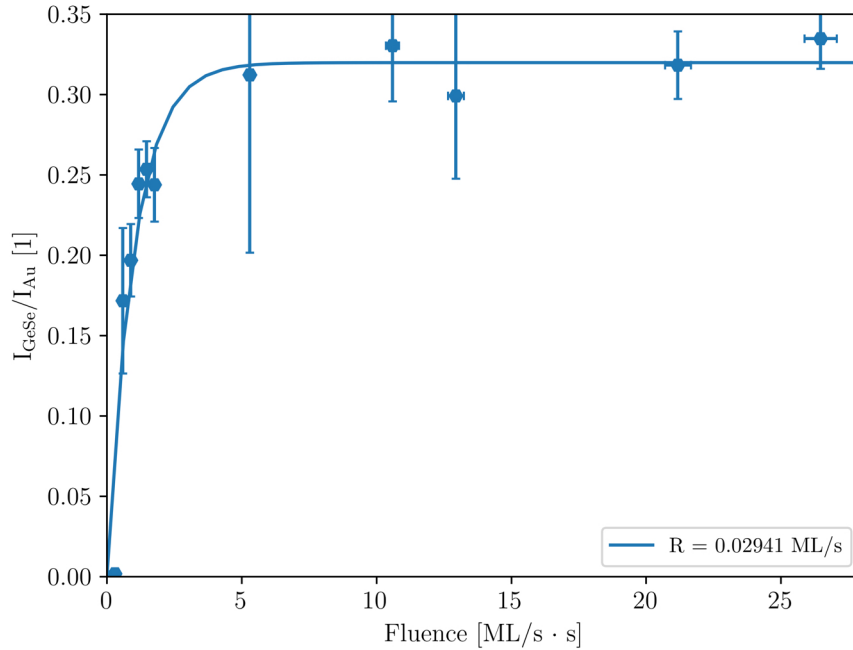
Figure 6.7: Spot intensity ratio I_{GeSe}/I_{Au} in dependence of fluence fit self-limiting growth. Data points were determined by image intensities for Au and the GeSe closest to the Au reflex, averaged for all directions, for images measured at 100 eV. Fluence is the product of rate and deposition time.

$R = 0.029$ ML/s. The rate R is in good agreement with measurements from QMB, which highlights its importance. The value S is the intensity ratio I_{GeSe}/I_{Au} for exactly 1 ML, therefore any intensity ratio can be linearly converted into coverage.
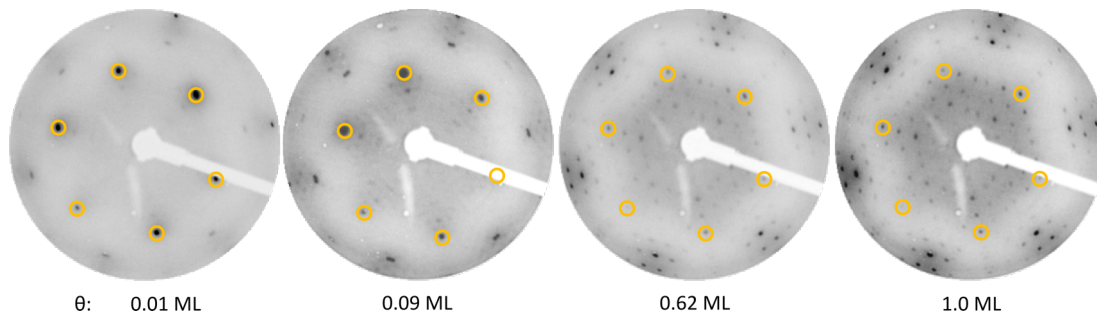

Figure 6.8: Different preparations of β-GeSe sorted by coverage, given at the bottom of each image. Fluence ranged up to 60 ML/s · s, while sample/annealing temperatures are within 550 ± 40 K. All LEED images are taken at 127 eV.

With this knowledge, different preparations can be characterised by coverage, independently from fluence and annealing temperatures. This can be seen for multiple (sub-)monolayer coverage of β-GeSe/Au(111) in fig. 6.8 at a LEED energy of 127 eV. At 1 ML the result is similar to fig. 6.4 (c). Down to 0.62 ML the LEED pattern itself does not change, but the intensity of GeSe reflexes is strongly reduced. At very low coverage, as seen for 0.01 ML, which is the lowest possible for this LEED instrument, and more clearly 0.09 ML, a splitting of the GeSe reflexes can be observed. This effect is most noticeable at the (11)-reflex. This splitting does not change lattice constants but alters the angular alignment between GeSe and the substrate. In fig. 6.5, the alignment angle is zero. The splitting changes this to $+1°$ and $-1°$. Apparently, this alignment allows a

preferred stacking of the hexagonal layer on Au(111), which is energetically no longer favourable at higher coverage. This onset could be found for 0.5 ML.
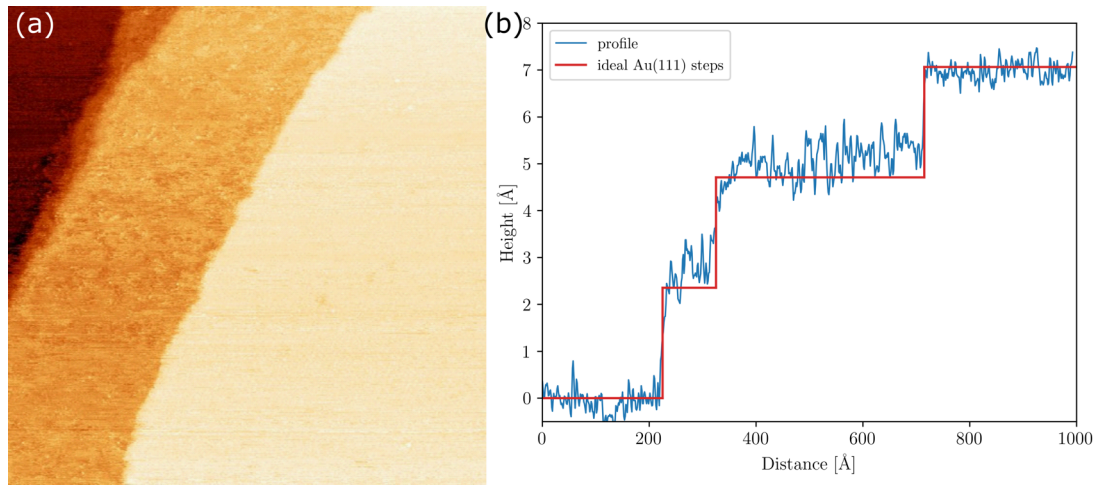

Figure 6.9: (a) Large overview STM image of GeSe/Au(111), grown at $(623\,\text{K}, 3.0 \times 10^{-2}\,\text{ML/s}, 600\,\text{s}, 553\,\text{K})$, $(1\,000\,\text{Å} \times 1\,000\,\text{Å}, -0.2\,\text{V}, 50\,\text{pA}, T = 200\,\text{K})$, with (b) corresponding line profile in scan direction. The step height of the sample (blue) fits the ideal Au(111) step height (red).

Fig. 6.9 (a) shows an STM overview image of a fully covered GeSe on Au(111) surface with a fluence of 18 ML. The surface of GeSe on Au(111) does not show any islands or any signs of an incomplete layer, confirming the model of self-limited growth. Both observations, together with the LEED results, lead to the understanding that β-GeSe growth is only possible on the reactive Au(111) surface, not on the material itself.

The steps which could be seen in STM fit nicely to the height of ideal gold steps. This is visualised in subfigure (b) with a line profile across the whole image together with the ideal Au(111) step height in red.
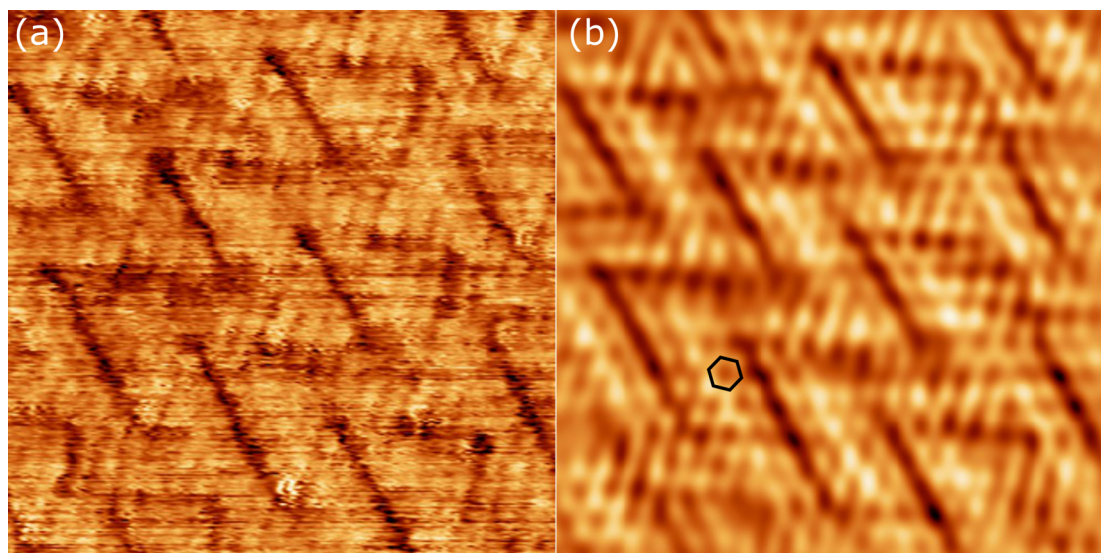
Figure 6.10: Detailed STM image of GeSe/Au(111), grown at $(623\,\text{K}, 3.0 \times 10^{-2}\,\text{ML/s}, 600\,\text{s}, 553\,\text{K})$, $(100\,\text{Å} \times 100\,\text{Å}, -0.05\,\text{V}, 300\,\text{pA}, T = 200\,\text{K})$. In (a) unfiltered, while (b) is Fourier-filtered. A black hexagon should indicate the hexagonal lattice.

In order to further investigate the surface, detailed STM images can be seen in fig.

6.10. The surface has a complex pattern which can be roughly described by stripes with angles of 60° and a width of $\approx 20\,\text{Å}$. Occasional triangular shapes interrupt left- and right-handed stripes. At a closer look as seen in the Fourier-filtered (FT) image in subfigure (b), a hexagonal structure can be vaguely identified. Lattice constants from FT are in agreement with LEED, resulting in the underlying hexagonal structure being the $\left(\frac{5}{4} \times \frac{5}{4}\right)$ pattern.

The large-scale superstructure is not identical to the herringbone reconstruction on Au(111). Due to the presence in LEED measurement, these are still present on the surface at high coverage, but no effect of the herringbone reconstruction can be found on the surface. This could be an indication that the herringbone reconstruction slightly alters the bonding of GeSe to the Au atoms and is therefore responsible for the observed superstructure.
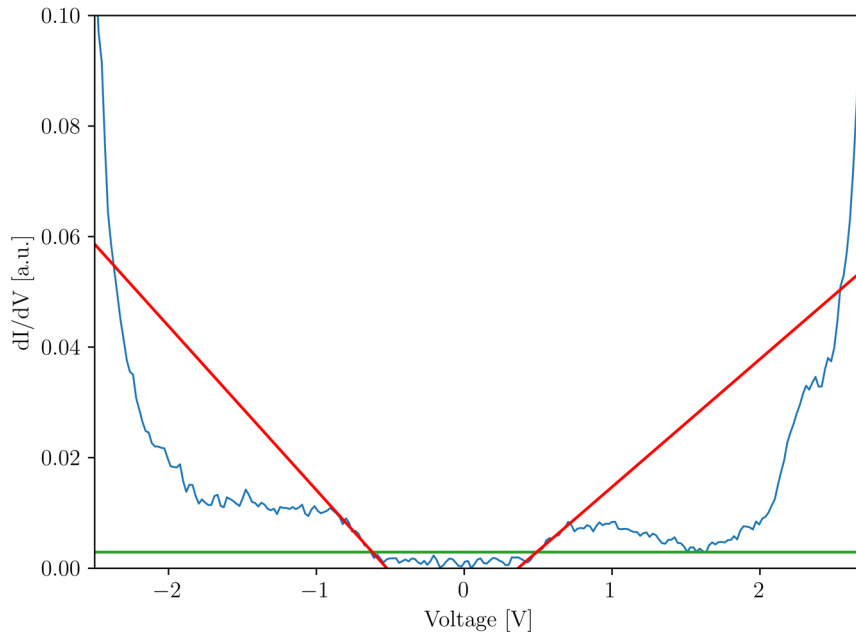
Figure 6.11: Electronic measurement with STS on 2D-bulk β-GeSe, reveal a semiconducting nature with a bandgap of $E_{\text{G}} = 1.113 \pm 0.015\,\text{eV}$. The red lines are fitted to the initial slope, the green line represents the error free level at 3σ above the noise level in the gap.

STS measurements in the form of dI/dV of the β-GeSe layer reveal a gap in the band from $-0.6\,\text{V}$ to $-0.5\,\text{V}$ which is followed by a region of nearly constant value before the signal is strongly increased at around $\pm 2\,\text{V}$. This indicates a semiconductor with a bandgap of $E_{\text{G}} = 1.113 \pm 0.015\,\text{eV}$ with an interesting region between $\pm(1\text{ to }2)\,\text{V}$ where a constant DOS is present.

Theoretical calculations of the bandgap of monolayer β-GeSe are ambiguous. Some are in good agreement with this measurement [101], others state larger values [35]. Also, the bulk value with just a slight decrease ($1.2\,\text{eV}$ [94]) could be explained by confinement effects or substrate interactions with surface states. Since the onset of the 2D-bulk valence and conduction band is not at the energy of the bandgap, but rather after a $\approx \pm 1.5\,\text{eV}$ gap, this leads to the believe that singular bands extend in the energy landscape.

With this insight, measurements of island shapes and edges could be possible, despite the rather difficult sub-monolayer growth and crystallisation conditions.

Chapter 7

Tin Sulfide

The interest in tin sulfide (SnS) among other MXs is rather large since it is theoretically predicted to have stable ferroelectricity across an extensive temperature range [10, 15, 102, 103] while having a relative low formation energy.
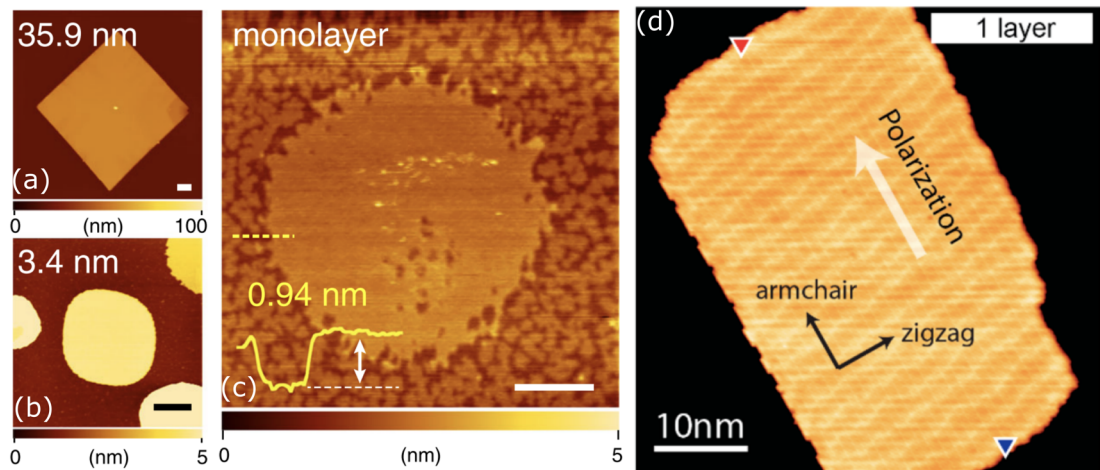

Figure 7.1: Experimental results of SnS in literature. AFM images of differently thick SnS layers, ranging from $359\,\text{Å}$ in (a), $34\,\text{Å}$ in (b), and a monolayer of $9\,\text{Å}$ in (c), all adapted from [102]. All experiments were performed on a mica substrate. (d) STM image of SnS on Au(111) revealing a superstructure pattern orthogonal to the polarisation direction, image adapted from [4]. The island is shown with indicated lattice directions of AC and ZZ. The triangles suggest further measurement points for determining polarisation direction (not shown). All measurements of both authors were performed at temperatures below $4\,\text{K}$.

Studies so far covered mostly few to multilayer experiments. However, Higashitarumizu *et al.* report the creation of monolayer SnS via physical vapour deposition on isolated mica [102]. AFM images can be seen in fig. 7.1 (a)-(c) for various thicknesses, ranging from ML (c) up to $359\,\text{Å}$ (a). This study could indicate that island shape is directly linked to layer thickness. While the thickest investigated layer forms straight edges with a rectangular shape, islands with a few layers start to become more round. ML SnS here has a wedding cake morphology, with one large round island surrounded by smaller ones, most likely due to Stranski-Krastanov growth. The rounded shape is probably caused by desorption processes during growth and insufficient conditions to reach the thermodynamic equilibrium shape [102].
Measurements of mono- and multilayer SnS using second-harmonic generation confirm a lack of inversion symmetry and thus ferroelectricity. This was also found in even

layered films, which is unexpected due to the compensation in symmetry resulting in a centrosymmetric structure with no net polarisation. Electric transport measurements found an even higher coercive field of 25 kV/cm for 9 layers of SnS.

Bao *et al.* investigated few-layer SnS via STM for imaging and piezoresponse-force microscopy (PFM) to study the ferroelectric properties [4]. Such a ML island on Au(111) is shown in fig. 7.1 (d). The shape has straight edges, suggesting it is close to the equilibrium shape. However, such a rectangular shape could not be observed in other MXs, like ML SnSe. A superstructure pattern can be seen, which can not be explained by a moiré between structure and island or substrate-induced strain, because of its presence even for multilayer islands [4]. For measuring the direction of polarisation, the local contact potential difference was measured using non-contact AFM, positions are highlighted in fig 7.1 (d) by the triangles. The polarisation direction is shown parallel to the AC direction and marked red for positive and blue for negative polarisation. For the actual values, samples were prepared on corrugated graphite by MBE, to overcome the direction problem of the in-plane ferroelectricity and out-of-plane PFM measurement. They found a finite polarisation signal and could measure a hysteresis with a coercive field of 10.7 kV/cm in devices based on SiO_2. However, the authors found for those islands an even-odd layer effect, suggesting a centrosymmetric stacking dependency. This is in contradiction to the results from [102]. Possible reasons for this difference can be due to different measurement techniques or differences in preparation, resulting in other stacking alignments.

Although different successful growth methods for SnS are already available, the reports are still quite scarce and studies suggest ambiguous results.

Therefore, this chapter covers the crystallization of SnS on gr/Ir(111) (sec 7.1) and gives first indications to the Curie temperature T_C by annealing measurements in sec. 7.2.

7.1 Crystallization on gr/Ir(111)

Similar to the previous experimental studies, evaporation of tin sulfide was also done using powder (5N, American Elements) from an effusion cell, as presented in fig. 3.10. Evaporation rates and temperature are optimised by using QMB and QMS. Both measurements are presented in fig. 7.2.

The main frame shows that the deposition rates for SnS from a heated crucible follow an exponential trend line (in blue) with the onset of evaporation at around 650 K. QMS measurements reveal, with the residual gas analysis, which atoms are deposited at the microbalance. It shows that in an early stage sulfur evaporates primarily, which can be identified by multiples of mass 32 [61]. In order to distinguish sulfur from oxygen, the peaks at mass 15 and 16 need to be missing. These kinds of measurements were used to find the ideal temperature where the SnS dimer peaks are maximised. One example at an evaporator temperature of 750 K is shown in the inset of fig. 7.2, where the main peak of SnS is indicated at 152.1 amu. Besides that, there are many peaks stemming from the isomers of SnS. In order to truly identify these peaks, the predicted values can be calculated from the natural occurrence of isomers of Sn and S. For a unit-less comparison, the ratios of each peak of the composite SnS were used. Those ratios fit the equivalent ratios which are measured in QMS. At the left edge of the graph at around mass 118, the isomers of Sn can be seen, which are here larger than the peaks of the dimers.

Further on, an evaporator temperature of $T_{evap} = 698$ K and the corresponding rather low rate of 1.1×10^{-3} ML/s are used. This is achieved by a sample evaporator distance of 8.25 cm. It is important to mention that the evaporator temperature was fixed not only because of an increased dimer output but also because of characteristics of the
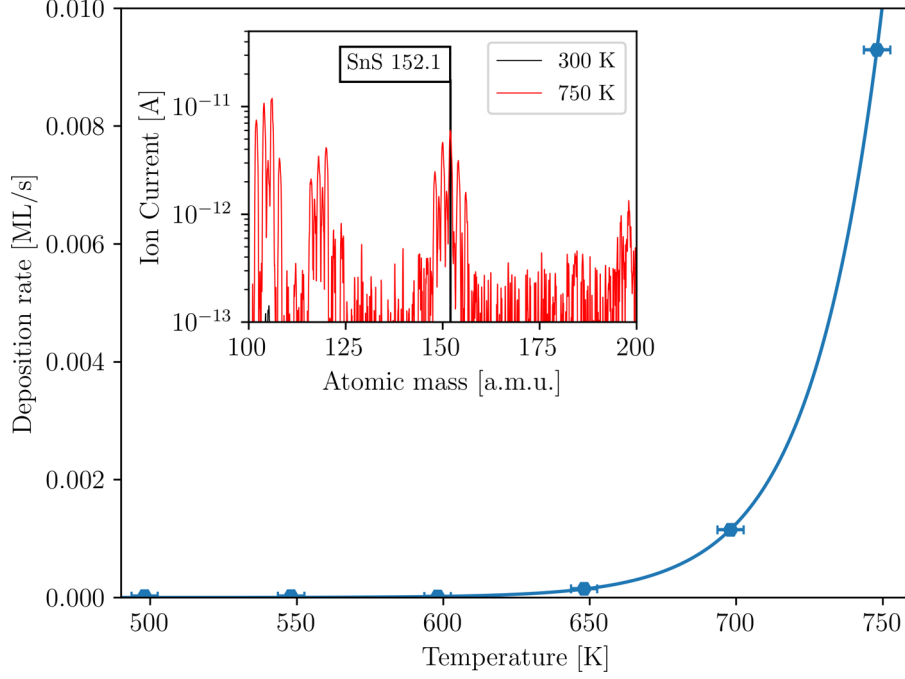
Figure 7.2: Evaporation behaviour in terms of deposition rate and atomic composition in residual gas analysis of SnS from an effusion cell, measured by QMB and QMS (inset), in dependence of evaporator temperature. The deposition rate increases exponentially (fitted by the blue line) with increasing crucible temperature. Two QMS measurements at 300 K and 750 K are shown. The main peak of SnS is indicated.

phase diagram [104]. Although it suggests that the stoichiometric structure is the most stable at any temperature. At higher temperatures than the chosen ones, a phase change from α- to β-phase in the bulk evaporation material is induced [104]. Note, that the same naming scheme as the one introduced in chapter 2, is used and the α-phase is generally the preferred one due to its in-plane ferroelectric characteristics.

Tin sulfide crystallises on gr/Ir(111) already at room temperature, as can be seen in the LEED image in fig.7.3. This differentiates the gr surface from previous discussed substrates, as kinetic energy was needed for crystallisation on other surfaces [4, 102]. The figure shows a measurement at 137.1 eV of roughly 2.6 ML of SnS. This is more an estimation, due to the limitations of QMB. The reflexes of gr and Ir are highlighted in red, with the inner reflex corresponding to gr. The weak intensity is most likely due to the large coverage. However, this results in 24 clear first-order SnS spots. Analogues to SnSe, these can be grouped in three sets of 8 spots each, which reflect the three orientations obtainable on the graphene surface. Each set is highlighted in a different colour (green, blue, and yellow) and reciprocal lattice vectors of a and b are drawn in for one orientation. Some spots appear weaker or are completely missing due to defects on the LEED screen. Therefore, some highlights are not indicated.

Lattice constants are determined as $a = 4.42 \pm 0.13$ Å and $b = 4.16 \pm 0.08$ Å, which is in agreement with theoretical values [15] and experimental results [4]. The orientation of the lattice vectors is contrary to the aforementioned SnSe vectors, but stated in this form to keep $a > b$ and the ratio of a/b positive. In this case, the lattice constant a aligns with the zigzag $\langle 11\bar{2}0 \rangle$-direction of graphene, most likely due to the better fit to the graphene lattice constant.
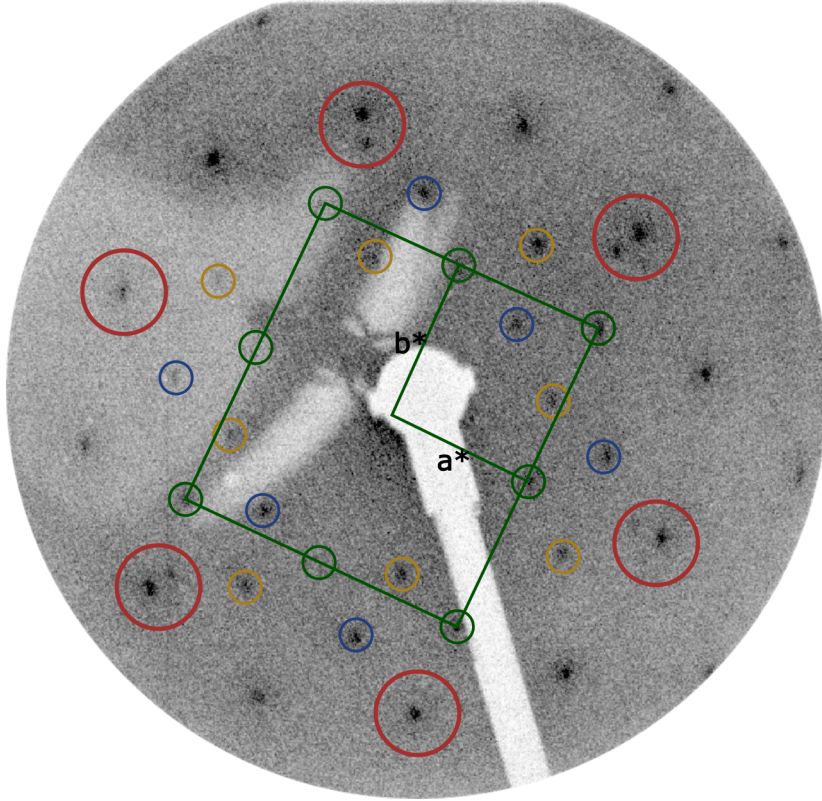
Figure 7.3: LEED measurement of SnS on gr/Ir(111) at 137.1 eV, grown at $(1.1 \times 10^{-3}$ ML/s, 2400 s, RT). The first-order reflexes of gr/Ir are highlighted in red, while first-order SnS spots are grouped in three times 8 spots, circled in green, blue, and yellow. Additionally, one group is highlighted with reciprocal lattice vectors of a and b.

7.2 Hints towards Curie temperature

Theoretical reports state that the Curie temperature of tin sulfide is around 1200 K [15]. Such a large temperature is not only in an usable range but also beneficial for ferroelectric properties. As a result of the Landau theory, the spontaneous polarisation is proportional to the Curie temperature. Hypothetically, this results in a large spontaneous polarisation. During the second-order phase transition close to T_C, the lattice constants should shift from an orthorhombic $(a \neq b)$ to a squared lattice $(a = b)$. Therefore the ratio of a/b is strongly temperature-dependent. The investigation of lattice constant ratios, calculated from LEED measurements, in dependence on temperature, is shown in fig. 7.4.

The lattice constants a and b were determined and averaged with the rotational orientations. The error is large due to the standard deviation of the ratio with the errors of each lattice constant. The error in temperature is due to the measurement technique with a pyrometer. LEED image of the room temperature measurement is shown in fig. 7.3. The sample is continuously further annealed while measurements are taken. Due to the limitations of the pyrometer, the low temperatures are approximated by assuming a linear correspondence to the heating filament current.

The data suggest a gradual change in the lattice constant ratio towards zero. Note the large line break in temperature. Due to the second-order transition, measurement points are focussed around the transition itself.
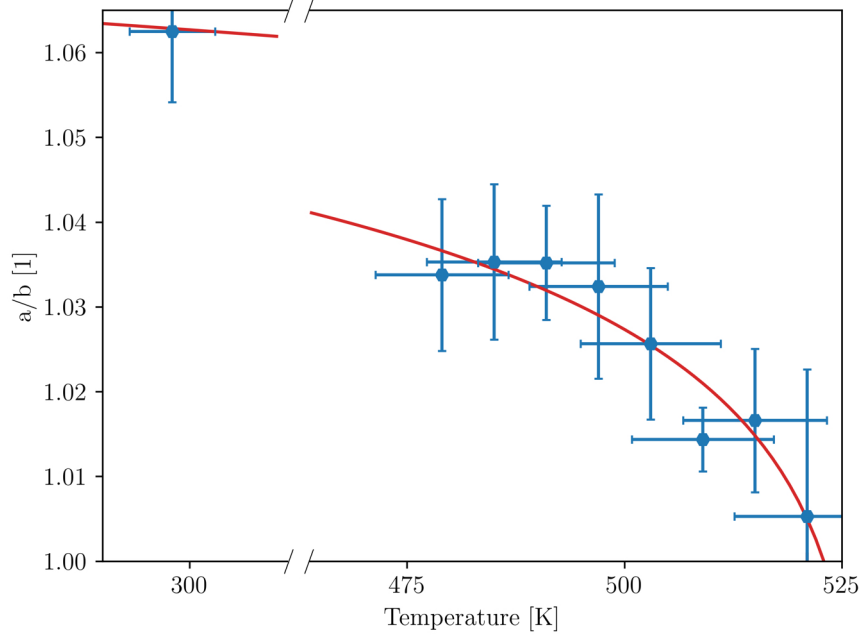
Figure 7.4: Lattice constant ratio a/b, measured by evaluating LEED images in dependency of the sample temperature, indicates a phase transition. The data is fitted with the Curie-Weiss law as seen in eq. 7.2.1 (red line).

The ratio of a/b can be fitted with an adjusted Curie-Weiss law

$$\left(\frac{a}{b}\right)(T) = \left(\frac{a}{b}\right)_{0\,\mathrm{K}} \cdot \left(1 - \frac{T}{T_{\mathrm{C}}}\right)^{\gamma},\qquad(7.2.1)$$

where the fit (red line) results in the lattice constant ratio at $0\,\mathrm{K}$ of $\left(\frac{a}{b}\right)_{0\,\mathrm{K}} = 1.077$, Curie temperature of $T_{\mathrm{C}} = 528\,\mathrm{K}$, and critical exponent $\gamma = 1.619 \cdot 10^{-2}$. This method allows an estimation of the transition temperature from experimental values. The lattice constant ratio at $0\,\mathrm{K}$ is plausible due to the close value at RT with 1.063. However, this result suggests that the Curie temperature is less than half of the theoretically predicted, which can have many reasons. The observed SnS material is embedded in a layered system and not (typically for models) completely freestanding [15]. It is known, that strain can affect electronic properties in MX, as shown for GeSe in [105]. Besides that, methodically the complete paraelectric phase ($a = b$) could not be reached in our system. The onset of desorption processes can be found at around $550\,\mathrm{K}$, which is close to T_{C}. The increasing error bars with temperature can be explained due to technical limitations. LEED measurements at higher temperatures lead to no meaningful result anymore, since the background lighting of the heating filament then dominates over any reflection spots.

Generally, desorption processes should not affect the lattice constants, but the effect of lattice expansion due to thermal heat could be an influence, which is here neglected. Theoretical models assume a fixed lattice constant a while the lattice only alters in $\langle 100 \rangle$ direction [15]. In experiment, this trend is not clear and both lattice constants change with temperature. Due to the large error in this method, it is difficult to assume that $a \propto a_{\mathrm{gr}}$ for all temperatures.

In order to stabilize the paraelectric phase, there is the option to increase layer stability with a stronger interacting substrate. Similar arguments were discussed in chapter 6 and a similar growth method can also be used for a Au(111) surface with crystallisation at RT. The resulting LEED measurements of SnS on Au(111) are presented in fig. 7.5.
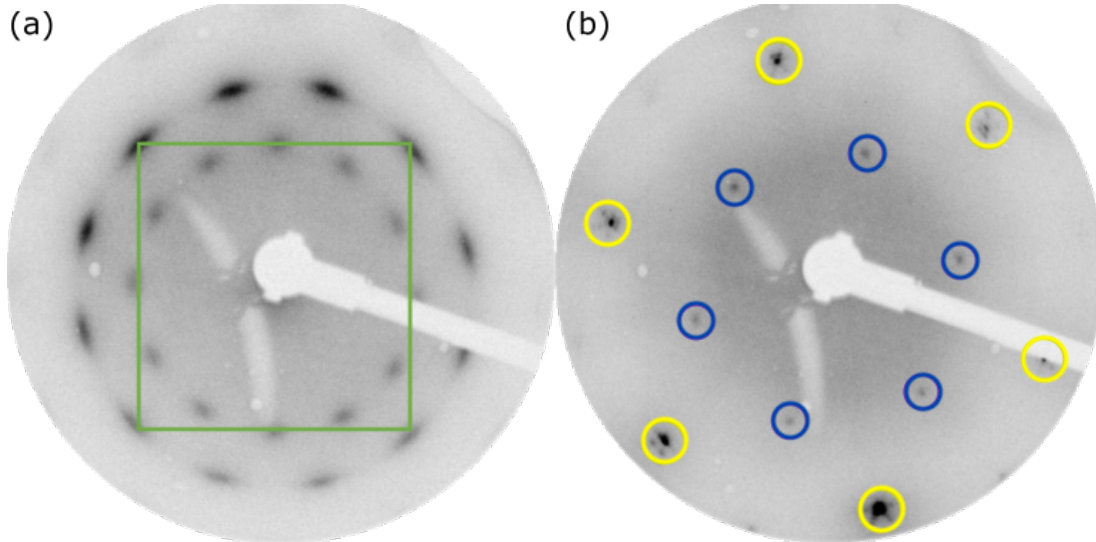
Figure 7.5: LEED images after $\Theta = 5.3\,\text{ML}$ SnS deposition on Au(111) surface, both at 70 eV. (a) The pristine state directly after growth ($698\,\text{K}$, $3.5 \times 10^{-3}\,\text{ML/s}$, $1500\,\text{s}$, RT) shows 24 reflexes, grouped in 3×8 spots with a square lattice, indicated in green. (b) After further treatment with annealing at $420\,\text{K}$ for $600\,\text{s}$ six Au(111) spots (yellow), as well as $\sqrt{3}$ reflexes (magenta) appear, while the previously seen pattern disappears.

After deposition of 5.3 ML SnS on Au(111) at room temperature two concentric rings of 12 spots each appear in LEED measurements, as seen in subfigure (a). These reflexes are quite elongated indicating some rotational freedom in the prepared structure. Those total 24 spots can also be grouped in three sets of 8 reflexes each, which then form a squared lattice: $a/b = (1.00 \pm 0.02)\,\text{Å}$. The reflexes stemming from the Au(111) are no longer visible, which is likely due to increased layer thickness. This hinders any lattice constant evaluation. In order to investigate the temperature dependence, an early onset of desorption could be found. The annealing treatment is performed at $420\,\text{K}$ for $600\,\text{s}$. This results in the diffraction image seen in subfigure (b).

The previously seen structure has vanished and been replaced by a structure, formed by six spots (highlighted in magenta), which can be described as $(\sqrt{3} \times \sqrt{3})\text{R}30°$ to the Au(111) (yellow). Faintly the six reflexes around the Au(111) spot, stemming from the herringbone reconstruction can be seen as well. This pattern fits the results of other reports of pure sulfur on Au(111) [106, 107]. The annealing temperature and duration were varied, but no other result than the measurements shown and a pure Au(111) structure could be observed.

The main idea of this experiment is that the first MX layer is more stable than any further layer, due to the direct interaction to the substrate. Therefore due to the annealing treatment, the bulk structure should reduce to a monolayer before the phase transition to the paraelectric state. This experiment shows that this is not the predominant mechanism for this material. Other reports related to SnSe on a Au(111) surface [81], experience similar behaviour when annealing from a multilayer structure. They state that such multilayer structure, in this case SnSe, result primarily in the β-phase structure. Any annealing treatment also results in only chalcogen atoms being bound to the surface. From this result and ncAFM measurements, they conclude that the layer is bound primarily by the chalcogen atom to the Au(111) surface, which should be a similar case here with the sulfur atom.

Chapter 8

Summary and outlook

In this thesis, the study on different ferroelectric materials of the group-IV monochalco-genide group is presented. All materials were prepared by MBE in UHV on various substrates.

In summary, the first of the projects presented here aimed to investigate SnSe islands on a gr/Ir(111) sample. After deposition at room temperature, the islands can be described with a fractal-dendritic shape. This is indicating that step-edge diffusion is hampered. The islands were analysed in an annealing sequence in terms of coverage, island density, and a newly introduced shape parameter, to quantitatively make a statement of the changes in shape. However, annealing does not lead to any ripening processes (Ostwald or Smoluchowski) before the desorption of the islands is thermally favoured at temperatures around 600 K. Nevertheless, before desorption becomes relevant, the morphology of the islands change to compact rhombic islands due to the onset of step edge diffusion. The preparation used a two-step process, which consists of a nucleation step of SnSe islands at room temperature and a second step with further deposition at elevated temperature. This method results in well-formed large islands which are epitaxially aligned with the substrate. Such a method could also be suitable for other 2D materials, in order to grow large, aligned, and well-ordered islands. For this investigated system, the shape of the islands is predominantly defined by edges in $\langle 110 \rangle$ direction, which resembles an armchair-like characteristic. The resulting shape is then defined as the equilibrium shape. The experimental observation of preferred edges can not be explained by a simple bond-counting model. These findings can be described by an edge relaxation which is also found in DFT calculations. However, the theoretical description of the edge energies is limited due to the fact that the system is close to the ferroelectric-paraelectric phase transition. It follows that the energy landscape has a quite shallow potential. The Wulff construction, based on the edge energies of the calculations to predict the island shape, agrees with the experimentally found equilibrium shape. The edge relaxation can also be found in atomically-resolved images of the preferred edge, which are in agreement with theoretically predicted structures. The calculations are extended to incorporate non-stoichiometric edges to predict edge energies for other growth methods which could result in atomic deficient edges. Energies, potential and predicted shape from Wulff constructions can help identifying the degree of Se deficiency from the stoichiometric case. The description of the atomic processes during the epitaxial growth can provide a guidance to suitable preparation parameters for desired island shapes and sizes. The determination of the dominant edge structure in the equilibrium shape can support future studies, to further characterise the ferroelectric properties of SnSe monolayer islands. The electric potential calculation indicates a reduction in response at the edge between non optimised and relaxed structure and therefore emphasises the challenges that such ferroelectric characterisation entails.

The formation of bilayer structure is rarely discussed in literature. Islands of SnSe on gr/Ir(111) with increased dimensionality are studied and found to have a similar kinetic behaviour in terms of shape change. LEED measurements demonstrate the existence of multiple phases, which are orthogonally rotated to each other. However, the onset of the bilayer formation is directly linked to large coverage. This enables the creation of domain boundaries, which nearly seamlessly grow together despite the differently rotated lattices. The evolution of individual layer coverage in dependency of the total coverage reveals that the initial growth of SnSe can be described as statistical, which results in mainly monolayer structures. Once a total coverage of $\approx 0.6\,\mathrm{ML}$ is reached, bilayer formation is strongly preferred. If the total coverage is larger than $\approx 1\,\mathrm{ML}$, no monolayer could be observed. This surprising growth dynamic leads to the proposal of a critical island size. By investigation of the circumference and area of multiple large single-domain islands, the indication could be found that there is energetically a maximum in monolayer side length at $640\,\text{\AA}$. This is determined by the smallest bilayer structure observed since large a monolayer could be grown from different nucleation points. The observation of only pure mono- or bilayer is justified by an estimation of relevant surface energies. Although this estimation does not reflect the same critical size as the experimental data, this is most likely due to the problem of identifying a suitable interface energy. It can be proposed that bilayer formation happens at a critical size in terms of a shape change due to energetically unfavoured edge conditions. The observation of multiple phases is also supported by electronic band gap measurements. Unfortunately, no existing theoretical description is in agreement. Electric potential calculations show a strong dependency on the topmost layer. However, STS maps do not reflect this behaviour. Instead, an edge state all around the island can be observed. This is an indication that there also could be relaxations or reconstructions involved for bilayer SnSe. Studies on the isostructural bilayer phosphorene show multiple possible reconstructions.

The deposition of GeSe on graphene samples on different metal substrates resulted in amorphous films, despite various conditions for crystallisation. This observation can have multiple possible reasons, with arguments in terms of energetics and growth methods. Nevertheless, this study shows that crystallisation conditions for monolayer structures are not in alignment with UHV and MBE conditions, such that other growth methods or substrate materials are needed. For the Au(111) substrate, the first preparation of β-GeSe is demonstrated, which results in a $\frac{5}{4} \times \frac{5}{4}$ pattern in regards to the Au(111) substrate. Lattice constant determination also supports this relation. Imaging of the surface reveals a complicated superstructure with a hexagonal sub-lattice, as LEED suggests with the alignment to the hexagonal gold and multiple additional reflection spots. Electronic measurements of the band gap reveal only a slightly lower band gap than the bulk material.

The crystallisation of SnS by MBE in UHV conditions could be realised on a gr/Ir(111) as well as on a Au(111) substrate. Lattice constant evaluation reveals monolayer characteristics. However, the structure on Au resulted in a square lattice, most likely due to transitioning to the paraelectric bulk material. A method to identify the Curie temperature of the transition from ferro- to paraelectric state is presented in the form of lattice constant evaluation by LEED measurements at elevated temperatures. This results in a change in the lattice constant ratio. With this method, the Curie temperature of $T_C = 521\,\mathrm{K}$ could be determined, which is significantly lower than theoretical reports state. Unfortunately, due to an early onset of desorption, no true paraelectric phase could be observed.

Such studies could benefit from the use of low-temperature STM to overcome the difficult measurement conditions needed for imaging. Other methods, like optical spectroscopy,

to probe existing samples are difficult to implement due to the stability problem in ambient conditions. However, multiple theoretical reports state large optical absorption [108]. Alternative methods that are more accessible in UHV conditions are, for example, x-ray diffraction (XRD) and angle-resolved photo emission spectroscopy (ARPES). Since the transition from the ferroelectric to paraelectric state is purely structural, diffraction methods can be useful here, in the assumption that desorption processes have a lower activation energy than the transition barrier. The study of orientation in bilayer formations could also be performed by diffraction since scanning probe imaging is mostly sensitive to the topmost layer. The unique shape with a broad area of constant DOS in the band structure of GeSe could be further investigated by ARPES measurements.

This work covered multiple group-IV monochalcogenide materials in various stages of their ferroelectric characterisation and focussed mainly on preparation and crystallographic properties. Given the novelty and complexity of these materials, the way to a real-world application using 2D ferroelectric behaviour still requires further investigation. In order to unlock the full potential, a deeper understanding of the electronic properties and full layer growth is needed. Nevertheless, such promising properties of this special material class could suggest great opportunities for future work.

Bibliography

[1] T. Mikolajick, U. Schroeder, and S. Slesazeck, "The Past, the Present, and the Future of Ferroelectric Memories", *IEEE Transactions on Electron Devices*, vol. 67, no. 4, pp. 1434–1443, Apr. 2020. DOI: 10.1109/TED.2020.2976148.

[2] Y. Cai, G. Zhang, and Y.-W. Zhang, "Electronic and Optical Properties of Phosphorene", in *Phosphorene*, vol. 128, American Institute of Physics Inc., Sep. 2020, pp. 149–214. DOI: 10.1201/b22476-5.

[3] C. Chowdhury, S. Karmakar, and A. Datta, "Monolayer Group IV-VI Monochalcogenides: Low-Dimensional Materials for Photocatalytic Water Splitting", *Journal of Physical Chemistry C*, vol. 121, no. 14, pp. 7615–7624, 2017. DOI: 10.1021/acs.jpcc.6b12080.

[4] Y. Bao, P. Song, Y. Liu, Z. Chen, M. Zhu, I. Abdelwahab, J. Su, W. Fu, X. Chi, W. Yu, W. Liu, X. Zhao, Q. H. Xu, M. Yang, and K. P. Loh, "Gate-Tunable In-Plane Ferroelectricity in Few-Layer SnS", *Nano Letters*, vol. 19, no. 8, pp. 5109–5117, Aug. 2019. DOI: 10.1021/acs.nanolett.9b01419.

[5] K. S. Novoselov, A. K. Geim, S. V. Morozov, D. Jiang, Y. Zhang, S. V. Dubonos, I. V. Grigorieva, and A. A. Firsov, "Electric field in atomically thin carbon films", *Science*, vol. 306, no. 5696, pp. 666–669, Oct. 2004. DOI: 10.1126/science.1102896.

[6] S. Z. Butler *et al.*, "Progress, challenges, and opportunities in two-dimensional materials beyond graphene", *ACS Nano*, vol. 7, no. 4, pp. 2898–2926, 2013. DOI: 10.1021/nn400280c.

[7] K. Chang *et al.*, "Discovery of robust in-plane ferroelectricity in atomic-thick SnTe", *Science*, vol. 353, no. 6296, pp. 274–278, Jul. 2016. DOI: 10.1126/science.aad8609.

[8] K. Chang, F. Küster, B. J. Miller, J. R. Ji, J. L. Zhang, P. Sessi, S. Barraza-Lopez, and S. S. Parkin, "Microscopic Manipulation of Ferroelectric Domains in SnSe Monolayers at Room Temperature", *Nano Letters*, vol. 20, no. 9, pp. 6590–6597, Sep. 2020. DOI: 10.1021/acs.nanolett.0c02357.

[9] K. Chang and S. S. P. Parkin, "Experimental formation of monolayer group-IV monochalcogenides", *Journal of Applied Physics*, vol. 127, no. 22, p. 220 902, Jun. 2020. DOI: 10.1063/5.0012300.

[10] S. Barraza-Lopez, B. M. Fregoso, J. W. Villanova, S. S. Parkin, and K. Chang, "Colloquium: Physical properties of group-IV monochalcogenide monolayers", *Reviews of Modern Physics*, vol. 93, no. 1, p. 11 001, Mar. 2021. DOI: 10.1103/RevModPhys.93.011001.

[11] P. Sutter and E. Sutter, "Growth Mechanisms of Anisotropic Layered Group IV Chalcogenides on van der Waals Substrates for Energy Conversion Applications", *ACS Applied Nano Materials*, vol. 1, no. 6, pp. 3026–3034, May 2018. DOI: 10.1021/acsanm.8b00660.

[12] H. Liu, A. T. Neal, Z. Zhu, Z. Luo, X. Xu, D. Tománek, and P. D. Ye, "Phosphorene: An unexplored 2D semiconductor with a high hole mobility", *ACS Nano*, vol. 8, no. 4, pp. 4033–4041, Apr. 2014. DOI: 10.1021/nn501226z.

[13] M. Wu and X. C. Zeng, "Intrinsic Ferroelasticity and/or Multiferroicity in Two-Dimensional Phosphorene and Phosphorene Analogues", *Nano Letters*, vol. 16, no. 5, pp. 3236–3241, May 2016. DOI: 10.1021/acs.nanolett.6b00726.

[14] P. Z. Hanakata, A. Carvalho, D. K. Campbell, and H. S. Park, "Polarization and valley switching in monolayer group-IV monochalcogenides", *Physical Review B*, vol. 94, no. 3, p. 035 304, Jul. 2016. DOI: 10.1103/PhysRevB.94.035304.

[15] R. Fei, W. Kang, and L. Yang, "Ferroelectricity and Phase Transitions in Monolayer Group-IV Monochalcogenides", *Physical Review Letters*, vol. 117, no. 9, p. 097 601, Aug. 2016. DOI: 10.1103/PhysRevLett.117.097601.

[16] M. Mehboudi, B. M. Fregoso, Y. Yang, W. Zhu, A. Van Der Zande, J. Ferrer, L. Bellaiche, P. Kumar, and S. Barraza-Lopez, "Structural Phase Transition and Material Properties of Few-Layer Monochalcogenides", *Physical Review Letters*, vol. 117, no. 24, p. 246 802, Dec. 2016. DOI: 10.1103/PhysRevLett.117.246802.

[17] H. Shen, J. Liu, K. Chang, and L. Fu, "In-Plane Ferroelectric Tunnel Junction", *Physical Review Applied*, vol. 11, no. 2, p. 024 048, Feb. 2019. DOI: 10.1103/PhysRevApplied.11.024048.

[18] T. Michely and J. Krug, *Islands, Mounds and Atoms* (Springer Series in Surface Sciences). Berlin, Heidelberg: Springer Berlin Heidelberg, 2004, vol. 42. DOI: 10.1007/978-3-642-18672-1.

[19] K. W. Böer and U. W. Pohl, *Properties and Growth of Semiconductors*. Springer, Cham, 2022, pp. 1–32. DOI: 10.1007/978-3-319-06540-3_1-4.

[20] Z. Liu, H. Wu, W. Ren, and Z. G. Ye, *Piezoelectric and ferroelectric materials: Fundamentals, recent progress, and applications*. Elsevier, 2023, vol. 1-10, pp. 135–171. DOI: 10.1016/B978-0-12-823144-9.00069-8.

[21] P. Li and F. Ding, "Origin of the herringbone reconstruction of Au(111) surface at the atomic scale", *Science Advances*, vol. 8, no. 40, Oct. 2022. DOI: 10.1126/sciadv.abq2900.

[22] P. Koskinen, S. Malola, and H. Häkkinen, "Self-passivating edge reconstructions of graphene", *Physical Review Letters*, vol. 101, no. 11, 2008. DOI: 10.1103/PhysRevLett.101.115502.

[23] P. Masih Das, G. Danda, A. Cupo, W. M. Parkin, L. Liang, N. Kharche, X. Ling, S. Huang, M. S. Dresselhaus, V. Meunier, and M. Drndić, "Controlled Sculpture of Black Phosphorus Nanoribbons", *ACS Nano*, vol. 10, no. 6, pp. 5687–5695, Jun. 2016. DOI: 10.1021/acsnano.6b02435.

[24] M. Petrović, M. Horn von Hoegen, and F. J. Meyer zu Heringdorf, "Equilibrium shape of single-layer hexagonal boron nitride islands on iridium", *Scientific Reports*, vol. 9, no. 1, pp. 1–6, Dec. 2019. DOI: 10.1038/s41598-019-56000-1.

[25] R. Zhao, J. Gao, Z. Liu, and F. Ding, "The reconstructed edges of the hexagonal BN", *Nanoscale*, vol. 7, no. 21, pp. 9723–9730, 2015. DOI: 10.1039/c5nr02143j.

[26] Z. Zhang, A. Kutana, and B. I. Yakobson, "Edge reconstruction-mediated graphene fracture", *Nanoscale*, vol. 7, p. 2716, 2015. DOI: 10.1039/c4nr06332e.

[27] L. Liang, J. Wang, W. Lin, B. G. Sumpter, V. Meunier, and M. Pan, "Electronic bandgap and edge reconstruction in phosphorene materials", *Nano Letters*, vol. 14, no. 11, pp. 6400–6406, Nov. 2014. DOI: 10.1021/nl502892t.

[28] Y. Liu, X. Shang, J. Zhuang, D. Li, and T. Cui, "Recent progress in the edge reconstruction of two-dimensional materials", *J. Phys. D: Appl. Phys.*, vol. 55, no. 41, Aug. 2022. DOI: `10.1088/1361-6463/ac855f`.

[29] A. Bhalla and A. Saxena, "Ferroelectricity - 100 years on", *Physics World*, 2020.

[30] S. Horiuchi and Y. Tokura, "Organic ferroelectrics", *Nature Materials*, vol. 7, no. 5, pp. 357–366, 2008. DOI: `10.1038/nmat2137`.

[31] V. Fridkin and S. Ducharme, "The ferroelectricity at the nanoscale", *Ferroelectrics*, vol. 466, no. 1, pp. 133–144, Jul. 2014. DOI: `10.1080/00150193.2014.895201`.

[32] L. D. Landau, E. M. Lifshitz, L. P. Pitaevskiĭ, J. B. Sykes, and M. J. Kearsley, *Statistical physics, Part 1*, 5th ed. Pergamon Press, Oxford, 1980, p. 449.

[33] C. Künneth, R. Materlik, M. Falkowski, and A. Kersch, "Impact of Four-Valent Doping on the Crystallographic Phase Formation for Ferroelectric HfO2 from First-Principles: Implications for Ferroelectric Memory and Energy-Related Applications", *ACS Applied Nano Materials*, vol. 1, no. 1, pp. 254–264, Jan. 2018. DOI: `10.1021/acsanm.7b00124`.

[34] P. Hess, "Bonding, structure, and mechanical stability of 2D materials: The predictive power of the periodic table", *Nanoscale Horizons*, vol. 6, no. 11, pp. 856–892, Sep. 2021. DOI: `10.1039/d1nh00113b`.

[35] S. Zhang, S. Liu, S. Huang, B. Cai, M. Xie, L. Qu, Y. Zou, Z. Hu, X. Yu, and H. Zeng, "Structural and electronic properties of atomically thin germanium selenide polymorphs", *Science China Materials*, vol. 58, no. 12, pp. 929–935, Dec. 2015. DOI: `10.1007/s40843-015-0107-5`.

[36] A. S. Sarkar and E. Stratakis, *Recent Advances in 2D Metal Monochalcogenides*, Nov. 2020. DOI: `10.1002/advs.202001655`.

[37] H. Wang and X. Qian, "Two-dimensional multiferroics in monolayer group IV monochalcogenides", *2D Materials*, vol. 4, no. 1, p. 015 042, Jan. 2017. DOI: `10.1088/2053-1583/4/1/015042`.

[38] F. Neuman and O. E. Meyer, *Vorlesungen über die Theorie der Elasticität der festen Körper und des Lichtäthers*. 1885.

[39] J. Dai and X. C. Zeng, "Bilayer phosphorene: Effect of stacking order on bandgap and its potential applications in thin-film solar cells", *Journal of Physical Chemistry Letters*, vol. 5, no. 7, pp. 1289–1293, 2014. DOI: `10.1021/jz500409m`.

[40] J. H. Yang and X. G. Gong, "Stacking induced indirect-to-direct bandgap transition in layered group-IV monochalcogenides for ideal optoelectronics", *Journal of Materials Chemistry C*, vol. 7, no. 38, pp. 11 858–11 867, 2019. DOI: `10.1039/c9tc04085d`.

[41] B. Xu, J. Deng, X. Ding, J. Sun, and J. Z. Liu, "Interlayer Sliding-Induced Intralayer Ferroelectric Switching in Bilayer Group-IV Monochalcogenides", 2021. DOI: `10.1038/s41524-022-00724-8`.

[42] L. D. Zhao, S. H. Lo, Y. Zhang, H. Sun, G. Tan, C. Uher, C. Wolverton, V. P. Dravid, and M. G. Kanatzidis, "Ultralow thermal conductivity and high thermoelectric figure of merit in SnSe crystals", *Nature*, vol. 508, no. 7496, pp. 373–377, Apr. 2014. DOI: `10.1038/nature13184`.

[43] S. Barraza-Lopez, T. P. Kaloni, S. P. Poudel, and P. Kumar, "Tuning the ferroelectric-to-paraelectric transition temperature and dipole orientation of group-IV monochalcogenide monolayers", *Physical Review B*, vol. 97, no. 2, p. 24 110, 2018. DOI: `10.1103/PhysRevB.97.024110`.

[44]   Y. Wang, W. Chen, B. Wang, and Y. Zheng, *Ultrathin ferroelectric films: Growth, characterization, physics and applications*, 2014. DOI: `10.3390/ma7096377`.

[45]   A. Bremerich, "Heterojunctions of epitaxially grown transition metal dichalcogenides", Master thesis, University of Siegen, 2021.

[46]   B. E. Murphy, "The physico-chemical properties of fullerenes and porphyrin derivatives deposited on conducting surfaces.", Ph.D. dissertation, Trinity College Dublin, Dublin, 2014.

[47]   K. Oura, M. Katayama, A. V. Zotov, V. G. Lifshits, and A. A. Saranin, *Surface Science*. Berlin, Heidelberg: Springer Berlin Heidelberg, 2003. DOI: `10.1007/978-3-662-05179-5`.

[48]   D. Wilks, P. Aleksa, S. Chung, P. Modregger, D. V. Novikov, V. Vonk, A. Stierle, and C. Busse, "Structure determination of mono- and few-layers of the 2D-ferroelectric SnSe on graphene on Ir(111)", Poster presented at DPG 2023, Dresden, Germany.

[49]   B. Voigtländer, *Scanning probe microscopy*. Berlin, Heidelberg: Springer Berlin Heidelberg, 2015, vol. 2, pp. 1–980. DOI: `10.1007/978-0-387-28668-6`.

[50]   S. Lounis, "Theory of scanning tunneling microscopy", *45th IFF Spring School*, p. 38, Apr. 2014. DOI: `10.1007/BF00324308`.

[51]   H. J. Zandvliet and A. Van Houselt, "Scanning tunneling spectroscopy", *Annual Review of Analytical Chemistry*, vol. 2, pp. 37–55, 2009. DOI: `10.1146/annurev-anchem-060908-155213`.

[52]   I. Horcas, R. Fernández, J. M. Gómez-Rodríguez, J. Colchero, J. Gómez-Herrero, and A. M. Baro, "WSXM: A software for scanning probe microscopy and a tool for nanotechnology", *Review of Scientific Instruments*, vol. 78, no. 1, 2007. DOI: `10.1063/1.2432410`.

[53]   Nue Unique, "Nanoscience on the Tip: Scanning Tunneling Microscopy and Spectroscopy", Tech. Rep., 2016.

[54]   G. B. Armen, "Phase sensitive detection: the lock-in amplifier", Tech. Rep., 2008.

[55]   T. Chagas Silva Peixoto, "Tunneling spectroscopy of 2D materials: Unraveling their density of states and the relantionship with local atomic environment", Ph.D. dissertation, Universidade Federal de Minas Gerais, Belo Horizonte, Brazil, 2020.

[56]   J. Cai, "Monolayer Hexagonal Boron Nitride : an ultra-thin insulator", Ph.D. dissertation, University of Siegen, 2021.

[57]   Advanced Energy, "Non-Contact Temperature Measurement: Metallic, Ceramic and Graphite Surfaces", Tech. Rep., 2021.

[58]   V. Blecker, "Synthese und Struktur- bestimmung zweidimensionalen Germaniumselenids", Master thesis, University of Siegen, 2023.

[59]   National Instruments, "Calculating Thermocouple Measurement Error in DMM/Switch Temperature Measurement Systems", Tech. Rep., 2021.

[60]   S. Schill, "Inficon STM-2 Rate and Thickness Monitor", Tech. Rep.

[61]   B. Jenninger and P. Chiggiato, "CAS tutorial on RGA Interpretation of RGA spectra CAS on Vacuum for Particle Accelerators", *CERN Accelerator School*, p. 70, 2017.

[62] R. Van Gastel, A. T. N'Diaye, D. Wall, J. Coraux, C. Busse, N. M. Buckanie, F. J. Meyer Zu Heringdorf, M. Horn Von Hoegen, T. Michely, and B. Poelsema, "Selecting a single orientation for millimeter sized graphene sheets", *Applied Physics Letters*, vol. 95, no. 12, p. 121 901, 2009. DOI: 10.1063/1.3225554.

[63] J. W. Arblaster, "Crystallographic properties of iridium", *Platinum Metals Review*, vol. 54, no. 2, pp. 93–102, Apr. 2010. DOI: 10.1595/147106710X493124.

[64] C. Busse, "Nucleation and stacking-faults on the Ir(111) surface", Ph.D. dissertation, University of Aachen, 2003.

[65] L. Wang, S. N. Shirodkar, Z. Zhang, and B. I. Yakobson, "Defining shapes of two-dimensional crystals with undefinable edge energies", *Nature Computational Science*, vol. 2, no. 11, pp. 729–735, Nov. 2022. DOI: 10.1038/s43588-022-00347-5.

[66] P. Aleksa, M. Ghorbani-Asl, S. Iqbal, M. A. Martuza, A. Bremerich, D. Wilks, J. Cai, T. Chagas, R. Ohmann, A. V. Krasheninnikov, and C. Busse, "Transition from fractal-dendritic to compact islands for the 2D-ferroelectric SnSe on graphene/Ir(111)", *Nanotechnology*, vol. 35, no. 17, p. 175 707, Feb. 2024. DOI: 10.1088/1361-6528/AD2156.

[67] G. Kresse and J. Furthmüller, "Efficient iterative schemes for ab initio total-energy calculations using a plane-wave basis set", *Physical Review B - Condensed Matter and Materials Physics*, vol. 54, no. 16, pp. 11 169–11 186, Oct. 1996. DOI: 10.1103/PhysRevB.54.11169.

[68] G. Kresse and D. Joubert, "From ultrasoft pseudopotentials to the projector augmented-wave method", *Physical Review B - Condensed Matter and Materials Physics*, vol. 59, no. 3, pp. 1758–1775, Jan. 1999. DOI: 10.1103/PhysRevB.59.1758.

[69] J. P. Perdew, K. Burke, and M. Ernzerhof, "Generalized gradient approximation made simple", *Physical Review Letters*, vol. 77, no. 18, pp. 3865–3868, Oct. 1996. DOI: 10.1103/PhysRevLett.77.3865.

[70] A. Okazaki and I. Ueda, "The Crystal Structure of Stannous Selenide SnSe", *Journal of the Physical Society of Japan*, vol. 11, no. 4, p. 470, Apr. 1956. DOI: 10.1143/JPSJ.11.470.

[71] S. Iqbal, "Preparation of 2-D Group-IV Monochalcogenides", Master thesis, University of Siegen, 2021.

[72] F. Li, H. Wang, R. Huang, W. Chen, H. Zhang, F. Li, R. Huang, W. Chen, H. Wang, and H. Zhang, "Recent Advances in SnSe Nanostructures beyond Thermoelectricity", *Advanced Functional Materials*, vol. 32, no. 32, p. 2 200 516, Apr. 2022. DOI: 10.1002/adfm.202200516.

[73] H. von Koch, *Sur une courbe continue sans tangente, obtenue par une construction géométrique élémentaire*. Stockholm: P.A. Norstedt & Soner, 1904, vol. 1.

[74] J. E. Prieto, J. de la Figuera, and R. Miranda, "Surface energetics in a heteroepitaxial model system: Co/Cu(111)", *Physical Review B - Condensed Matter and Materials Physics*, vol. 62, no. 3, pp. 2126–2133, 2000. DOI: 10.1103/PhysRevB.62.2126.

[75] M. C. Bartelt and J. W. Evans, "Dendritic islands in metal-on-metal epitaxy I. Shape transitions and diffusion at island edges", *Surface Science*, vol. 314, no. 1, pp. L829–L834, Jul. 1994. DOI: 10.1016/0039-6028(94)90203-8.

[76] J. Coraux, A. T. N'Diaye, M. Engler, C. Busse, D. Wall, N. Buckanie, F. J. Meyer Zu Heringdorf, R. Van Gastel, B. Poelsema, and T. Michely, "Growth of graphene on Ir(111)", *New Journal of Physics*, vol. 11, no. 2, p. 023 006, Feb. 2009. DOI: `10.1088/1367-2630/11/2/023006`.

[77] C. Van Efferen, C. Murray, J. Fischer, C. Busse, H. P. Komsa, T. Michely, and W. Jolie, "Metal-insulator transition in monolayer MoS2 via contactless chemical doping", *2D Materials*, vol. 9, no. 2, p. 025 026, Mar. 2022. DOI: `10.1088/2053-1583/ac5d0f`.

[78] C. C. Silva, J. Cai, W. Jolie, D. Dombrowski, F. H. Farwick Zum Hagen, A. J. Martínez-Galera, C. Schlueter, T. L. Lee, and C. Busse, "Lifting Epitaxial Graphene by Intercalation of Alkali Metals", *Journal of Physical Chemistry C*, vol. 123, no. 22, pp. 13 712–13 719, Jun. 2019. DOI: `10.1021/acs.jpcc.9b02442`.

[79] B. Pielić, J. Hall, V. Despoja, I. Š. Rakić, M. Petrović, A. Sohani, C. Busse, T. Michely, and M. Kralj, "Sulfur Structures on Bare and Graphene-Covered Ir(111)", *Journal of Physical Chemistry C*, vol. 124, no. 12, pp. 6659–6668, Mar. 2020. DOI: `10.1021/acs.jpcc.9b11641`.

[80] A. T. N'Diaye, J. Coraux, T. N. Plasa, C. Busse, and T. Michely, "Structure of epitaxial graphene on Ir(111)", *New Journal of Physics*, vol. 10, pp. 43 033–43 049, 2008. DOI: `10.1088/1367-2630/10/4/043033`.

[81] F. Frezza, A. Sánchez-Grande, M. Ondráček, M. Vondráček, Q. Chen, O. Stetsovych, V. Villalobos-Vilda, E. Tosi, F. J. Palomares, M. F. López, C. Sánchez-Sánchez, K. H. Ernst, J. A. Martín-Gago, J. Honolka, and P. Jelínek, "Epitaxial growth and characterization of SnSe phases on Au(111)", *Journal of Physics Condensed Matter*, vol. 35, no. 33, p. 335 001, May 2023. DOI: `10.1088/1361-648X/acd49e`.

[82] G. Wulff, "Zur Frage der Geschwindigkeit des Wachsthums und der Auflösung der Krystallflächen", *Zeitschrift für Kristallographie - Crystalline Materials*, vol. 34, no. 1-6, pp. 449–530, Dec. 1901. DOI: `10.1524/ZKRI.1901.34.1.449`.

[83] X. Sang, X. Li, W. Zhao, J. Dong, C. M. Rouleau, D. B. Geohegan, F. Ding, K. Xiao, and R. R. Unocic, "In situ edge engineering in two-dimensional transition metal dichalcogenides", *Nature Communications*, vol. 9, no. 1, pp. 1–7, May 2018. DOI: `10.1038/s41467-018-04435-x`.

[84] C. Kamal, A. Chakrabarti, and M. Ezawa, "Direct band gaps in group IV-VI monolayer materials: Binary counterparts of phosphorene", *Physical Review B*, vol. 93, no. 12, p. 125 428, Mar. 2016. DOI: `10.1103/PhysRevB.93.125428`.

[85] A. K. Deb and V. Kumar, "Bandgap engineering in semiconducting one to few layers of SnS and SnSe", *Physica Status Solidi (B) Basic Research*, vol. 254, no. 2, p. 1 600 379, Feb. 2017. DOI: `10.1002/pssb.201600379`.

[86] B. Jiang, J. Neu, D. Olds, S. A. Kimber, K. Page, and T. Siegrist, "The curious case of the structural phase transition in SnSe insights from neutron total scattering", *Nature Communications*, vol. 14, no. 1, pp. 1–10, Jun. 2023. DOI: `10.1038/s41467-023-38454-0`.

[87] V. Q. Nguyen, V. T. Duong, T. H. Nguyen, R. Kang, A. T. Pham, V. T. Tran, C. K. Nguyen, A. T. Duong, T. B. Phan, J. Kim, and S. Cho, "Se/Sn flux ratio effects on epitaxial SnSe thin films; crystallinity & domain rotation", *Journal of Alloys and Compounds*, vol. 840, p. 155 680, Nov. 2020. DOI: `10.1016/j.jallcom.2020.155680`.

[88] J. R. Chin, M. B. Frye, D. S. H. Liu, M. Hilse, I. C. Graham, J. Shallenberger, K. Wang, R. Engel-Herbert, M. Wang, Y. K. Shin, N. Nayir, A. C. van Duin, and L. M. Garten, "Self-limiting stoichiometry in SnSe thin films", *Nanoscale*, vol. 15, no. 23, pp. 9973–9984, Jun. 2023. DOI: `10.1039/d3nr00645j`.

[89] A. Dahal and M. Batzill, "Graphene-nickel interfaces: A review", *Nanoscale*, vol. 6, no. 5, pp. 2548–2562, Jan. 2014. DOI: `10.1039/c3nr05279f`.

[90] J. Chazalviel, *Coulomb screening by mobile charges: applications to materials science, chemistry, and biology.* Birkhäuser, 1999, p. 355. DOI: `10.1007/978-1-4612-1762-6`.

[91] J. Y. Wu, W. P. Su, and G. Gumbs, "Anomalous magneto-transport properties of bilayer phosphorene", *Scientific Reports*, vol. 10, no. 1, 2020. DOI: `10.1038/s41598-020-64106-0`.

[92] R. Gupta, S. Kakkar, B. Dongre, J. Carrete, and C. Bera, "Enhancement in the Thermoelectric Performance of SnS Monolayer by Strain Engineering", *ACS Applied Energy Materials*, vol. 6, no. 7, pp. 3944–3952, 2023. DOI: `10.1021/acsaem.3c00110`.

[93] T. Eknapakul, P. D. King, M. Asakawa, P. Buaphet, R. H. He, S. K. Mo, H. Takagi, K. M. Shen, F. Baumberger, T. Sasagawa, S. Jungthawan, and W. Meevasana, "Electronic structure of a quasi-freestanding MoS2 monolayer", *Nano Letters*, vol. 14, no. 3, pp. 1312–1316, Mar. 2014. DOI: `10.1021/nl4042824`.

[94] N. H. Lam, P. Nguyen, S. Cho, and J. Kim, "Bandgap reduction at wrinkles on the cleavage surfaces of GeSe single crystals", *Surface Science*, vol. 730, p. 122 251, Apr. 2023. DOI: `10.1016/j.susc.2023.122251`.

[95] X. Zhang, J. Shen, S. Lin, J. Li, Z. Chen, W. Li, and Y. Pei, "Thermoelectric properties of GeSe", *Journal of Materiomics*, vol. 2, no. 4, pp. 331–337, 2016. DOI: `10.1016/j.jmat.2016.09.001`.

[96] G. Liu, L. Wu, X. Chen, T. Li, Y. Wang, T. Guo, Z. Ma, M. Zhu, S. Song, and Z. Song, "The investigations of characteristics of GeSe thin films and selector devices for phase change memory", *Journal of Alloys and Compounds*, vol. 792, pp. 510–518, Jul. 2019. DOI: `10.1016/j.jallcom.2019.04.041`.

[97] T. G. Edwards and S. Sen, "Structure and Relaxation in Germanium Selenide Glasses and Supercooled Liquids: A Raman Spectroscopic Study", *J. Phys. Chem. B*, vol. 115, pp. 4307–4314, 2011. DOI: `10.1021/jp202174x`.

[98] K. Momma and F. Izumi, "VESTA 3 for three-dimensional visualization of crystal, volumetric and morphology data", *Journal of Applied Crystallography*, vol. 44, no. 6, pp. 1272–1276, Oct. 2011. DOI: `10.1107/S0021889811038970`.

[99] T. Hu and J. Dong, "Two new phases of monolayer group-IV monochalcogenides and their piezoelectric properties", *Physical Chemistry Chemical Physics*, vol. 18, no. 47, pp. 32 514–32 520, Nov. 2016. DOI: `10.1039/c6cp06734d`.

[100] C. Liu, S. Guan, H. Yin, W. Wan, Y. Wang, and Y. Zhang, "γ-GeSe: A two-dimensional ferroelectric material with doping-induced ferromagnetism", *Applied Physics Letters*, vol. 115, no. 25, p. 252 904, Dec. 2019. DOI: `10.1063/1.5133022`.

[101] N. Luo, W. Duan, B. I. Yakobson, and X. Zou, "Excitons and Electron–Hole Liquid State in 2D γ-Phase Group-IV Monochalcogenides", *Advanced Functional Materials*, vol. 30, no. 19, May 2020. DOI: `10.1002/adfm.202000533`.

[102] N. Higashitarumizu, H. Kawamoto, C. J. Lee, B. H. Lin, F. H. Chu, I. Yonemori, T. Nishimura, K. Wakabayashi, W. H. Chang, and K. Nagashio, "Purely in-plane ferroelectricity in monolayer SnS at room temperature", *Nature Communications 2020 11:1*, vol. 11, no. 1, pp. 1–9, May 2020. DOI: 10.1038/s41467-020-16291-9.

[103] F. Guo, H. Guo, K. Zhang, N. Yuan, and J. Ding, "Variations in structural and optoelectronic features of thermally co-evaporated SnS films with different Sn contents", *Thin Solid Films*, vol. 642, pp. 285–289, Nov. 2017. DOI: 10.1016/j.tsf.2017.09.031.

[104] R. E. Banai, M. W. Horn, and J. R. Brownson, *A review of tin (II) monosulfide and its potential as a photovoltaic absorber*, Jun. 2016. DOI: 10.1016/j.solmat.2015.12.001.

[105] H. G. Min, C. Lyi, and Y. Kim, "Tunable bulk photovoltaic effect in strained γ -GeSe", *Physical Review B*, vol. 106, no. 20, p. 205 153, 2022. DOI: 10.1103/PhysRevB.106.205153.

[106] M. Yu, H. Ascolani, G. Zampieri, D. P. Woodruff, C. J. Satterley, R. G. Jones, and V. R. Dhanak, "The structure of atomic sulfur phases on Au(111)", *Journal of Physical Chemistry C*, vol. 111, no. 29, pp. 10 904–10 914, 2007. DOI: 10.1021/jp072088+.

[107] P. Shao, Q. L. He, H. Zhang, C. Y. Wang, and Y. R. Zhao, "Adsorption of sulfur on Au(111) surface: An extremely stable configuration", *Journal of Molecular Graphics and Modelling*, vol. 122, p. 108 494, Jul. 2023. DOI: 10.1016/j.jmgm.2023.108494.

[108] A. Tołłoczko, S. J. Zelewski, M. Błaszczak, T. Woźniak, A. Siudzińska, A. Bachmatiuk, P. Scharoch, and R. Kudrawiec, "Optical properties of orthorhombic germanium selenide: an anisotropic layered semiconductor promising for optoelectronic applications", *Journal of Materials Chemistry C*, vol. 9, no. 41, pp. 14 838–14 847, 2021. DOI: 10.1039/d1tc04280g.

Acknowledgments

This thesis summarises my work of the last years and brings an end to my Ph.D. research. Self-explanatory, this would not be possible without the help and assistance from many. Here, I would like to express my gratitude to multiple people:

- Prof. Dr. **Carsten Busse** for giving me the opportunity to start this research journey at his group as well as guidance and encouragement. I am grateful for all discussions and inspiring ideas leading to new perspectives.

- Prof. Dr. **Arkady Krasheninnikov** for co-refereeing this thesis.

- **Alice Bremerich**, **Dr. Thais Chagas** and **Dina Wilks** for proofreading of this thesis. Their insights and suggestions were very helpful.

- All the master students, I was able to supervise: **Sammer Iqbal**, **Muhammad Ali Martuza**, **Ankur Das**, **Veronika Blecker** and especially to **Dina Wilks**, who will continue this wonderful project.

- All members of the group Busse throughout my time in Siegen. I need to emphasise a special thanks to some particular colleagues. **Alice Bremerich** and **Dina Wilks** for not only supporting in any imaginable lab task but also having an enjoying office culture as friends. Dr. **Thais Chagas** for always being attentive and ready to help. **Kai Mehlich** for his witty comments in day to day situations and Dr. **Jiaqi Cai** for introducing me to the systems and encouraging me to look out for small details to overcome problems.

- Dr. **Mahdi Ghorbani** and Dr. **Arkady Krasheninnikov** for the theoretical input to the surprising edge situation of SnSe. The DFT and first-principles calculations helped creating the model of the edge relaxation of SnSe on gr/Ir(111).

- The team of the mechanical workshop, especially **Uwe Krüger** and **Olaf Meyer** for trying to find a solution despite all challenging requests or situations.

- The team of the electronics workshop around **Michael Ziolkowski** for quickly repairing any electronics.

- **Sven Neuberger** and Prof. Dr. **Schmedt auf der Günne** for allowing and implementing experiments with single crystals in a furnace oven, such that insight to crystallisation preference of GeSe on Au(111) could be reached.

- **Markus Hartmann** for XRD on GeSe powder to confirm the degradation during evaporation.

- Last but not least, all my family and friends for the support and encouragement I received from them over these years and beyond.

Thank you!

Eigenständigkeitserklärung

Hiermit erkläre ich, Paulus Aleksa, dass ich die vorliegende Dissertation mit dem Titel "Preparation and characterisation of two-dimensional ferroelectrics" selbstständig, ohne fremde Hilfe und in eigenen Worten niedergeschrieben habe. Ich versichere insbesondere, dass ich alle wörtlichen und sinngemäßen Übernahmen aus Quellen und anderen Ergebnissen als solche gekennzeichnet sowie vollständig aufgeführt habe.

_____   _____
Ort, Datum   Unterschrift